EFFICIENT CATALYSTS FOR WATER OXIDATION: SYNTHESIS, CHARACTERIZATION AND COMPUTATIONAL STUDY

Khalid Azmani Oualite

UNIVERSITAT ROVIRA i VIRGILI

EFFICIENT CATALYSTS FOR WATER OXIDATION: SYNTHESIS, CHARACTERIZATION AND COMPUTATIONAL STUDY

KHALID AZMANI OUALITE

DOCTORAL THESIS
2022

DOCTORAL THESIS

Efficient catalysts for water oxidation: Synthesis, Characterization and Computational study

Khalid Azmani Oualite

Supervised by

Prof. Dr. Josep Maria Poblet Rius

Universidad Rovira i Virgili (URV)

Prof. Dr. José Ramón Galán Mascarós

Institut Català d'Investigació Química (ICIQ)

Tarragona, 2022

UNIVERSITAT
ROVIRA i VIRGILI

Prof. Dr. Josep Maria Poblet i Rius, Tenure Professor of the Physical Chemistry and Inorganic Department of the Universitat Rovira i Virgili (URV), and Prof. Dr. José Ramón Galàn Mascarós, Group Leader of the Institute of Chemical Research of Catalonia (ICIQ) and Research Professor of the Catalan Institution for Research and Advances Studies (ICREA),

CERTIFIES that the present study entitled "**Efficient catalysts for water oxidation: Synthesis, Characterization and Computational study**", presented by Khalid Azmani Oualite to receive the PhD degree in Chemistry, has been carried out under our supervision, in the in the Universitat Rovira I Virgili (URV) and Institute of Chemical Research of Catalonia (ICIQ).

Tarragona, 21st November 2022

PhD Thesis supervisors

Prof. Dr. Josep Maria Poblet i Rius

Prof. Dr. José Ramón Galàn Mascarós

The work performed in the present Doctoral Thesis has been possible thanks to the funding of:

- Universitat Rovira i Virgili (URV)
- Institut Català d'Investigació Química (ICIQ)
- *Institut de Chimie Physique (ICP)*
- ICREA foundation
- Ministerio de Ciencia, Innovación y Universidades – Agencia Estatal de Investigación
- Generalitat de Catalunya
- Ministerio de Economía y Competitividad – FPU fellowship (FPU16/02588)

A mi Familia y en especial a mis Padres

"Abandona (toda esperanza en) este mundo y Dios te amará. Y abandona (toda esperanza en) lo que esté en posesión de la gente y la gente te amará"

- *Profeta Mahoma*

Referencia: Ibn Mayah, Al Hakim. Al-Albani también lo declaró auténtico en As-Silsilah

Acknowledgements

Quiero agradecer a mis supervisores Dr. José Ramón Galán-Mascarós (JR) y Prof. Josep María Poblet por ofrecerme la oportunidad de participar en este proyecto, sobre todo por tratarme como un compañero y no simplemente como un estudiante. Gracias por la libertar proporcionada para el desarrollar de los proyectos recogidos en esta tesis, por tenerme en cuenta en otros proyectos de colaboración y otórgame responsabilidad que me han hecho crecer como investigador y persona. Gracias por la paciencia que habéis tenido conmigo y por cada uno de los consejos que me han llevado a culminar este proceso.

La tesis para mi es la culminación de un proceso que empezó realmente hace diez años, cuando Poblet me impartía la clase de *Complements de Química* del grado de Química en la Universidad y me dio la posibilidad de incorporarme en su grupo de investigación tan pronto. Debo confesar que no encuentro las palabras para agradecerle su implicación, su cuidado, orientación a lo largo de estos diez años. Todo este tiempo hace que no pueda verle únicamente como supervisor.

I would also like to thank Prof. Israël-Martyr Mbomekall and his team from *Equipe d'Electrochimie et de Photo-electrochimie, Institut de Chimie Physique* for his support and complete dedication on the synthesis and characterization of the subject of study polyoxometalate compounds.

También quiero agradecer especialmente a la Dr. María Besora ya que ha sido como un supervisor para mí, acompañándome en todo momento en el enredado proceso de entender los mecanismos de oxidación de agua como también por ser fuente de inspiración.

En segundo lugar, muchas gracias a todos los compañeros y compañeras de la URV como de ICIQ, En especial, Nuria por enseñarme a gatear dentro del mundo de la computación, Marc Alias por ser más que un compañero (ha sido un placer crecer juntos desde el grado de química), Felipe por ser un socio y amigo antes que un compañero,

Ximo, Roser, Almudena, Antonio, Laura, Albert, Toni, Mariano, Gerard, Marta, David, Andrea, Mabel, Vanesa, Stefano, Ilario, Neus, Scott, Jiahao, Álvaro,Juanjo *to be always there always*

En tercer lugar, al personal de suporte de la URV e ICIQ, en especial a Josep por ayudarme a poner en marcha nuestro incipiente laboratorio de electroquímica en la URV. Xavi y León por hacer lo imposible y en tiempo récord lo que necesitaba.

A Salua por embellecer todo este proceso y hacer único cada día que pasamos juntos, ya son diez años desde que nos unió el principio de *Le Châtelier* en la prueba de acceso a la universidad. Gracias por confiar en mí, gracias por decir ¡sí quiero!, gracias por hacer que la Tesis sea breve a pesar de durar cinco años. No hay recuerdo más bonito de la Tesis que recordar que me he unido contigo para siempre.

A mis apreciados hermanos y hermanas, Mustafa, Mohamed, Zineb, Houssin, Hassan e Iman que me complementan, gracias por creer en mí. Por último y más importante a mis queridos padres por hacerme ser lo que soy, por apoyarme en cada paso que doy, por animarme a seguir estudiando, convirtiéndome en una referencia para toda la familia.

Table of Contents

Summary

Storage energy into chemical bonds has become nowadays the primary key to make possible the transition from carbon dependency to renewable (i.e., solar or wind) energy solving the intermittency of this. For example, water splitting involves storing of the energy in to H_2 and O_2. However, the oxidation reaction of water to O_2 is a bottleneck in this process. In this Thesis, we have joined the international challenge of deeply understanding of water oxidation and search for an efficient, robust, and inexpensive heterogeneous water oxidation catalyst.

We have focused on the use of already described polyoxometalates (POMs) as water oxidation catalysts in aqueous media at different pH. We have synthesized, characterized, and evaluate their catalytical activity. At all times we have confirmed the stability and integrity of the catalysts by performing a pre and post catalytic characterization.

First, we have deeply studied the promising Co-containing polyoxometalate in acidic media by studying different parameters involving structure, composition and nuclearity through a series of Cobalt - POM (Co-POM) incorporated into carbon paste electrodes as insoluble salts of Cs^+ and/or Ba^{2+}. Then we have moved to evaluate polyoxometalate based on the most abundant and cheapest transition metal (Iron). We have focused on the tetrairon Weakley sandwich $[(Fe^{III}OH_2)_2\text{-}Fe^{III}_2\ (PW_9O_{34})_2]^{6-}$ ($Fe_4P_2W_{18}$) due to be isostructural of tetracobalt Weakley sandwich one of the most extensively studied Co-POMs. We have started evaluating in the neutral media the catalytic activity and confirming the complete faradaic efficiency and the true catalyst. Then we have investigated the reaction mechanism employing computational methods to understand the different catalytic performance with Co-POM. Finally, we want to test the robust character of POM in acidic media in the carbon paste environment, we have evaluated $Fe_4P_2W_{18}$ as water oxidation catalyst in acidic media to determine the pH effect. Effectively, we could confirm the stability of the Fe-POM. Surprisingly, our results show a low faradaic efficiency which we could relate to a competitive reaction to water oxidation based on carbon oxidation.

List of Publications

The results of this PhD Thesis have delivered the following publications:

Khalid Azmani, Maria Besora, Joaquín Soriano-López, Meriem Landolsi, Anne-Lucie Teillout, Pedro de Oliveira, Israël-Martyr Mbomekallé, Josep M Poblet, José-Ramón Galán-Mascarós. Understanding polyoxometalates as water oxidation catalysts through iron vs. cobalt reactivity. Chem. Sci., 2021, 12, 8755 – 8766 DOI: 10.1039/D1SC01016F

JT Arens, M Blasco-Ahicart, K Azmani, J Soriano-López, A García-Eguizábal, JM Poblet, JR Galán-Mascaros. Water oxidation electrocatalysis in acidic media with Co-containing polyoxometalates. Journal of catalysis, 2020, 389 345 – 351, DOI: 10.1016/j.jcat.2020.06.006

Abbreviations

η	Overpotential
μ	Micro
CAN	Cerium (IV) ammonium nitrate
CP	Carbon paste
CV	Cyclic voltammetry
DFT	Density functional theory
e^-	Electron
E^0	Thermodynamic potential
E_{app}	Applied potential
EDX	Electron dispersive X-ray spectroscopy
ES	Earth system
eV	Electronvolt
GC	Gas chromatography or Glassy carbon electrode
H^+	Proton
HER	Hydrogen evolving reaction
ICP-OES	Inductively coupled plasma optical emission spectroscopy
IR	Infrared spectroscopy
j	Current density
LSV	Linear sweep voltammetry
M	Molar or Metal

mA/cm^2	Milliampere per square centimetre
NHE	Normal hydrogen electrode
OER	Oxygen evolving reaction
PAMAM	Polyamidoamine
PB	Planetary boundaries
PCET	Proton-coupled electron transfer
PEM	Proton Exchange Membrane or Polymer Electrolyte Membrane
Pi	Phosphate
POM	Polyoxometalate
PSI	Photosystem I
PSII	Photosystem II
RDE	Rotating disk electrode
rpm	Revolutions per minute
TGA	Thermogravimetric analysis
TOF	Turnover frequency
TON	Turnover number
WOC	Water oxidation catalyst
XPS	X-ray photoelectron spectroscopy

Chapter 1

General Introduction

1.1. The fingerprint of an unsustainable energy consumption

In the 90's, an international awareness begins to reflect on the energy impact which it has on the environment. The continuous growth of human population is expected to increase 2 billion persons in the next 30 years reaching 9.7 billion in 2050. Furthermore, the world lives a massive economic progress with a high demanding living standards which involve a remarkable growth of world energy consumption. This is translated in a consumption increase of 47% in the next 30 years according to the US Energy Information Administration. This energy consumption trend will keep us tied significant to carbon sources in absent of any policy changes or technological breakthroughs.

Nowadays, the world's energy needs are based mainly on carbon sources. More specifically, the natural gas and petroleum represent about 60% of energy consumption. Even though there are reserves of fossil fuels to maintain the energy rate for the coming centuries, this high rate of fossil sources involves a significant carbon emission in CO_2 form. Scientific evidence indicate that the atmospheric CO_2 concentration has been kept constant between 210-300 ppm for the last 650000 years. However as shown in Figure 1.1, since industrial revolution stars a progressive trend of CO_2 emission, which involves a high rate and constant accumulation of CO_2 in the atmosphere with the absence of natural destruction mechanisms of CO_2. Along the last 50 years the concentration reaches a maximum value of 380 ppm.

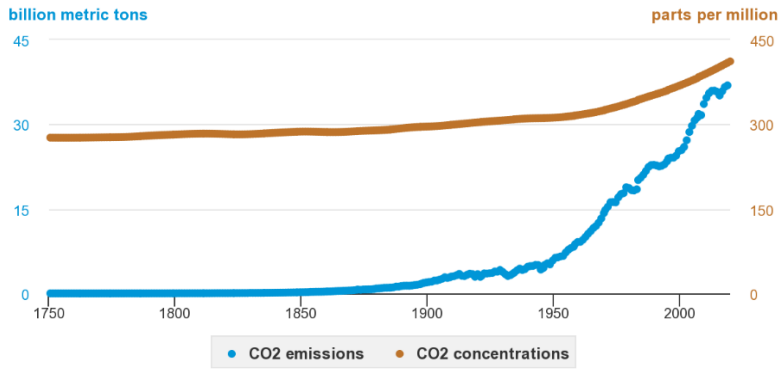

Figure 1.1. World carbon dioxide (CO2) emissions from fossil fuel combustion and global atmospheric concentrations CO2 (1751-200).[1]

The accumulative CO_2 in the atmosphere from fossil, together with others anthropogenic GHG emissions (Figure 1.2), becomes a significant global issue throw off balance the greenhouse phenomena. This disequilibrium has dangerous negative effect not only in human health but also in the stable environmental state of the current geological epoch known as Holocene. The result could lead to abrupt environmental change making the Earth uninhabitable for the human species.

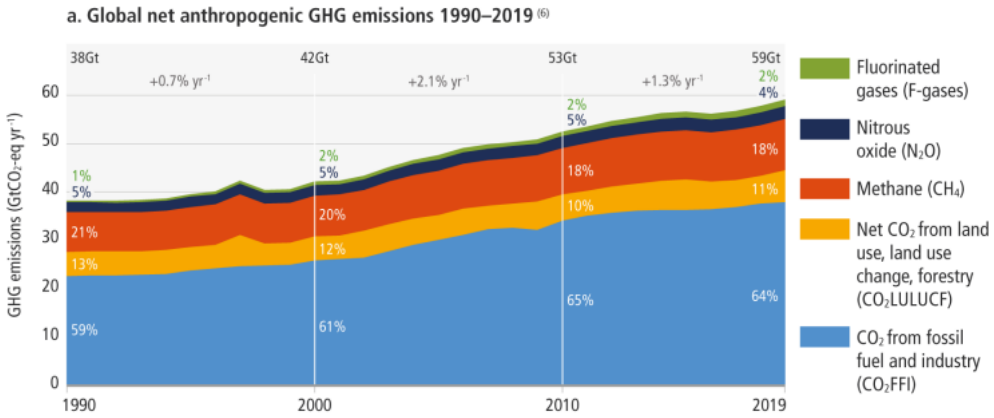

Figure 1.2. Aggregate annual global net anthropogenic GHG emissions by groups of gases from 1990 to 2019 reported in $GtCO_2$-eq yr^{-1}: CO_2 from fossil fuel combustion and industrial processes (CO_2-FFI); net CO_2 emissions from land use, land use change and forestry (CO_2-LULUCF); methane (CH_4); nitrous oxide (N_2O); and fluorinated gases (F-gases) comprising hydrofluorocarbons (HFCs), perfluorocarbons (PFCs), Sulphur hexafluoride (SF_6) as well as nitrogen trifluoride (NF_3). The fraction of global emissions for each gas is shown 1990, 2000, 2010 and 2019, as well as the aggregate average annual growth rate between these decades.[2]

As shown in figure 1.3, the uncontrolled race for economic growth between the different countries do not help to maintenance the Earth System (ES) in a resilient and accommodating state. the major producers of greenhouse gas emissions are China and followed by United States. Considering the evolution of CO_2 emissions, the China and United State race culminates 10.668 and 4.713 million $MtCO_2$ in 2020, which represent 30% and 13% of global emissions.[3]

The impact of the global environmental change is not something will happen in the future. Global climate data shows global temperatures increase of 1°C from 1901-2020, sea level rise has accelerated from 1.7 mm/year to 3.2 mm/year since 1993, average thickness of glaciers has decreased more than 25 meters since 1970 in consequence the area covered by sea ice in the arctic at the end of summer has shrunk by about 40% (Figure 1.4).

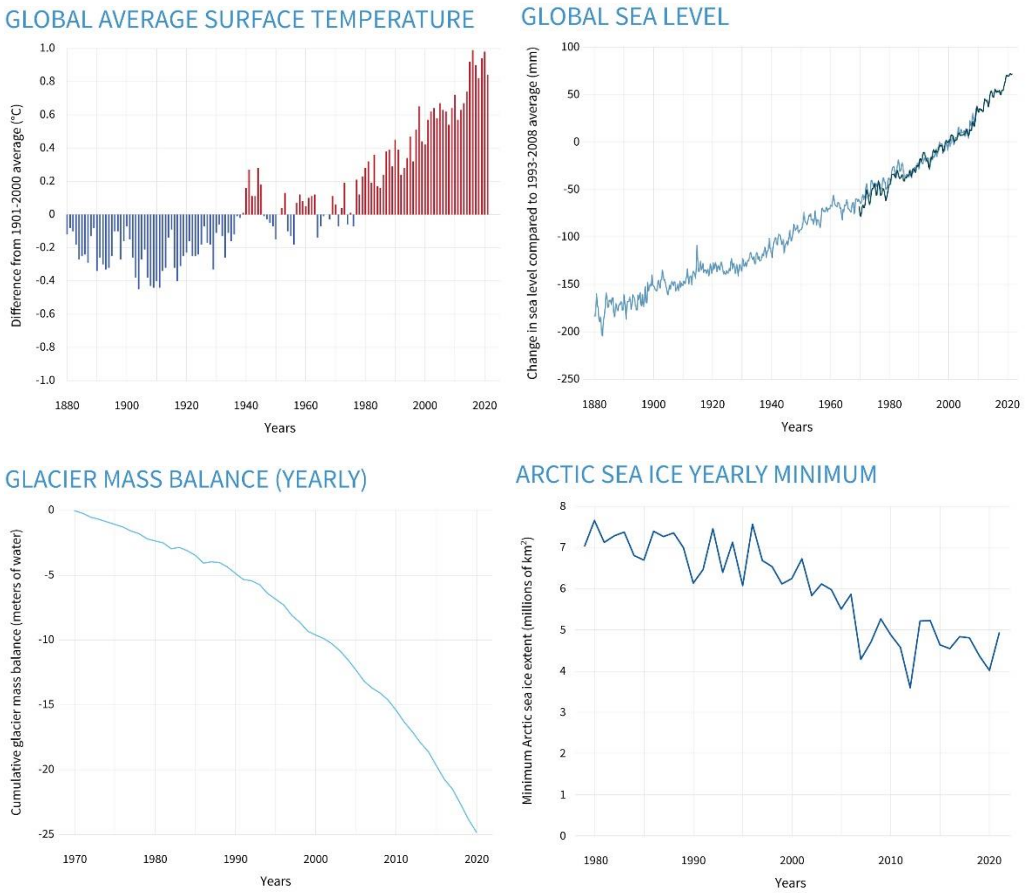

Figure 1.4. a) Yearly surface temperature compared to the 20th-century average from 1880–2021. Blue bars indicate cooler-than-average years; red bars show warmer-than-average years[4] b) Seasonal (3-month) sea level estimation. The values are shown as change in sea level in millimeters compared to the 1993-2008 average[5] c) Ice loss relative to 1970 for the glaciers in the World Glacier Monitoring Service's climate reference network[6] d) Sea ice extent in the Arctic at the end of the summer melt season each September from 1979–2021[7]

To avoid irreversible climate change, Rockstrom et al. have proposed a planetary boundary (PB) which defines a safe and respectful human operating mode with the Earth system. Nine processes have identified to be bounded: climate change; rate of biodiversity loss (terrestrial and marine); interference with the nitrogen and phosphorus cycles; stratospheric ozone depletion; ocean acidification; global freshwater use; change in land use; chemical pollution; and atmospheric aerosol loading. [8,9] Two PB have been transgressed, such as genetic diversity and biogeochemical flows. Moreover, climate change and land-system change are in the zone of increasing risk. Recently, the scientific discussion went around to identify and quantify novel entities (NE-PB). According to Steffen et al.[8], novel entities consist in created, introduced, or recirculated chemicals, engineered materials, and their transformation products, that have the potential to cause effects on vital Earth system processes.[10]

These results must constrain humanity to change the way of thinking and working to guaranty Holocene equilibria. Taking to account that humanity should have a responsible consume of the energy by defining a more Earth friendly habits, humanity must switch to carbon free dependence. There are three alternatives to compensate the high energy demanding: nuclear fission, carbon capture/storage and the use of renewable energy.[11] Nevertheless, renewable energies are the most plausible alternative due to its clean, abundant, and economically affordable character. [12] Taking in to account the economical point of view, renewables have become the lowest-cost source of new power generation. As costs continue to fall for solar and wind technologies, this will be true in a growing number of countries (Figure 1.5) .[2,13] Here some examples like hydroelectric, geothermal, wind, tides, ocean thermal energy conversion, and solar. The latter is available at any location on Earth's surface making it suitable to replace completely the carbon dependency.

The solar energy use is determined by capture and conversion of sun light in electrical energy using photovoltaic systems. On the other hand, the generated energy should be stored since the sun is intermittent. Regarding the last two decades, photovoltaic systems are deeply developed reducing the cost per watt of delivered solar energy. However,

solar energy storage is the major challenge to use solar energy as the main energy source. There are different storage technologies like batteries, mechanical storage, concentrated solar thermal. However, the most plausible method is based on artificial photosynthesis, where solar energy can be stored in chemical bonds producing clean and useful fuels. Clear example is the promising water splitting where the solar energy is stored in H_2 and O_2. As we mention previously, with the continuously decreasing costs of solar photovoltaic and wind electricity, the production of green hydrogen is increasing. This attractive strategy becomes the key for renewable energy source as the drivers to reverse the negative course of power energy sector. However, this storage process involves efficient and optimal electroyzers to minimize the cost. Fortunately, the deep interest in this technology allows to reduce the capital cost of electrolysis by 60% since 2010, resulting in a decrease of hydrogen cost from a range of 10-15 $/kg to as low as 4-6 $/kg in that period.

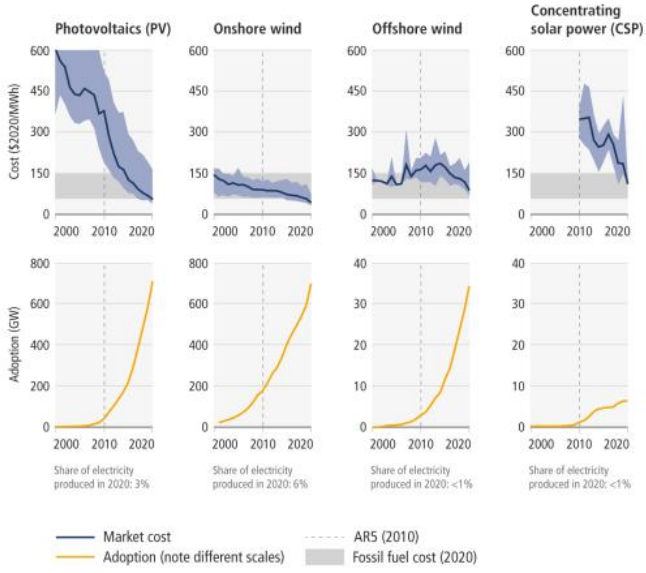

Figure 1.5. Top) Global costs per unit of energy (USD/MWh) for Photovoltaics, Onshore and Offshore wind and Concentration Solar Power. Bottom) Cumulative global adoption for each technology.[2]

1.2. Mimicking the nature: water splitting

The solar energy can be the promising key for the complex dilemma of accelerated energy consumption rate and the maintenance of the Earth system (ES) in a resilient and accommodating state. In general terms, the irradiation received by Earth along one-hour equivale to the total energy consumed by humans in a year.[14]

Looking on the nature machinery responsible of the Earth's life evolution over billions of years, the photosynthesis becomes the process that takes advantage of sunlight and convert it into chemical energy.[15] Photosynthesis is a biochemical process that nurture the biosphere as the basis for the food chain. This may be split into the 'light' and 'dark' reactions. In the light reactions, water is split using light into oxygen, protons, and electrons. Followed by the dark reactions where the protons and electrons are used to reduce CO_2 to carbohydrate.[16] The two processes reactions can be summarized:

Light reactions:

$$2H_2O + \text{light} \rightarrow O_2 + 4H^+ + 4e^- \qquad G^o = +317\ kJ{\cdot}mol^{-1}$$

Dark reactions:

$$CO_2 + 4H+ + 4e^- \rightarrow CH_2O + H_2O \qquad G^o = +162\ kJ{\cdot}mol^{-1}$$

Overall:

$$H_2O + \text{light} + CO_2 \rightarrow CH_2O + O_2 \qquad G^o = +479\ kJ{\cdot}mol^{-1}$$

Photosynthesis converts ~200 billion tons of CO_2 into complex organic compounds annually and produces ~140 billion tons of oxygen into the atmosphere. The oxygen produced as a by-product of photosynthesis allowed the formation of the ozone layer, the evolution of aerobic respiration and thus complex multicellular life.[17] By facilitating conversion of solar energy into chemical energy, photosynthesis acts as the primary energy input into the global food chain. Nearly all living organisms use the complex organic compounds derived from photosynthesis as a source of energy. The breakdown of these organic compounds occurs via the process of aerobic respiration, which of course also requires the oxygen produced by photosynthesis.

$$CH_2O + O_2 \rightarrow CO_2 + H_2O \qquad G^o = -479\ kJ{\cdot}mol^{-1}$$

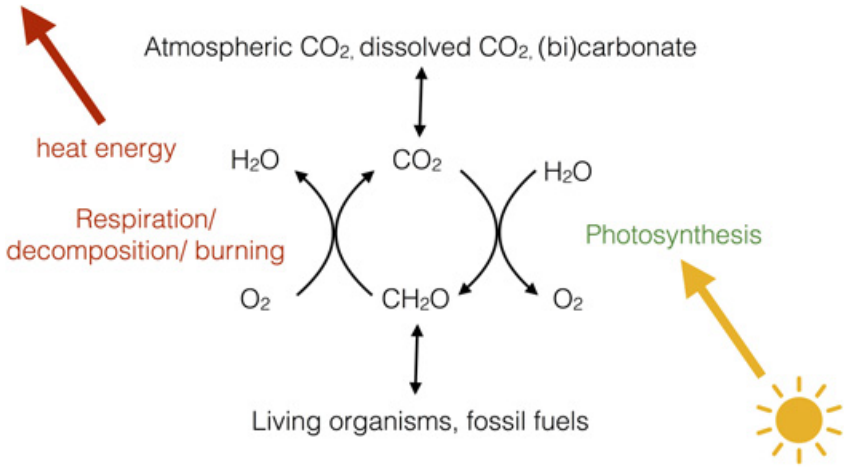

Figure 1.6. Natural photosynthesis and aerobic respiration: light and dark reactions.

Photosynthesis takes place mainly in the chloroplast, which are organelles that are bound by a double membrane and are found in the cells of green plants and algae. They contain a third membrane system that is known as thylakoids, where all the pigments, electron transport complexes and the ATP synthase (F-ATPase) are located.[18,19]

The biochemical process begins with the splitting of water by Photosystem II (PSII), where the light is used to oxidize water to oxygen and reduce the electron acceptor plastoquinone to plastoquinol. With the help of thylakoid-embedded protein complex called cytochrome b6f, plastoquinol is oxidized to plastoquinone and reduces an electron carrier protein plastocyanin. In both steps, protons are released and lead to formation of a proton gradient across the thylakoid membrane that is used by the ATP synthase enzyme to make ATP. The electrons derived from water experience a second light-step takes place by another chlorophyll protein complex called Photosystem I (PSI). In this moment, PSI give rise the formation of NADPH by oxidizing plastocyanin and reducing electron carrier protein ferredoxin which is used by ferredoxin–NADP+ reductase (FNR) enzyme.[17,18]

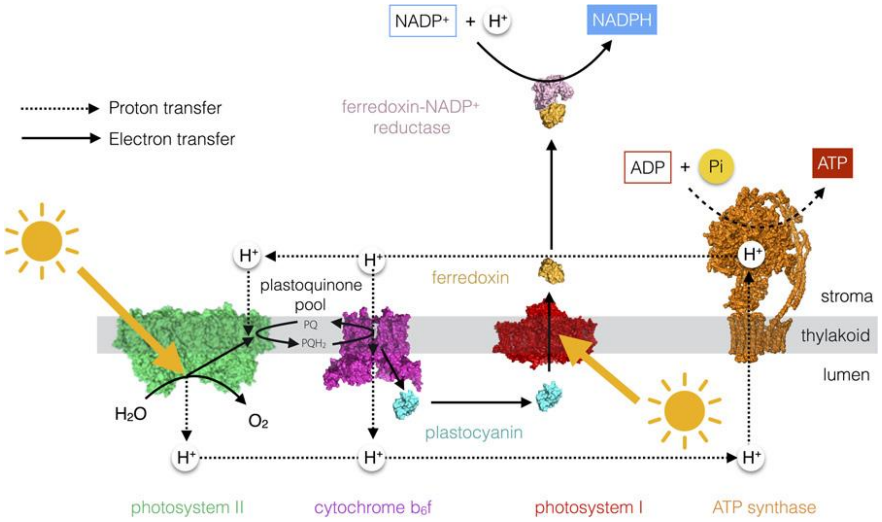

Figure 1.7. The photosynthetic electron and proton transfer chain.[17]

To culminate the conversion of sunlight into chemical energy, the energy-rich compounds previously generated (ATP and NADPH) are used to reduce CO_2 into carbohydrates through the Calvin-Benson cycle. The reaction is catalyzed by enzyme ribulose-1,5-bisphosphate carboxylase/oxygenase and is known as Rubisco.[18]

In 1912, Giacomo Ciamician has postulated a revolutionary hypothesis to substitute the fossil fuels by sunlight using artificial photochemical reactions.[20,21] An approach for mimicking the nature photosynthesis outside of cellular environment consist in capture sunlight by Photovoltaic cell generating electron/hole pairs and invest the charges to split water in H_2 and O_2.

$$2H_2O \rightarrow 2H_2 + O_2$$

The water splitting consists in a redox process which involves two semi reactions where the solar energy is stored into chemical bonds of H_2 and O_2. In one hand, Oxygen Evolution Reaction (OER) where the water is oxidized at the anode producing oxygen. In the other hand, Hydrogen Evolution Reaction (HER) where protons are reduced at the cathode generating hydrogen.

$$2H_2O \rightleftharpoons O_2 + 4H^+ + 4e^-$$

$$4H+ + 4e, \rightleftharpoons 2H_2$$

The water oxidation reaction is considered bottleneck step of overall process, as water is an extremely poor electron donor since the redox potential of the water-oxygen couple is 800 mV under mild temperature and pH conditions.

In the nature photosynthesis, PSII plays the role to mediate the water splitting, starting with the light energy conversion to electricity energy (charge separation) through chlorophylls known as P680 (Absorption peak in the red part at 680 nm). The excitation of P680 gives rise the formation of an extremely oxidizing specie with a redox potential of 1.2V (vs NHE). Considering that charge separation involves only one electron, the formation of one oxygen molecule from two molecules which involves 4 electrons require turnovers of PSII.

In second step, the regeneration of P680 is performed by an oxygen-evolving complex (OEC) located in PSII. This was well described and crystallographic solved by Kamiya et al in 2011.[22] The OEC consist of cube-like cluster with three manganese and one calcium ions bridged with mono-μ-oxo. One of these oxygens connects the cluster to a fourth external manganese ion, which is designated Mn4. The latter binds two water molecules as a substrate and extracts electrons from it. [23]

Coming back to artificial photosynthesis concept, the water oxidation should crucially be assisted by a catalyst to minimize the applied potential to Nernstian potential to overcome the activation barriers despite other experimentally issue as concentration effect and voltage drops due to the resistance on the medium. In practice, water electrolyzers are electrochemical devices used to split water molecules into hydrogen and oxygen by passage of an electrical current which can come from photovoltaic system or an alternative renewable source, i.e., wind. The basic principle of a water electrolysis cell consists of two electrodes separated by an electrolyte. The electrolyte is the media responsible for transporting the generated chemical charges (anions (-) or cations (+)) from one electrode to the other. Electrolyzers are typically divided into four main technologies, these are distinguished based on the electrolyte and temperature of

operation: alkaline and polymer electrolyte membrane (PEM) are already commercial, whereas anion exchange membrane (AEM) and solid oxide are nowadays at lab scale.[24]

Nowadays, the scientific challenge is focused on reduce the high cost across the entire value chain, from electrolysis to transport and fuel cells. One of the most challenging aspects is to optimize the water oxidation catalyst (WOC) looking for robust, efficient, inexpensive efficiency and stability.

1.3. Water Oxidation Catalysts

The use of water oxidation catalysts (WOC) is non-negotiable in to attenuate the high energy demand of the water oxidation. In 1982, Meyler et al. reported the first catalyst for water oxidation known as "Blue Dimer" due to its characteristic color.[25] The deep search for water oxidation catalyst during the last years shed some light onto mechanism of water splitting and allows to discover and understand the precise electronic properties requirement for an efficient WOC.

Homogenous WOC

The beginning of water oxidation research was focused on homogeneous catalyst as the molecular catalysts allow easier interpretation of the complex and interlocking parameters of the process. The list of catalyst goes mainly from ruthenium, iridium, and manganese. However, other base metal catalysts, most based on cobalt, and iron are also of current interest.

Ruthenium-based WOCs

The exploration of ruthenium empowers to understand and settle the key aspects of WOC search. As introduced before, the first well-defined example of a homogenous water oxidation catalyst is known as "Blue Dimer". This is based on μ-oxo-bridged ruthenium dimer coordinated by polypyridyl ligands with formula cis,cis-$(bpy)_2(H_2O)Ru(III)(O)Ru(III)(H_2O)(bpy)_2]^{4+}$ (Figure 1.8). The characteristic cis,cis arrangement at each metallic centers with respect to the -bpy- ligand allows the aqua ligands to align in parallel with free-rotation along the μ-oxo bridge. Furthermore, the steric constraints conferred by the bpy- ligand gives a linear geometry to the Ru centers through the μ-oxo bridge.

The ruthenium dimer activity has been studied thorough numerous experiments and computational methods. The results show a sophisticated mechanism of water oxidation involving for example a multi and successive Proton Coupled Electron Transfer (PCET) reactions which are the key for accumulative oxidative equivalents at one site without

upturn to charged species. To this we must add the higher oxidation states of the Ru-O-Ru core, cross-electron transfer between non-adjacent oxidation states, different intermediate acid-base equilibrium reactions and some anion exchanges between the surrounding solution and the coordinated water molecules.[26,27]

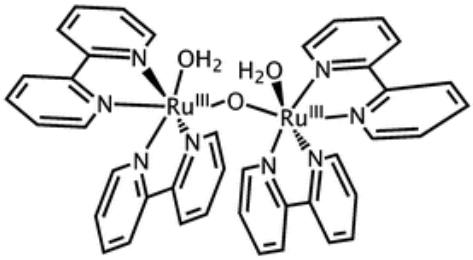

Figure 1.8. Drawn structure of the ruthenium "Blue Dimer".

Although the complex and discrepancy interpretations on the mechanism, the catalytically active specie is formed by the four-electron oxidation of Ru(III)–O–R(III) to form Ru(V)–O–R(V) specie. There are proposed two mechanisms concerning the O_2-releasing step. In one hand, water molecule attacks the active center leading to hydro-peroxo specie which promote an intramolecular oxidation through the non-involved metallic center with the O_2 releasing.[28–30] The alternative mechanism proposes the oxidation of ligand because of an attack of a molecule of water at the position of the pyridine ring. Then the radical specie is neutralized by an attack of a second water at the β-position leading to O−O bond formation after oxidation by the Ru-centers. Finally, the ligand recovers aromaticity by releasing oxygen.[31–33]

Regarding the efficiency, the "Blue Dimer" has achieved turnover numbers (TON) of 11 with turnover frequencies (TOF) between $10^{-1} – 10^{-3}$ s^{-1}. To reach an efficient and robust catalyst, stars a race to improve the stability and activity by stabilizing the ligand framework. At the same time, computational studied become crucial to understand and investigate the intermediates involved in the plausible mechanism for water oxidation.

Iridium-based WOCs

In 2008, the iridium complexes arise as a candidate for water oxidation reaction. Bernhard *et al.* described a series of catalyst based on cyclometalated Ir-complexes containing 2-phenylpyridine-type (ppy) ligands with two free sites in cis configuration for water to be coordinated (Figure 1.9).[34] The oxidative activity using Ce^{IV} lead to maximum TOF of $1.5 \cdot 10^{-3}$ s^{-1} and remarkable TON of 2500.

Starting from the need to create an electron rich environment to stabilize high-valent intermediates, pentamethylcyclopentadienyl ligand-based-complexes was proposed by Crabtree et la in 2009.[35] Since donating ligands improve the catalytic activity, Cp*-iridium complexes becomes the deeper studied leading to $(Cp^*)Ir(dmiz)(OH)_2$ (where dmiz = 1,3-dimethylimidazole) showing turnover frequencies of 1.5 s^{-1} and TON of 2000 (Figure 1.9). [36] However, stability studies performed by Grotjahn et al bring to light the unstableness structural integrity. Electrochemical Quartz Crystal Nanobalance in water oxidizing conditions using CP-iridium complexes shows oxide nanoparticles deposited on the electrode leading to excellent catalytic performance.[37]

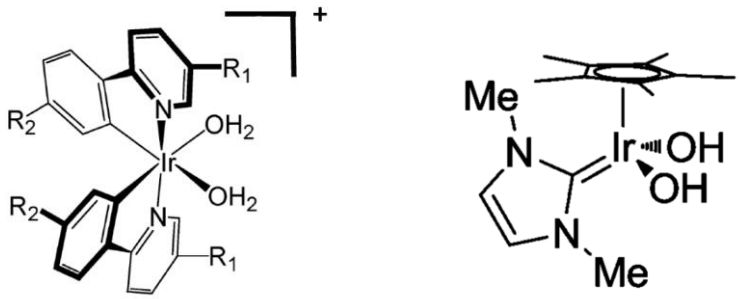

Figure 1.9. Drawn structure Left) of Ir-based catalyst described by Bernhard and co-workers.[34] The ligands can be R1=H, CH3 and R2=H, Ph, F, Cl Right) of $[(Cp^*)Ir(dmiz)(OH)_2]$[36]

Manganese-based WOCs

Manganese is the metallic active center on the OEC in PSII. For this reason, seems reasonable to take manganese as starting point for the WOC's search. In the other hand, its earth abundancy and nontoxic character inspire to be the ideal metallic based catalyst. Mimicking the nature system many manganese complexes have been studied.[38,39]

In 1999, Crabtree *et al.* reported the first binuclear complexes able to catalyze in homogeneous conditions the oxygen evolution reaction.[40] This complex is characterized by di-μ-oxo bridged Mn with typ ligand with the formula $[H_2O(terpy)Mn(\mu\text{-}O)_2Mn(terpy)OH_2](NO_3)_3$. The complex shows a TON of 4 after 6h employing NaClO as chemical oxidant. The aqua ligands present in the structure can be deprotonated to form a proposed Mn^V=O species by PCET. Experimental results show catalyst deactivation due to the dissociation of the complex in to MnO_4^-.

On the other hand, Dismukes et al. presented tetranuclear manganese complex inspired on the structure of the OEC in PSII (Figure 1.10), with formular $Mn_4O_4L_6$ where L=$(Ph)_2PO_2$, $(p\text{-}MePh)_2PO_2$, or $(p\text{-}MeOPh)_2PO_2$ able to evolve O_2 with the UV irradiation. [41–43]

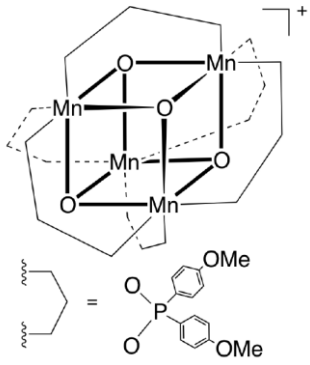

Figure 1.10. Drawn structure of $[Mn_4O_4((p\text{-}MePh)_2PO_2)_6]^+$ inspired on the structure of the OEC in PSII.

Cobalt-based WOCs

In the search of non-novel metals, researchers have been investigated molecular cobalt catalyst for water oxidation.[44–46] Berlinguette *et al*. have proposed an active water oxidation catalyst in basic media based on polypyridyl complex with formula $[Co(Py5)(OH_2)](ClO_4)_2$(Py5=2,6-(bis(bis-2-pyridyl)methoxy-methane)-pyridine). They have confirmed the oxygen formation with fluorescence optical probe at an applied potential of +1.59V vs NHE with a TOF of 79 s^{-1}.[47,48]

On the other hand, Nocera *et al.* have reported a series of Co hangman corroles complexes able to immobilize using Nafion membrane deposited on conducting fluorine doped tin oxide (FTO). The best performance were obtained with β-octofluoro Co(III) xanthene hangman corrole reaching a TOF of ~1s^{-1} at neutral pH.[44]

Iron -based WOCs

In the same line as Cobalt based WOC, the iron becomes an attractive metallic center as is not novel metal and is an earth abundant metal. In 2010, Bernhard and Collins reported a series of Fe-macrocyclic complexes with formula [Fe(III)(taml)]-, where taml = tetra-amido macrocyclic ligand, able to oxidize water to oxygen using Ce^{IV} as sacrificial oxidant. They have observed the electronic effect under metallic center by playing with electron donating and electron withdrawing groups.[49]

One year later, Lloret and Costas et al reported an Fe active catalyst series based on tetradentate ligands coordinated in cis configuration using Ce^{IV} or $NaIO_4$ as sacrificial oxidants.[50] The most active complex shows interesting TOF of 0.23 s^{-1}. The proposed factor responsible of the catalytic performance is summarized on the high valent Fe -oxo- specie able to form the O-O bond.

Heterogeneous WOC

Heterogenous catalyst have been extensively studied to take advantage of his higher stability and easier implementation in practical devices. Metal oxides have been investigated since 1960s. Most active catalyst are based on precious metals centers and requires in the case of the first transition metals high basic condition.

Iridium Oxide is one of the most efficient catalysts requiring low overpotential and able to work in acidic conditions. These was reported for first time by Grätzel et al. in 1978.[51] One year later, Grätzel *et al.* proposed ruthenium oxide in colloidal form as active water oxidation catalyst in presence of Ce^{IV}. These particles were also implemented in photo induced system employing $[Ru(bpy)_3]^{2+}$ as photosensitizer and dimethylviolegen as sacrificial oxidant.

Looking for cheapest based catalyst, researchers try to identify active oxides with Mn, Co, Fe, Ni or even mixing those. Along with other metal oxides, CoO_x has commonly been used as a cathode for electrochemical water splitting since the 1970s.[52] A remarkable example is known as CoPi reported by Nocera *et al*.[53] These consist of the use of CoO_x in a phosphate electrolyte at neutral pH where Pi anions is exclusively structural, in stabilizing the CoO_x catalytic domains to avoid Co leaching. This CoPi catalyst can be better described as layered CoOx with molecular dimensions, stabilized at neutral pH by the PO4 groups.[54] On the other hand, Galán-Mascarós *et al.* bring to light the electrocatalytic activity of Prussian blue derivative (PB) reporting $K_{2x}Co_{(3-x)}[Fe(CN)_6]_2$ (CoFe-PB) as WOC at acidic and neutral pH.[55] These shows a competitive performance in comparison with metal oxides showing, for example in comparison with cobalt oxide film at pH 7, a decrease of 105 mV of overpotential at TOF of 2.6×10^{-3} s^{-1}. On the other hand, these exhibit an unprecedent long-term stability persistent catalytic activity for weeks at neutral pH under ambient conditions.

Furthermore, manganese is one of the most studied metals to be water oxidation catalysts based on the photosynthetic organism to split water.[39,56] However, MnO_x catalysts involves lower activity due to stable formation of inactive MnO_2 domains and exhibit a

delicate stability regarding the instability of Mn^{3+} formed during the promotion of water oxidation.[57,58]

Leaving the metal oxides in band, an alternative strategy for search of earth-abundant an efficient catalyst consists of combine the use of polyoxometalate derivatives as molecular catalyst with conductive and protected matrices. The homogeneous catalyst becomes a starting point to immerse on the understanding of the water oxidation. However, the proposed catalysts have shown a deactivation and degradation issues due mainly to the organic ligand. For this reason, polyoxometalates as is described in next sections was proposed as molecular catalyst to introduce robustness substituting organic ligand by inorganic ligands. The heterogenization of homogeneous catalysts is already successfully done with precious metals-based catalyst.[59,60] Two strategies have been reported to achieve this mode operating: polymeric membrane (i.e Nafion) and conductive matrix (i.e Carbon Paste). The first one is demonstrated with cobalt cubane clusters incorporated onto hematite electrodes with Nafion containing ink resulting on a higher photocurrent.[61] The second one is reflected in the use of insoluble Cs^{+} or Ba^{2+} salts of cobalt containing polyoxometalates mixed with Carbon Paste.[62] This leads to high current at low overpotentials performance and involves stable behavior in long range of pH.

1.4. Polyoxometalate Chemistry

1.4.1. The POM's framework

Polyoxometalates (POMs) are polyoxoanion molecules built from high-valent metal oxides building blocks that are formed spontaneously in eater when either soluble molecular monomeric transition metal precursors or insoluble metal hydroxides or oxides are adjusted to the appropriate pH. POMs were discovered by the Spanish Delhuyar brothers in 1783.[63] Nevertheless, the popularity and development of POM chemistry do not start until the end of 20th century.

The general formula of POMs is $\{MO_x\}_n$, where M stands for the metal and x vary between 4 and 7. The most common POMs are based on molybdenum or tungsten in their highest oxidation state. These structures are defined by MOx polyhedral units with octahedral or tetrahedral shape sharing corners, edges, or faces. Structurally can be found two different types of oxygen atoms: terminal (M=O) and bridging (M-O-M). This later carry a greater negative charge becoming the most basic centers with easiness protonation character.

These clusters are controlled by electrostatic and radius-ratio principles also observed for extended ionic lattices.[64] POMs show extensive solution chemistry in aqueous and nonaqueous solvents due to theirs low surface charge densities responsible of weak anoint-cation attractions.

In 2010, Cronin et al.[65] reported a POM's review where polyoxometalate can be classified mainly into three families: (i) heteropolyanions, (ii) isopolyanions and (iii) molybdenum blue and molybdenum brown reduced POM clusters.

> *Heteropolyanions* is characterized to include one or several heteroatoms into metal oxide cluster. These heteroatoms are commonly elements from *p*- or *d*-block (i. e. P(V), Si(IV) or V(V)). This family shows hydrolytic stability over a wide pH range and becomes the most studied POMs. It highlighted archetypal Keggin $[XM_{12}O_{40}]^{n-}$ and Wells-Dawson $[X_2M_{18}O_{62}]^{n-}$ anions where M = W or

Mo and X = heteroatom (Figure 1.11). The robustness of tungsten-based POMs allows to form lacunary POMs with vacancies in their structure which gives high negative charge density making it ideal as inorganic ligands to stabilize transition metal complexes.

Isopolyanions consist of metal oxide cluster without any heteroatom into structure, Lindqvist archetype is an example (see figure 1.11) This results in lower stability compared to the heteropolyanion. Their high charges and strong basic oxygen character makes them attractive as building blocks.

Molybdenum blue and molybdenum brown reduced POM clusters consist in nanoscale structures with spherical shape based on molybdenum oxide blocks (Figure 1.11). Theirs structure has brought to light by Muller et al. in 1995 with a very-high-nuclearity cluster intertwining pentagonal building blocks {(Mo)Mo_5} resulting in a ring topology.

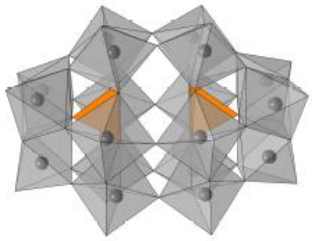

Wells-Dawson

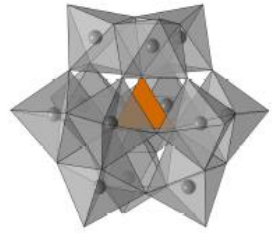

Keggin

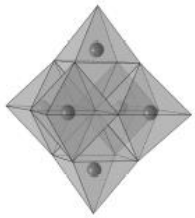

Lindqvist

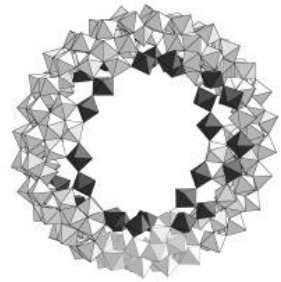

$\{Mo_{11}\}_{14}$

Figure 1.11. Schematic representation of Keggin $[XM_{12}O_{40}]^{n-}$,Wells-Dawson $[X_2M_{18}O_{62}]^{n-}$, Lindqvist $[M_6O_{19}]^{2-}$ and $\{Mo_{11}\}_{14}$.

The most studied archetype among polyoxometalates is the Keggin structure reported for the first time by J. F. Keggin in 1933.[66] This structure is known nowadays as α-Keggin and it has overall Td symmetry with a central XO_4 tetrahedron surrounded by twelve MO_6 octahedral units assembled together in four edge-sharing trimers. These M_3O_{12} trimers are linked to each other and to the central heteroatom by corner shared bridges.[67]

Rotation of three edge shared M_3O_{13} trimers rise to five different isomers so-called Baker Figgis isomers. Thus, when one of the trimers of α-Keggin is rotated 60º lead to β-Keggin reducing symmetry from T_d to C_{3v}. Rotation of 60º of a second trimer led to γ-Keggin with loss of symmetry to C_{2v}. The rotation of the third and fourth trimer yields to δ and ε Keggin isomers with C_{3v} and Td symmetry, respectively. Rotation of trimers involves a lower M-M distance and acute M-O-M angles, that confer lower stability due to coulombic repulsions. Theoretical DFT calculations computed the destabilization impact defining the following trend $\alpha < \beta < \gamma < \delta < \varepsilon$.

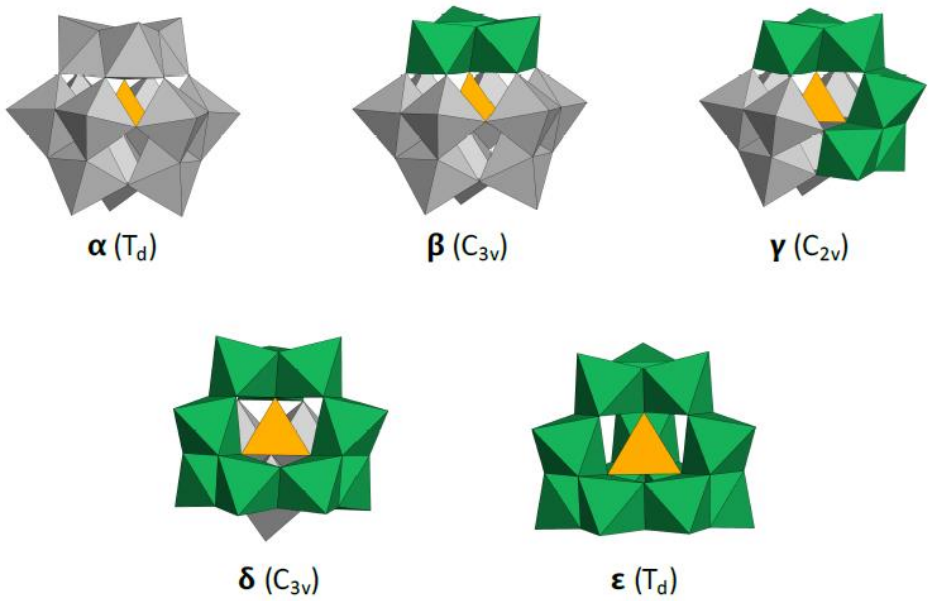

Figure 1.12. Polyhedral representation of isomers of the Keggin archetype. The rotated triads are highlighted in green.

Polyoxometalate are highlight of their stable behavior a wide range of pH from acid to moderate alkaline media. However, POM structure suffers a progressive degradation in alkaline media towards lacunary structures, where 1,2 or 3 $[MO_6]$ units have been detached. These vacancies can be filled with $[Mn^{+}=O]^{(n-2)+}$ fragments or organic groups. These lacunary species are interesting from a synthetic point because they are independently stable and isolable.

Focusing on the α-Keggin, the removal of one octahedral unit lead to the pentadentate monolacunary {α-XW11O39} archetype, whereas trilacunary species are formed either by losing three corners shared octahedral {α-XW9O34} leading to hexadentate ligand, or by removal of three edge-shared octahedral {β-XW9O34} leading to heptadenate ligand. Lacunary archetype involves an interesting inorganic ligand with multidentate attribute able to stabilize metal oxide frameworks or organic compounds. These give to POMs a huge range of potential applications such as magnetism, medicine, analysis, biochemistry, chirality, or material science.

Polyoxometalates have been used as catalyst in different reactions, for example: oxidation of aromatic hydrocarbons; olefin polymerization and epoxidation and Friedel-Crafts-type alkylation, acylation and sulfonation of aromatic compounds. As said before, POMs have shown a promising water oxidation catalyst.

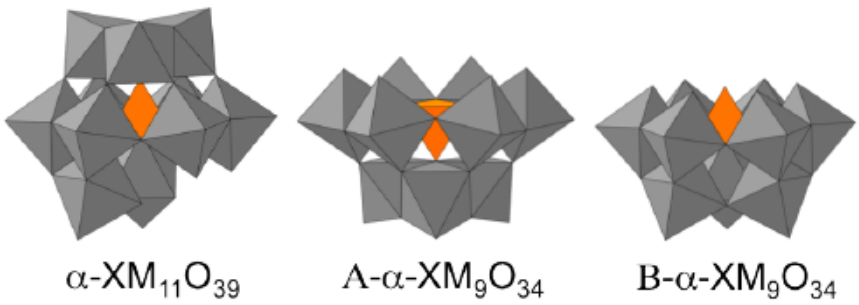

Figure 1.13. Polyhedral representation of lacunary α-Keggin species.

1.4.2. Polyoxometalate as Water oxidation Catalyst

During the last decade, POMs become very interesting candidates as water oxidation catalyst since they can serve as all-inorganic multidentate ligand to stabilize transition metal oxide clusters conferring high stability under strong conditions.[65,68,69]. On the other hand, POMs can assist on the deprotonation equilibria through the polyoxogenated surface acting as strong Bronsted acid. Furthermore, they mimic natural enzymes because can stabilize adjacent *d*-electrons through multiple-μ-hydroxo/oxo bridging units.

As mentioned before, the first POMs acting as remarkable water oxidation catalyst was reported in 2008 simultaneously and separately by Bonchio et al. and Hill et al.[70,71] In this case, the POM consists of tetraruthenate core $[Ru_4IV(-O)4(-OH)_2(H_2O)_4]^{6+}$ stabilized by two $[g\text{-}SiW_{10}O_{36}]^{8-}$ units with formula $[Ru_4(-O)_4(-OH)_2(H_2O)_4(\text{-}SiW_{10}O_{36})_2]_{10}$ (Ru_4Si). The ruthenium core has an adamantane-like arrangement with the four ruthenium atoms forming a tetrahedron. As shown in figure 1.14, the ruthenium centers are linked to the Keggin moieties by sharing vertexes.

The catalytic activity of Ru_4Si was tested using different chemical oxidants. Bonchio *et al.* evaluated performance using Cerium Ammonium Nitrate (CAN) in strong acidic media at 20ºC. They reached a TOF of 0.125 s^{-1} with an oxygen yield of 90% with respect to the oxidant. A second consecutive addition of CAN highlighted the stability of the catalyst under reaction conditions.[71] On the other hand, Hill et al. have used $[Ru(bpy)_3]^{3+}$ at pH 7 in dark conditions. In this case, due to the instability under oxidizing conditions of $[Ru(bpy)_3]^{3+}$. The same group have proved that the catalyst is stable in range of pH between 1.5 and 7.[72]

Voltametric characterization of Ru4Si estimated an overall 4-electron reduction potential ($Ru^{IV}{}_4$ to $Ru^{V}{}_4$) in 0.95V at neutral pH., whereas at the same pH the 4-electron oxygen evolution reaction at the same pH requires ca. 0.82 V. Thus, the reduction potential obtained with Ru_4Si is enough to empower water oxidation catalysis.

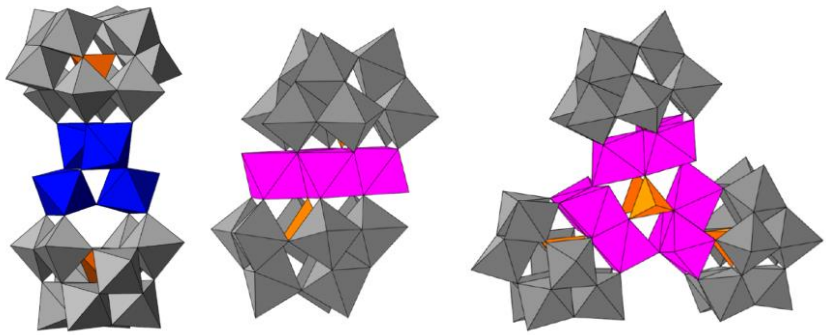

Figure 1.14. Polyhedral representation of (left) polyanion Ru_4 (middle) polyanion Co_4 (right) polyanion Co_9. The polytungstate fragments are shown as gray octahedra, heteroatom as orange tetrahedra, Ru as blue octahedra and Co as purpure octahedral.

The first non-precious noble metal catalysts came out in 2010, when Hill et al reported the water oxidation catalytic activity of the described tetracobalt-oxo-core sandwich type polyoxometalate with formula $[Co_4(H_2O)_2(a\text{-}PW_9O_{34})_2]^{10-}$ (Co_4) (Figure 1.14).[73] This consists in a central rhomb-like tetracobalt-oxo-core stabilized by sandwich structure with two trilacunary $[B\text{-}\alpha\text{-}PW_9O_{34}]^{9-}$ Keggin units. The four CoO_6 octahedral with coplanar cobalt atoms are linked to each other through oxo bridges by sharing edges. The cobalt disposition distinguishes two internal positions, and two external positions linked each one to a water molecule.

Hill *et al.* have evaluated the catalytic activity of Co_4 towards water oxidation catalysis using $[Ru(bpy)_3]^{3+}$ as chemical oxidant in a sodium phosphate buffer at pH 8. They have measured using gas chromatography the highest TOF (~$5s^{-1}$) observed for a molecular WOC at that time. Same research group have reported one year later, the catalytical activity under light-driven conditions using $[Ru(bpy)_3]^{3+}$ as photosensitiser and sodium persulfate as sacrificial electron acceptor in pH 8. The results show a better performance in comparison with Ru_4Si.[73]

Nevertheless, the polyoxometalate based on Co has generated a deep doubt in the real nature of the catalyst.[74–76] This is due Co^{2+} cations can be leached into aqueous solution

through the coordination equilibria. Thus, the aqueous cobalt cations, as well as, in situ generated CoO_x can be the true water oxidation species. Extra experiments have been required to confirm the true catalyst. Hill *et al*. have performed a series of experiments to demonstrate the negligible activity of aqueous cobalt cations and CoO_x.[73,77] This result was confirmed by Finke *et al*. through careful studies working at same conditions.[74,78] However, Finke et al. also proved with experimental evidence that CoO_x WOC film is formed in situ on the working electrode surface under oxidizing conditions. To verify the true catalyst inhibition strategy is necessary to transform the aqueous cobalt cations in inactive precipitate reacting with 2,2'-bipyridine (bpy).[75,78]

In 2012, Galán-Mascarós *et al.* reported the water oxidation catalytic activity of high nuclearity Co-POM with the formula $[Co_9(H_2O)_6(OH)_3(HPO_4)_2(PW_9O_{34})_3]^{16-}$ (**Co_9**).[79] This cluster was first described by Weakley *et al*. in 1984.[80] This polyanion contains three trilacunary {B-α-XW_9O_{34}} Keggin units with Co_3O_{12} moieties filling the vacant positions in each Keggin fragment Then, the three Co-Keggin fragments are interconnected by three hydroxyl bridges and two $[HPO_4]^{2-}$ anions forming a triangle of Triangles (Figure 1.14). Six of nine Co atoms archive their coordination sphere with terminal water molecules with a tendency to be oxidized. In comparison with the described Co_4, Co_9 structure involves hydroxyl bridges versus only oxo bridges, hydrogen phosphate bridges that are not embedded in the POM structure and higher percentage of terminal water molecules prone to be oxidized.

Galán-Mascarós *et al*. have evaluated the oxygen evolution reaction with the presence of 2,2'-bipyridyl (bpy) to avoid cobalt oxide formation during the OER. They have measured the efficiency using fluorescence probe reaching a 90% over an hour. Goberna *et al.* have reported the Co_9 stability along the pH range between 5.5 and 11.[81]

To take advantage from heterogeneous conditions, Galán-Mascarós *et al*. have reported a non-soluble Co_9 by adding CsCl to Co_9 aqueous solution.[62] Then, the Co_9 cesium salt (CsCo9) was incorporated into conductive matrix based on amorphous carbon paste. The electrocatalytic activity towards water oxidation at neutral pH shows a strong evolution reaction with a long-term stability. They were able to monitor the oxygen production

using fluorescence probe reaching 90% Faradaic efficiency. Post characterization of the recovered catalyst from the matrix confirms non-evidence of degradation. To confirm the true catalyst, analogous experiments with equimolar amounts of CoO_x show a lower current density confirming the real activity of $CsCo_9$. This attractive strategy allows to obtain robust electrodes by incorporating non-soluble homogenous WOCs into a solid-state matrix.

Inexpensive transition-metal cannot compete with noble metals in acidic media, where hydrogen production is easier and faster. Galán-Mascarós *et al*. reported in 2017 an unprecedent performance of Co_9 polyoxometalate in strong acidic conditions using modified electrodes of amorphous carbon paste.[82] They have evaluated the electrocatalytic activity of Cesium and Barium insoluble salt of Co_9 in comparison with IrO_2 in the identical working conditions. The $BaCo_9$ blend needs lower potentials in comparison with IrO_2 blend to reach the same current densities including a remarkable 246 mV difference for the onset potential of water oxidation. The excellent activity of $BaCo_9$ in comparison with $CsCo_9$ confirms a clear cation effect involving a remarkable decrease on onsetpotential. This gives to POMs an intrinsic feature to enhance the water oxidation performance. Extensive characterization of recovered catalyst has performed to confirm the stability and the real catalyst. On the other hand, Oxygen evolution showed Faradaic eficiency (>99%) for both Co-POM/CP electrodes, indicating a negligible contribution to the total measured currents from any other redox process. Last but not least, Carbon Paste shows a non-innocent role on the protection, stabilization, and enhancement POM activity. Recently, Galan et al. have gone deeper in the protective function essentially to the hydrophobicity environment, which avoids proper solvation of the catalysts, precluding its dissolution.[83]

1.5. Thesis goals and outline

The renewable energy becomes the key solution to cover the energy demands for human evolution and persevering the environmental equilibria of the world. Nevertheless, the intermittent character of renewable energy can be solved with a clean and attractive strategy based on store the energy into chemical bonds as splitting water in O_2 and H_2. Unfortunately, this later becomes a big challenge due to the limiting step of oxidation of water to O_2, making this strategy unviable from commercial point of view. The understanding and the search for cheap, effective, and robust catalyst for water oxidation becomes the greatest challenge that scientists are facing nowadays.

In this work we focus to understand the water oxidation catalysis performance of already reported Polyoxometalates based on earth-abundant transition metal. Moreover, we have contributed to shed some light into already reaction mechanism for the water oxidation reaction catalyzed by POMs based on earth-abundant transition metal.

In chapter 2 we have explored the activity and stability of several Co-POMs toward water oxidation in acidic media evaluating several features such as heteroatom composition, framework structure, net charge effect and Nuclearity.

In chapter 3 we have studied the electrocatalytic oxygen evolution reaction activity in neutral media of isostructural tetracobalt-oxo core POM (Co_4) based on Iron (Fe_4). On the other hand, we have investigated the reaction mechanism employing computational methods to determine the key aspects in comparison with those of the already well studied Co_4-WS.

In chapter 4 we have evaluated the possibility to use tetrairon-oxo core POM (Fe_4) in adverse conditions like in acidic media to be competitive with CO_9. Our results bright light the presence of a competitive electrochemical process involving carbon oxidation reaction given the formation of O_2 and CO_2.

This Thesis pick up specific concepts for the use of Earth-abundant based POMs in solid-state water oxidation catalysis and motivate to keep investigating to design a new cheapest and efficient catalyst based on Earth-abundant transition metals such as iron or Cobalt.

1.6. References

[1] U.S. Energy Information Administration, *Greenhouse gases' effect on climate - U.S. Energy Information Administration (EIA)*, **2021**.

[2] W. G. III, *Climate Change 2022: Mitigation of Climate Change*, **2022**.

[3] UNCTAD, *Global Carbon Project*, **2020**.

[4] NOAA National Centers for Environmental information, *Climate at a Glance: Global Time Series*, **2022**.

[5] J. A. Church, N. J. White, *Surv. Geophys.* **2011**, *32*, 585.

[6] N. Climate.gov, *Glacier mass balance*, **2020**.

[7] R. SCOTT, L. MICHON, *Sea ice extent in the Arctic at the end of the summer melt season each September from 1979–2021*.

[8] W. Steffen, K. Richardson, J. Rockstrom, S. E. Cornell, I. Fetzer, E. M. Bennett, R. Biggs, S. R. Carpenter, W. de Vries, C. A. de Wit, C. Folke, D. Gerten, J. Heinke, G. M. Mace, L. M. Persson, V. Ramanathan, B. Reyers, S. Sorlin, *Science (80-.).* **2015**, *347*, 1259855.

[9] J. Rockström, W. Steffen, K. Noone, Å. Persson, F. S. Chapin, E. F. Lambin, T. M. Lenton, M. Scheffer, C. Folke, H. J. Schellnhuber, B. Nykvist, C. A. de Wit, T. Hughes, S. van der Leeuw, H. Rodhe, S. Sörlin, P. K. Snyder, R. Costanza, U. Svedin, M. Falkenmark, L. Karlberg, R. W. Corell, V. J. Fabry, J. Hansen, B. Walker, D. Liverman, K. Richardson, P. Crutzen, J. A. Foley, *Nature* **2009**, *461*, 472.

[10] L. Persson, B. M. Carney Almroth, C. D. Collins, S. Cornell, C. A. de Wit, M. L. Diamond, P. Fantke, M. Hassellöv, M. MacLeod, M. W. Ryberg, P. Søgaard Jørgensen, P. Villarrubia-Gómez, Z. Wang, M. Z. Hauschild, *Environ. Sci. Technol.* **2022**, *56*, 1510.

[11] N. S. Lewis, D. G. Nocera, *Proc. Natl. Acad. Sci.* **2006**, *103*, 15729.

[12] M. Makešová, M. Valentová, *Energies* **2021**, *14*.

[13] International Renewable Energy Agency, *IRENA (2020), Global Renewables Outlook: Energy transformation 2050*, 2020th ed., Abu Dhabi.

[14] J. Barber, *Chem. Soc. Rev.* **2009**, *38*, 185.

[15] R. E. Blankenship, H. Hartman, *Trends Biochem. Sci.* **1998**, *23*, 94.

[16] J. P. McEvoy, G. W. Brudvig, *Chem. Rev.* **2006**, *106*, 4455.

[17] M. P. Johnson, *Essays Biochem.* **2016**, *60*, 255.

[18] N. Nelson, A. Ben-Shem, *Nat. Rev. Mol. Cell Biol.* **2004**, *5*, 971.

[19] L. N. M. DUYSENS, J. AMESZ, B. M. KAMP, *Nature* **1961**, *190*, 510.

[20] G. Ciamician, *Science (80-.).* **1912**, *36*, 385.

[21] M. Venturi, V. Balzani, M. T. Gandolfi, G. Ciamician, **2005**.

[22] Y. Umena, K. Kawakami, J.-R. Shen, N. Kamiya, *Nature* **2011**, *473*, 55.

[23] K. N. Ferreira, T. M. Iverson, K. Maghlaoui, J. Barber, S. Iwata, *Science (80-.).* **2004**, *303*, 1831.

[24] H. B. and R. M. (IRENA) and M. C. Emanuele Taibi, *Green Hydrogen Cost Reduction: Scaling up Electrolysers to Meet the 1.5^{0}C Climate Goal*, Abu Dhabi, **2020**.

[25] S. W. Gersten, G. J. Samuels, T. J. Meyer, *J. Am. Chem. Soc.* **1982**, *104*, 4029.

[26] Z. Deng, H.-W. Tseng, R. Zong, D. Wang, R. Thummel, *Inorg. Chem.* **2008**, *47*, 1835.

[27] M. H. V Huynh, T. J. Meyer, *Chem. Rev.* **2007**, *107*, 5004.

[28] J. L. Cape, J. K. Hurst, *J. Am. Chem. Soc.* **2008**, *130*, 827.

[29] F. Liu, J. J. Concepcion, J. W. Jurss, T. Cardolaccia, J. L. Templeton, T. J. Meyer,

Inorg. Chem. **2008**, *47*, 1727.

[30] B. Limburg, E. Bouwman, S. Bonnet, *Coord. Chem. Rev.* **2012**, *256*, 1451.

[31] C. Sens, I. Romero, M. Rodríguez, A. Llobet, T. Parella, J. Benet-Buchholz, *J. Am. Chem. Soc.* **2004**, *126*, 7798.

[32] F. Bozoglian, S. Romain, M. Z. Ertem, T. K. Todorova, C. Sens, J. Mola, M. Rodríguez, I. Romero, J. Benet-Buchholz, X. Fontrodona, C. J. Cramer, L. Gagliardi, A. Llobet, *J. Am. Chem. Soc.* **2009**, *131*, 15176.

[33] S. Romain, F. Bozoglian, X. Sala, A. Llobet, *J. Am. Chem. Soc.* **2009**, *131*, 2768.

[34] N. D. McDaniel, F. J. Coughlin, L. L. Tinker, S. Bernhard, *J. Am. Chem. Soc.* **2008**, *130*, 210.

[35] J. F. Hull, D. Balcells, J. D. Blakemore, C. D. Incarvito, O. Eisenstein, G. W. Brudvig, R. H. Crabtree, *J. Am. Chem. Soc.* **2009**, *131*, 8730.

[36] D. G. H. Hetterscheid, J. N. H. Reek, *Chem. Commun.* **2011**, *47*, 2712.

[37] D. B. Grotjahn, D. B. Brown, J. K. Martin, D. C. Marelius, M.-C. Abadjian, H. N. Tran, G. Kalyuzhny, K. S. Vecchio, Z. G. Specht, S. A. Cortes-Llamas, V. Miranda-Soto, C. van Niekerk, C. E. Moore, A. L. Rheingold, *J. Am. Chem. Soc.* **2011**, *133*, 19024.

[38] S. Mukhopadhyay, S. K. Mandal, S. Bhaduri, W. H. Armstrong, *Chem. Rev.* **2004**, *104*, 3981.

[39] M. Wiechen, H.-M. Berends, P. Kurz, *Dalt. Trans.* **2012**, *41*, 21.

[40] J. Limburg, J. S. Vrettos, L. M. Liable-Sands, A. L. Rheingold, R. H. Crabtree, G. W. Brudvig, *Science (80-.).* **1999**, *283*, 1524.

[41] W. F. Ruettinger, C. Campana, G. C. Dismukes, *J. Am. Chem. Soc.* **1997**, *119*, 6670.

[42] W. F. Ruettinger, D. M. Ho, G. C. Dismukes, *Inorg. Chem.* **1999**, *38*, 1036.

[43] and G. C. D. M. Yagi, K. V. Wolf, P. J. Baesjou, S. L. Bernasek, *Angew. Chem.* **2001**, *40*, 2925.

[44] D. K. Dogutan, R. J. McGuire, D. G. Nocera, *J. Am. Chem. Soc.* **2011**, *133*, 9178.

[45] M. Natali, I. Bazzan, S. Goberna-Ferrón, R. Al-Oweini, M. Ibrahim, B. S. Bassil, H. Dau, F. Scandola, J. R. Galán-Mascarós, U. Kortz, A. Sartorel, I. Zaharieva, M. Bonchio, *Green Chem.* **2017**, *19*, 2416.

[46] T. Abe, K. Nagai, S. Kabutomori, M. Kaneko, A. Tajiri, T. Norimatsu, *Angew. Chem. Int. Ed. Engl.* **2006**, *45*, 2778.

[47] D. J. Wasylenko, R. D. Palmer, E. Schott, C. P. Berlinguette, *Chem. Commun.* **2012**, *48*, 2107.

[48] D. J. Wasylenko, C. Ganesamoorthy, J. Borau-Garcia, C. P. Berlinguette, *Chem. Commun.* **2011**, *47*, 4249.

[49] W. C. Ellis, N. D. McDaniel, S. Bernhard, T. J. Collins, *J. Am. Chem. Soc.* **2010**, *132*, 10990.

[50] J. L. Fillol, Z. Codolà, I. Garcia-Bosch, L. Gómez, J. J. Pla, M. Costas, *Nat. Chem.* **2011**, *3*, 807.

[51] J. Kiwi, M. Grätzel, *Angew. Chemie Int. Ed. English* **1978**, *17*, 860.

[52] J. R. Galán-Mascarós, *ChemElectroChem* **2015**, *2*, 37.

[53] Y. Surendranath, M. Dinca, D. G. Nocera, *J. Am. Chem. Soc.* **2009**, *131*, 2615.

[54] M. W. Kanan, J. Yano, Y. Surendranath, M. Dincă, V. K. Yachandra, D. G. Nocera, *J. Am. Chem. Soc.* **2010**, *132*, 13692.

[55] S. Pintado, S. Goberna-Ferrón, E. C. Escudero-Adán, J. R. Galán-Mascarós, *J. Am. Chem. Soc.* **2013**, *135*, 13270.

[56] Y. Matsumoto, E. Sato, *Electrochim. Acta* **1979**, *24*, 421.

[57] A. Bergmann, I. Zaharieva, H. Dau, P. Strasser, *Energy Environ. Sci.* **2013**, *6*, 2745.

[58] T. Takashima, K. Hashimoto, R. Nakamura, *J. Am. Chem. Soc.* **2012**, *134*, 1519.

[59] F. M. Toma, A. Sartorel, M. Iurlo, M. Carraro, P. Parisse, C. Maccato, S. Rapino, B. R. Gonzalez, H. Amenitsch, T. Da Ros, L. Casalis, A. Goldoni, M. Marcaccio, G. Scorrano, G. Scoles, F. Paolucci, M. Prato, M. Bonchio, *Nat. Chem.* **2010**, *2*, 826.

[60] M. Quintana, A. M. López, S. Rapino, F. M. Toma, M. Iurlo, M. Carraro, A. Sartorel, C. Maccato, X. Ke, C. Bittencourt, T. Da Ros, G. Van Tendeloo, M. Marcaccio, F. Paolucci, M. Prato, M. Bonchio, *ACS Nano* **2013**, *7*, 811.

[61] B. Zhang, F. Li, F. Yu, X. Wang, X. Zhou, H. Li, Y. Jiang, L. Sun, *ACS Catal.* **2014**, *4*, 804.

[62] J. Soriano-López, S. Goberna-Ferrón, L. Vigara, J. J. Carbó, J. M. Poblet, J. R. Galán-Mascarós, *Inorg. Chem.* **2013**, *52*, 4753.

[63] F. C. Delhuyar Lubice, J. J. & Delhuyar Lubice, *Análisis químico del wolfram y examen de un nuevo metal que entra en su composición*, **1783**.

[64] F. M. Toma, A. Sartorel, M. Iurlo, M. Carraro, S. Rapino, L. Hoober-Burkhardt, T. Da Ros, M. Marcaccio, G. Scorrano, F. Paolucci, M. Bonchio, M. Prato, *ChemSusChem* **2011**, *4*, 1447.

[65] D.-L. Long, R. Tsunashima, L. Cronin, *Angew. Chem. Int. Ed. Engl.* **2010**, *49*, 1736.

[66] J. F. KEGGIN, *Nature* **1933**, *131*, 908.

[67] M.T. Pope, *Heteropoly and Isopoly Oxometalates* (Ed.: Springer Berlin, H.), **1983**.

[68] M. T. Pope, A. Müller, **2002**.

[69] D.-L. Long, E. Burkholder, L. Cronin, *Chem. Soc. Rev.* **2007**, *36*, 105.

[70] Y. V. Geletii, B. Botar, P. Kögerler, D. A. Hillesheim, D. G. Musaev, C. L. Hill, *Angew. Chemie Int. Ed.* **2008**, *47*, 3896.

[71] A. Sartorel, M. Carraro, G. Scorrano, R. De Zorzi, S. Geremia, N. D. McDaniel, S. Bernhard, M. Bonchio, *J. Am. Chem. Soc.* **2008**, *130*, 5006.

[72] Y. V Geletii, C. Besson, Y. Hou, Q. Yin, D. G. Musaev, D. Quiñonero, R. Cao, K. I. Hardcastle, A. Proust, P. Kögerler, C. L. Hill, *J. Am. Chem. Soc.* **2009**, *131*, 17360.

[73] Q. Yin, J. M. Tan, C. Besson, Y. V Geletii, D. G. Musaev, A. E. Kuznetsov, Z. Luo, K. I. Hardcastle, C. L. Hill, *Science (80-.).* **2010**, *328*, 342 LP.

[74] J. J. Stracke, R. G. Finke, *ACS Catal.* **2014**, *4*, 79.

[75] J. J. Stracke, R. G. Finke, *ACS Catal.* **2013**, *3*, 1209.

[76] M. Natali, S. Berardi, A. Sartorel, M. Bonchio, S. Campagna, F. Scandola, *Chem. Commun.* **2012**, *48*, 8808.

[77] J. W. Vickers, H. Lv, J. M. Sumliner, G. Zhu, Z. Luo, D. G. Musaev, Y. V Geletii, C. L. Hill, *J. Am. Chem. Soc.* **2013**, *135*, 14110.

[78] J. J. Stracke, R. G. Finke, *J. Am. Chem. Soc.* **2011**, *133*, 14872.

[79] S. Goberna-Ferrón, L. Vigara, J. Soriano-López, J. Ramón Galán-Mascarós, *Inorg. Chem.* **2012**, *51*, 11707.

[80] T. J. R. Weakley, *J. Chem. Soc.{,} Chem. Commun.* **1984**, 1406.

[81] S. Goberna-Ferrón, J. Soriano-López, J. R. Galán-Mascarós, M. Nyman, *Eur. J. Inorg. Chem.* **2015**, *2015*, 2833.

[82] M. Blasco-Ahicart, J. Soriano-López, J. J. Carbó, J. M. Poblet, J. R. Galan-Mascaros, *Nat. Chem.* **2017**, *10*, 24.

[83] J. Yu, F. A. Garcés-Pineda, J. González-Cobos, M. Peña-Díaz, C. Rogero, S. Giménez, M. C. Spadaro, J. Arbiol, S. Barja, J. R. Galán-Mascarós, *Nat. Commun.* **2022**, *13*, 1.

Chapter 2

Water oxidation electrocatalysis in acidic media with Co-containing polyoxometalates

2.1. Introduction

The use of renewable energy source, such as solar energy, is a suitable, sustainable strategy to satisfy the world's energy demand in the long term. Its storage into chemical bonds is a smart strategy to overcome the intrinsic intermittency of renewable source.[1] In the chemical storage, electrochemical water splitting has become the feasible choice. Water as clean fuel is used to store electrical energy in H_2 and O_2 bonds. This process involves the oxidation of water producing molecular oxygen (Oxygen Evolution Reaction OER) and, at the same time, the reduction of protons to molecular hydrogen (Hydrogen Evolution Reaction HER). Both processes are thermodynamically proton dependent of 59 mV per unit of pH. On the other hand, the water oxidation half reaction to produce O_2 is thermodynamically and kinetically energy demanding. On this regard, OER is commonly considered as the bottleneck of the whole process.

$$2H_2O \rightleftharpoons O_2 + 4H^+ + 4e^- \qquad E^0_{anode} = 1.23 - 0.059 \cdot pH\ (V\ vs\ NHE)\ (Eq.2.1)$$

$$4H^+ + 4e^- \rightleftharpoons 2H_2 \qquad E^0_{cathode} = 0.00 - 0.059 \cdot pH\ (V\ vs\ NHE)\ (Eq.2.2)$$

Water electrolysis would be highly preferred in acidic conditions where hydrogen production is favored due to high proton concentration, and proton exchange membranes are able to support high currents (> 1 $A \cdot cm^{-2}$) minimizing crossover and resistance loses.[2,3] Unfortunately, only noble metals are able to promote electrocatalytically processes in these conditions. This is especially relevant for the water oxidation reaction at the anode, where IrO_2 and RuO_2,[4] appear as the only options. Therefore, there is still a need for a low-cost WOC active in acidic conditions.

Many oxides of earth abundant metals are efficient heterogeneous WOCs in alkaline electrolyte.[5–12] Nevertheless, their catalytic performance decreases when lowering the pH, and most of them rapidly dissolve even in mildly acidic media.[13,14] Only some cobalt and manganese oxides have shown catalytic activity in such demanding conditions.[15–20] Even still, their performance is not sufficient of earth abundant WOCs are needed.[21]

Water oxidation electrocatalysis in acidic media with Co-containing polyoxometalates

As alternative to oxides, polyoxometalates (POMs) has become the key point to develop WOCs based on earth abundant metals working in drastically acidic condition. POMs are characterized by their rich redox chemistry since they can stabilize high-valent intermediates because of their multiple-μ-hydroxo/oxo bridging units. Moreover, they can be immobilized into modified electrodes working as heterogeneous water oxidation catalysts. In spite of low electrical conductivity, POMs can be introduced in conductive matrix material.

Since 2008, many conductive matrix and strategy have proposed to immobilize POMs. The Bonchio and co-workers were the pioneers in this strategy.[22] They have reported a high catalytic water oxidation improvement by incorporating a $Li_{10}[Ru_4(\mu\text{-}OH)_2(H_2O)_4(g\text{-}SiW_{10}O_{36})_2]$ (Ru_4) to carbon nanotubes decorated previously by poly(amidoamine ammonium) dendrimers (PAMAM). These modified electrodes were prepared by drop-casting onto an ITO electrode showing high surface area, good mechanical properties and good thermal stability. The same group has published three years later a graphene-functionalized nanosheet with Ru4. In this case, the conductive source was pristine graphite which was functionalized with PAMAM via 1,3-dipolar cyclo-addition and then Ru4 was incorporated electrostatically.[23]

In the search for the new WOCs based on abundant raw materials, polyoxometalate are promising candidates. Particularly, cobalt-containing polyoxometalate (Co-POM) have shown encouraging homogenous catalytic performance in close-to-neutral pH[24–27] with confirmed stability under controlled working conditions.[28–31]

Hill et al. reported in 2010, the first example of Co-POM as water oxidation catalyst in homogenous conditions, where [Ru(bpy)3]3+ (bpy is 2,2'-bipyridine) is used as the oxidant.[24] Two years later, Galan and collaborators discovered a remarkable cobalt containing POM as water oxidation catalyst at neutral pH.[26] Despite the hydrolytic and oxidative stability of the POM, the solution equilibria of Co-POM liberate Co^{2+} traces that give rise to oxide species. These oxides in the form of films compete with POM in certain conditions.

Regarding this, heterogeneous electrocatalytic water oxidation seems the key point to avoid the metal leaching due to the chemical equilibria process. Xie group published the first Co-POM modified electrode in 2012.[32] They have immobilized the $[Co_4(H_2O)_2(PW_9O_{34})_2]^{10-}$ ($Co_4P_2W_{18}$) in ordered mesoporus carbon nitride (MCN). In this case, the strategy followed to link the catalyst and the conductive matrix is based specially of the presence of group's $–NH_2$/–NH, that could be protonated providing cationic groups used as electrostatic anchor to immobilize the anionic Co_4 POM.

One year later, Galán-Mascarós et al. published the activity of a water oxidation modified electrode based on a conducting matrix of amorphous carbon paste (CP) and $Cs_{15}K[Co_9(H_2O)_6(OH)_3(HPO_4)_2(PW_9O_{34})_3]$ (**$CsCo_9$**) water-insoluble salt. [33] The modified electrodes were prepared by mechanically mixing the cesium POM salt with carbon paste conducting matrix. Then, the blend was filled into electrode pocket. These electrodes show a remarkable stability with any signs of fatigue during at least 8 hours. Furthermore, faradaic O2 evolution efficiency was above 90%. Moreover, this strategy confers a robust performance in large pH range and protect the POM catalyst in drastic acidic media where metal oxides are unstable. In order to determine the nature of the true catalyst, they performed experiments with CoO_x. The electrocatalytically performance discovered for CoO_x differs significantly from the CsCo9. This difference was even higher at low pH where the metal oxides are unstable.

Regarding the features observed working with the carbon paste modified electrode, Galán-Mascarós's group recently contributed to the major technology challenge. They promote a viable strategy to successfully catalyze water oxidation in acidic media with Co-POMs by taking advantage of the insolubility of the corresponding heavy alkaline and alkaline-earth cation salts, and of the protecting role of a partially hydrophobic carbon paste electrode support.[34] Salts of $[Co_9(H_2O)_6(OH)_3(HPO_4)_2(PW_9O_{34})_3]^{16-}$ (Co_9) showed promising performance for the electrocatalytic water oxidation in such conditions.[30] They presented the Co_9 with Barium counteraction ($BaCo_9$) as an alternative to the state of-the-art IrO_2 based on the excellent and unparalleled performance of $BaCo_9$ in sulfuric acid solution (1M). They carried out the same experiments with different catalyst content incorporating IrO_2 in Carbon Paste

environment to reach a real comparison. Independently if the electrocatalytic activity is compared taking account the catalyst content in weigh or total number of possible active sites, the results show a clear superior performance of $BaCo_9$. They have confirmed this excellent performance reporting >99% Faradaic efficiency and carefully characterization before and after electrolysis without observing any significant change. On the other hand, they have discovered a counter cation effect in the Co_9 POM performance.

In this chapter, we present a complete series of catalytic studies with multiple Co-POMs following the same working electrode strategy. We selected a variety of different structural types and composition. The corresponding water-insoluble salts were used to prepare the CP modified electrodes to promote water oxidation in acidic conditions. Our results allow us to correlate POM structure and composition with activity, establishing the major requirements for a Co-POM to deliver high activity and robust performance for acidic water electrolysis.

2.2. Results and Discussion

Our previous results with $[Co_9(H2O)_6(OH)_3(HPO_4)_2(PW_9O_{34})_3]^{16-}$ (Co_9) salts in acidic water oxidation catalysis led to additional questions, such as if Co_9 is unique or if other Co-POMs may offer analogous performance. And if so, what is the effect of POM structure and composition? We decided to test six additional Co- POMs with different nuclearity, charge, or heteroatom (Figure 1). We selected the tetrameric $[Co_4(H_2O)_2(PW_9O_{34})_2]^{10-}$ ($Co_4P_2W_{18}$), deeply studied as WOCs in homogeneous conditions[19] and its analogs $[Co_4(H_2O)_2(SiW_9O_{34})_2]^{12-}$ ($Co_4Si_2W_{18}$) and $[Co_4(H_2O)_2(P_2W_{15}O_{56})_2]10-$ ($Co_4P_4W_{30}$), both with the same active Co4 core, but with SiIV ($Co_4Si_2W_{18}$) or with Dawson-Wells ligands ($Co_4P_4W_{30}$) instead of the smaller Keggin moieties. Finally, we investigated the three monosubstituted Keggin POMs $[Co(H_2O)(PW_{11}O_{39})]^{5-}$ ($CoPW_{11}$), $[Co(H_2O)(SiW_{11}O_{39})]^{6-}$ ($CoSiW_{11}$) and $[Co(H_2O)$-$(CoW_{11}O_{39})]^{7-}$ ($CoCoW_{11}$), with the analogous catalytically active $[(H_2O)Co^{II}O_5]$ center on the surface, and a different internal heteroatom P^V, Si^{IV} or Co^{III} in the tetrahedral position.

All compounds were synthesized following reported procedures and the Cs^+ and Ba^{2+} water-insoluble salts were obtained by metathesis. The water-insoluble salts were blended with commercial carbon paste (CP) to obtain modified electrodes to be used as anodes.

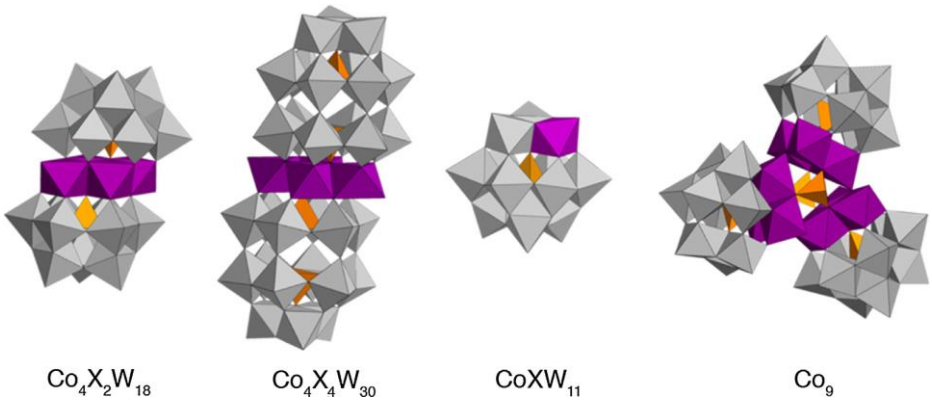

Figure 2.1. Polyhedral representation of (from left to right): $[Co_4(H_2O)_2(XW_9O_{34})_2]^{n-}$ (X = P^V or Si^{IV}) ($Co_4X_2W_{18}$), $[Co_4(H_2O)2(P_2W_{15}O_{56})_2]^{16-}$ ($Co_4X_4W_{30}$), $[Co(H_2O)$-$(XW_{11}O_{39})]^{m-}$ (X = P^V, Si^{IV} and Co^{III}) (CoXW11) and $[Co_9(H2O)$-$_6(OH)_3(HPO_4)_2(PW_9O_{34})_3]^{16-}$ (Co_9). Label: Co (purple octahedra), X or P (orange tetrahedra) and W (grey octahedra)

2.2.1. Electrochemical stability

At first glance, from standard 30% POM electrodes, we rapidly noticed that not all the Co-POMs tested were chemically stable during acidic water oxidation. This is the case for $CoSiW_{11}$, $CoCoW_{11}$ and $Co_4Si_2W_{18}$. Their Linear sweep voltammetry data changes dramatically for very short periods of time, with the appearance of a significant pre-catalytic event after just one cycle (Figure 2.2)

This precatalytic event has been identified as the electrochemical signature for the presence of CoO_x in these conditions.[10] Anions with high charge density ratio are, in general, less stable.[35,36] This phenomenon is strictly associated with the charge-to-metal (q/M) ratio in these polyanions, where q is the overall negative charge of the anion and M is the number of metal atoms present in the structure. The q/M ratio has been previously employed as a chemical descriptor to rationalize the reactivity, redox properties and protonation degree of POMs.[36] Our results show how those POMS with higher q/M values are unstable under acidic water oxidation conditions, even when protected by the carbon paste support. This is the case for $Co_4Si_2W_{18}$ vs $Co_4P_2W_{18}$, with q/M values of 0.545 and 0.455, respectively. And also, for $CoSiW_{11}$ and $CoCoW_{11}$ vs $CoPW_{11}$, with q/M values 0.538, 0.500 and 0.417, respectively. Despite its instability, these Si and Co derivatives should be more active towards OER, based in the same rationale. We previously showed how increasing the q/M ration of Co_9 by substitution of the three P (V) heteroatoms for Ge (IV) increases the energy of the set of the occupied molecular orbitals yielding to a lower oxidation potential of the reactive site Co (II)–OH_2, and ultimately a lower onset WOC overpotential.[37]

Thus, the presence of P with a + 5 oxidation state as heteroatom is a key feature for the stability of the Co-POM structure since the analogous compounds $Co_4P_2W_{18}$ and $CoPW_{11}$ were stable in the long term. Hence, $Co_4Si_2W_{18}$, $CoSiW_{11}$ and $CoCoW_{11}$ will be omitted for the rest of the comparative analysis.

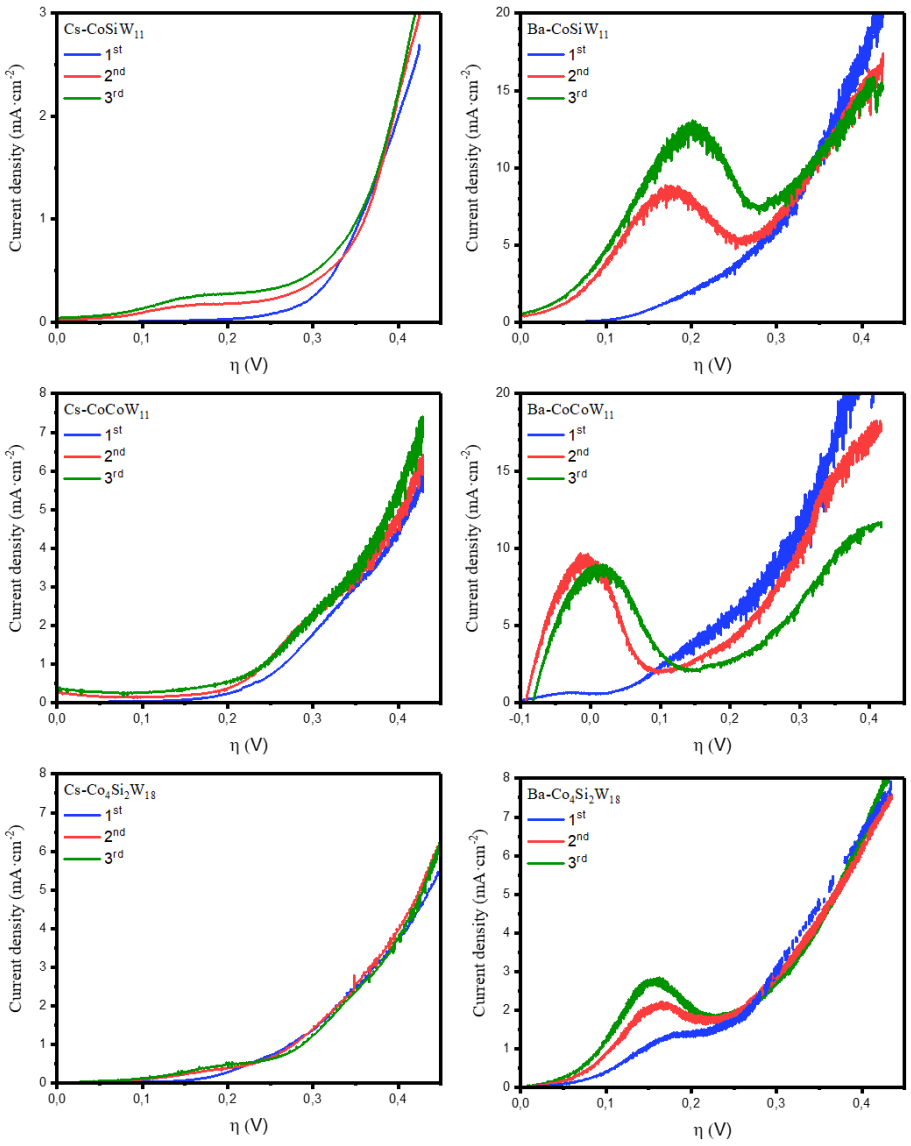

Figure 2.2. Linear sweep voltammetry in H_2SO_4 (1 M) solution with a blend working electrode for 30% catalyst contents: (i) Cs-$CoSiW_{11}$/CP (ii) Ba-$CoSiW_{11}$/CP (iii) Cs-$CoCoW_{11}$/CP (iv) Ba-$CoCoW_{11}$/CP (v) Cs- $Co_4Si_2W_{18}$/CP (vi) Ba-$Co_4Si_2W_{18}$/CP.

We further analyzed the stability of the Co-POM/CP electrodes in chronopotentiometry measurements (Figure 2.3). All compounds with good initial stability, also showed good long-term stability at 1 mA·cm^{-2}, maintaining the consistent overpotentials for at least two hours. It is worth mentioning that this time limit is determined by the instability of

the carbon paste electrodes, not because of catalytic issues. During water oxidation experiments, these electrodes accumulate electrostatic charges resulting in the expulsion of the paste blend from the electrode pocket. It is interesting to note that some different trends are apparent: most blends show small increments in overpotentials, while Cs-Co_9, Ba-$Co_4P_2W_{18}$ and Ba-Co_9 slightly improve their catalytic activity over this time.

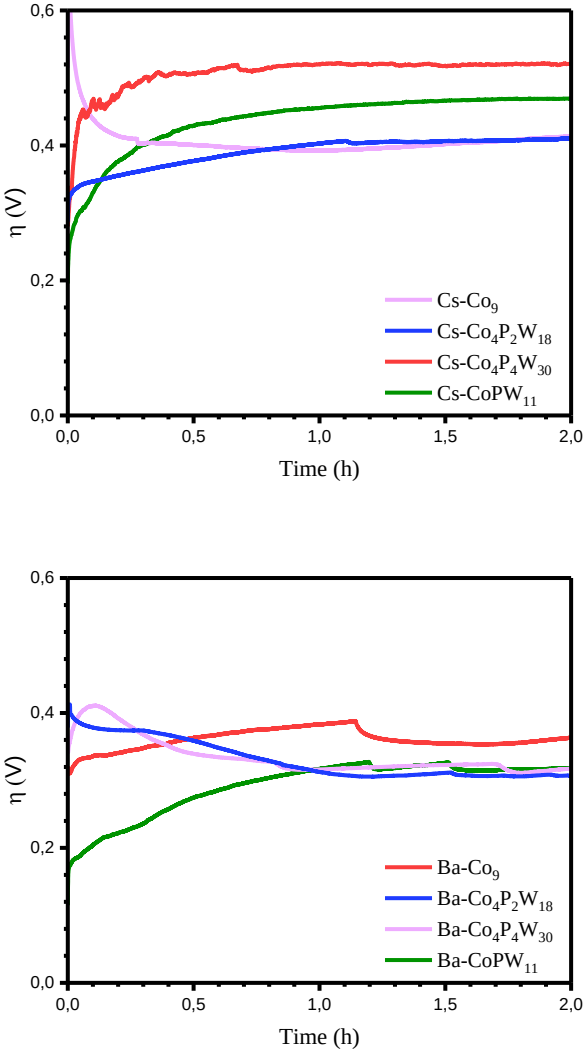

Figure 2.3. Chronopotentiometry data in H_2SO_4 (1 M) solution at a constant current density of 1mA·cm^{-2} with (a) 30% Cs-POM/CP blends with a porous frit on the tip and (b) 30% Ba-POM/CP blends. Data collected with a regular working electrode (surface area = 0.07 cm^2) in an H-cell under magnetic stirring.

2.2.2. Electrochemical performance

In general, the catalytic activity of the stable Co-POM/CP electrodes (Co_9, $Co_4P_2W_{18}$, $CoPW_{11}$ and $Co_4P_4W_{30}$) increases with catalyst content (Figure 2.4), but at the cost of poorer mechanical stability.

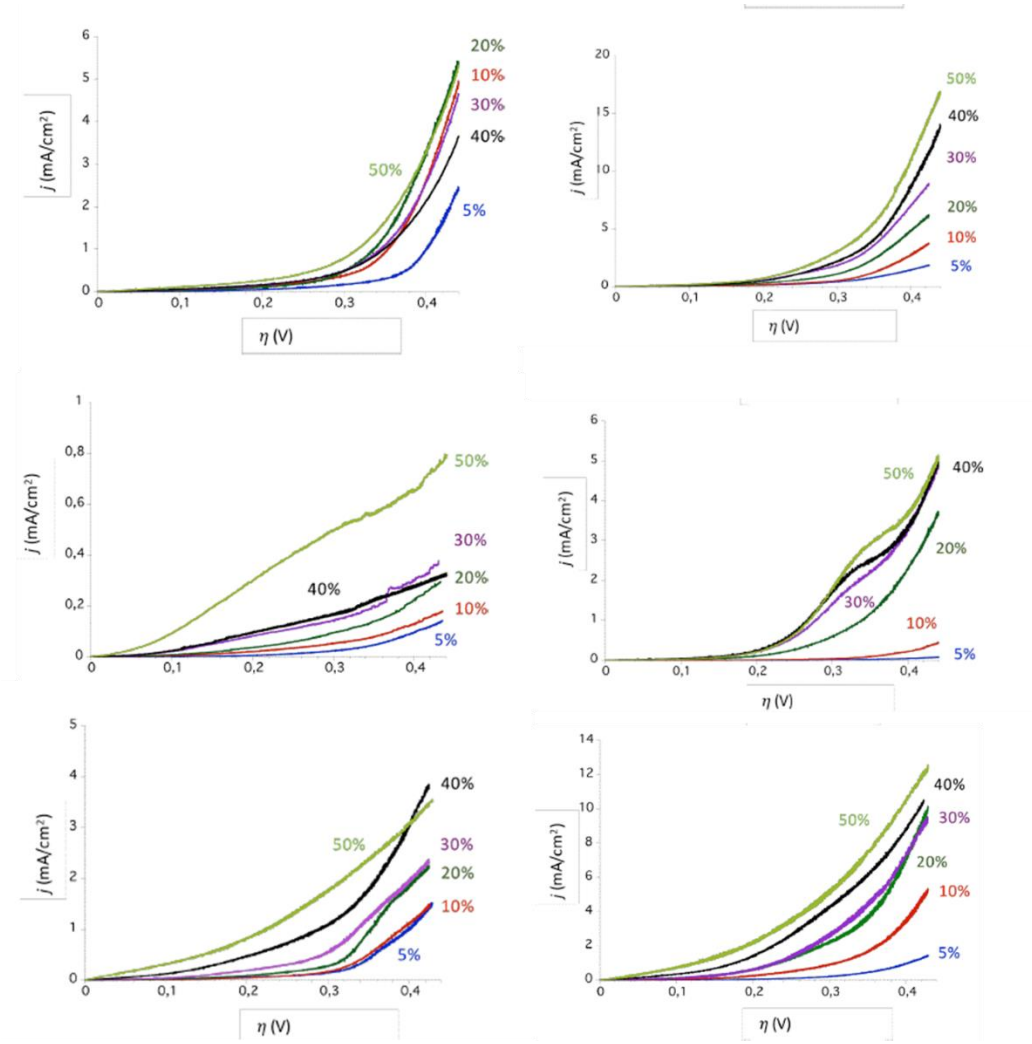

Figure 2.4. Linear sweep voltammetry in H_2SO_4 (1 M) solution with a blend working electrode for different % catalyst contents: (i) Cs-$Co_4P_2W_{18}$/CP (ii) Ba-$Co_4P_2W_{18}$/CP (iii) Cs-$Co_4P_4W_{30}$/CP (iv) Ba-$Co_4P_4W_{30}$/CP (v) Cs-$CoPW_{11}$/CP (vi) Ba-$CoPW_{11}$/CP.

For a given catalyst content, barium salts reach higher current densities than the cesium counterparts for all Co-POM types (Figure 2.5). This is especially significant for the Dawson-Wells derivative. Cs-$Co_4P_4W_{30}$ shows almost negligible electrocatalytic current, whereas Ba-$Co_4P_4W_{30}$ shows remarkable performance. Interestingly, all Keggin-derivatives exhibit almost identical onset overpotential of ~ 100 mV, reaching 10 $mA \cdot cm^{-2}$ well below 400 mV overpotential. In terms of maximum current densities, the electrocatalytic activity for these electrodes with same Co-POM content per weight follows the trend Co_9 > $Co_4P_2W_{18}$ > $CoPW_{11}$ > $Co_4P_4W_{30}$ regardless the countercation.

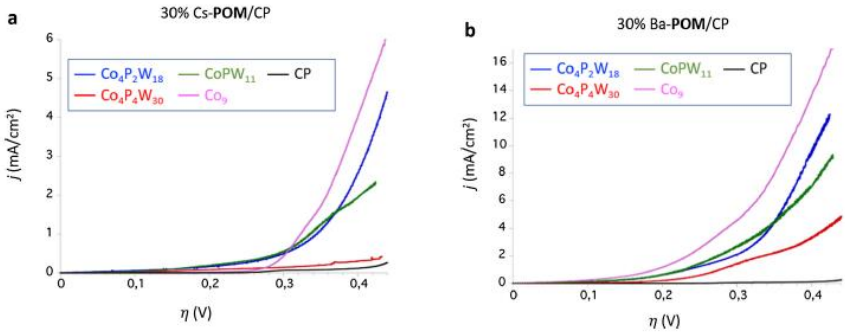

Figure 2.5. Linear sweep voltammetry in H_2SO_4 (1 M) solution with 30% Co-POM/CP blend working electrodes: (a) Cs-POM/CP blends; (b) Ba-POM/CP blends. Data collected with an RDE (surface area = 0.07 cm^2) at 500 rpm and with a 1 mV/s scan rate.

Of course, this weighted comparison is very significant for applications, but to understand better the origin of this different activity we decided to normalize the electrochemical data by the total number of moles of catalyst (Figure 2.6). The compared per mol activity shows the same trend, but with higher differences in current densities. Co_9 doubles the response of $Co_4P_2W_{18}$, and the two other catalysts exhibit a significantly lower activity. This suggests that nuclearity and/or total POM charge favors electrocatalytic activity in the Keggin-based series while Keggin derivatives are intrinsically more active than the corresponding Dawson-Wells, regardless of the countercation. This phenomenon can be relate to the steric hindrance imposed by larger POM ligands, slowing down the kinetics of the reaction. On the other hand, the higher activity of larger clusters should be related to a cooperative Co–O–Co interactions, since it cannot be due just to a higher number of active sites. On the contrary, the probability

of two or more Co centers being active in a single POM at the same time is computationally very high in energy.[38]

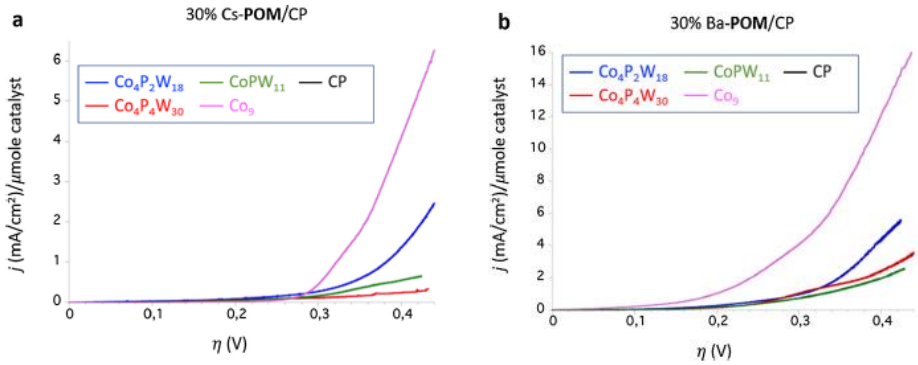

Figure 2.6. Linear sweep voltammetry in H_2SO_4 (1 M) solution with 30% Co-POM/CP blend working electrodes normalized by the total number of moles: (a) Cs-POM/CP blends; (b) Ba-POM/CP blends. Data collected with an RDE (surface area = 0.07 cm^2) at 500 rpm and with a 1 mV/s scan rate.

Looking for any indirect difference between all these materials, we studied the relative differences between active surface area in the double layer capacitance (Cdl). Although the actual surface area is difficult to assess just from electrochemical data, comparison of the Cdl values obtained for analogous electrodes, under the same conditions, should be proportional to the differences in surface active areas. From these data analyses we found that the Ba-POM electrodes show higher Cdl values when compared to the cesium counterparts (figure 2.7 – 2.10). This indicates that Ba salts have intrinsically higher active surface area towards water oxidation, which is reflected in the higher current densities reached.

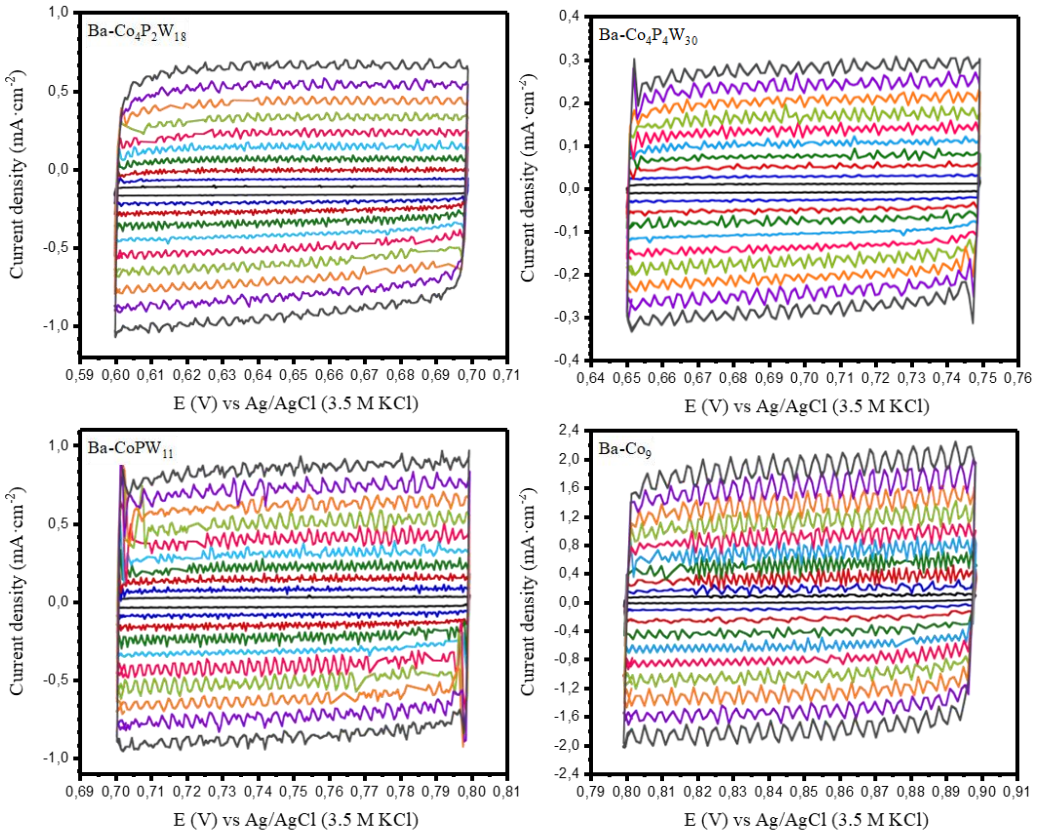

Figure 2.7. Double-layer capacitance (Cdl) measurements in 1 M H_2SO_4. (a) Cyclic voltammograms in the non-Faradaic region at the following scan rates: (black) 20, (dark-blue) 40, (red) 60, (dark-green) 80, (light-blue) 100, (pink) 120, (light-green) 140, (orange) 160, (purple) 180 and (grey) 200 mV/s.

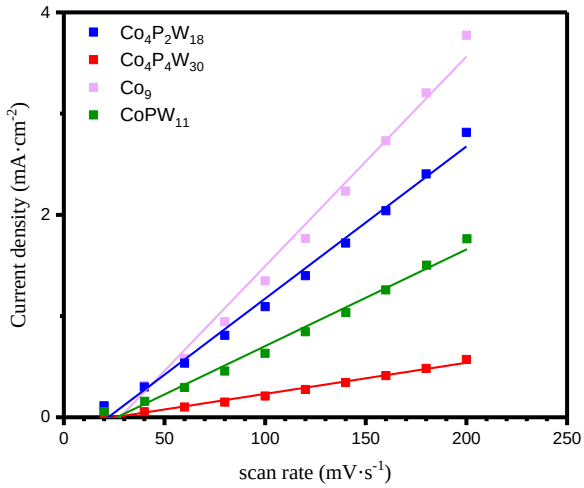

Figure 2.8. Plot of Dj (ja-jc) against the scan rate for Ba-POM, where the slope is twice the Cdl.

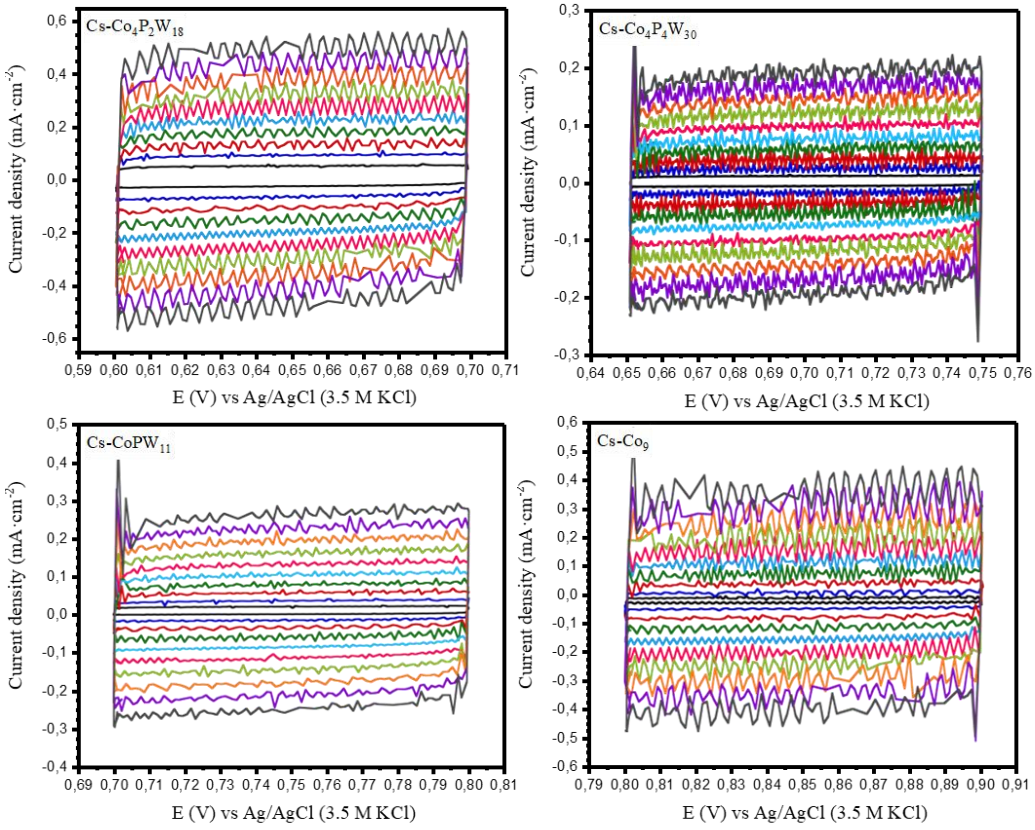

Figure 2.9. Double-layer capacitance (Cdl) measurements in 1 M H2SO4. (a) Cyclic voltammograms in the non-Faradaic region at the following scan rates: (black) 20, (dark-blue) 40, (red) 60, (dark-green) 80, (light-blue) 100, (pink) 120, (light-green) 140, (orange) 160, (purple) 180 and (grey) 200 mV/s.

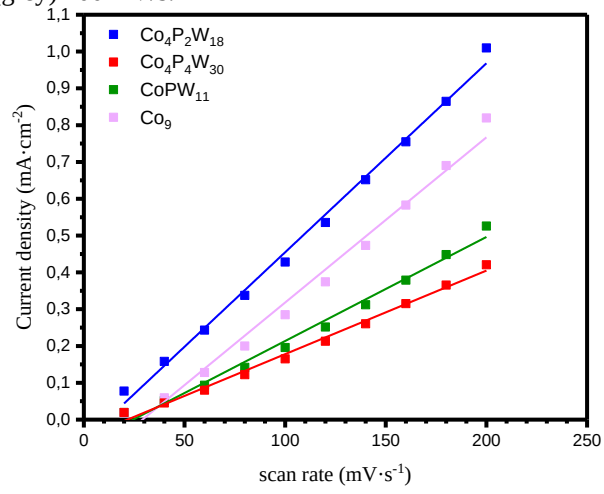

Figure 2.10. Plot of Dj (ja-jc) against the scan rate for Ba-POM, where the slope is twice the Cdl.

2.2.3. Post-catalytic characterization

In water oxidation electrocatalysis, it is very important to investigate the true genuine catalytic species, since operando evolution into other more active species (typically the corresponding metal oxides) may lead to incorrect conclusions. This is a very difficult task, since less than 1% impurity, hardly detectable, may be enough to account for the apparent visibility.[39] In acidic media this task is easier since most metal oxides are unstable or inactive.[40] In our previous studies, we could not find any traces of CoO_x after electrocatalytic performance, and given the very high activity, it can be concluded that just a small, undetectable impurity of CoO_x could not account for the total activity found. Here, the recovered catalysts after a 2 h chronopotentiometry was characterized by surface sensitive techniques using Raman spectroscopy and photoelectron spectroscopy (XPS).

On the other hand, the electrolyte solution also was analyzed by Inductively Coupled Plasma Mass Spectrometry (ICP-MS) (Table 2.1). It can observe some Cs leaching, accounting for less than 10% of the initial Cs content, which can be attributed to a partial protonation of the oxo-sites. All other elements were below the detection limits of the technique, except some traces of W (<1%). This suggests good chemical stability for all Co-POMS tested in these conditions.

Table 2.1. ICP-MS analyses of the liquid reaction media after 2 h electrocatalytic water oxidation at a constant current density of 1 mA/cm2 in H2SO4 (1 M) of stable compounds.

Mother liquor solution	Cs	Ba	P	Co	W
Cs-$Co_4P_2W_{18}$	2.3 ppm (5.8%)	-	≤1.0 ppm	≤1.0 ppm	≤1.0 ppm (1.4%)
Ba-$Co_4P_2W_{18}$	-	≤0.2 ppm	≤1.0 ppm	≤1.0 ppm	≤1.7 ppm (1.0%)
Cs-$Co_4P_4W_{30}$	2.8 ppm (6.7%)	-	≤1.0 ppm	≤1.0 ppm	≤1.0 ppm
Ba-$Co_4P_4W_{30}$	-	≤0.2 ppm	≤1.0 ppm	≤1.0 ppm	1.1 ppm (0.7%)
Cs-$CoPW_{11}$	4.2 ppm (13.5%)	-	≤1.0 ppm	≤1.0 ppm	≤1.0 ppm
Ba-$CoPW_{11}$	-	≤0.2 ppm	≤1.0 ppm	≤1.0 ppm	≤1.0 ppm
Cs-Co_9*	4.7 ppm (~30%)	-	≤1.0 ppm	≤1.0 ppm	≤1.0 ppm
Ba-Co_9*	-	≤0.2 ppm	≤1.0 ppm	≤1.0 ppm	≤1.0 ppm

* Data extracted from [34] Data in brackets refers to the percentage of metal lost.

The Raman data became crucial in this analysis. While the P-based catalysts did not show any significant differences between fresh or used materials show any difference in spectra (Figure 2.12), the recovered $CoSiW_{11}$ catalyst showed major changes in the Raman spectrum, with new bands appearing in the 400–800 cm^{-1} range, and original bands disappearing in the 800–1000 cm^{-1} range (Figure 2.11). This confirms decomposition process in this case and supports our preliminary conclusions from electrochemical data.

In order to confirm the preservation of the Co-POM structure after catalysis of P-based catalysts, IR spectra of recovered materials was collected. (Figure 2.13). Comparative analyses did not show any significant differences between pre- and post-electrolysis IR spectra.

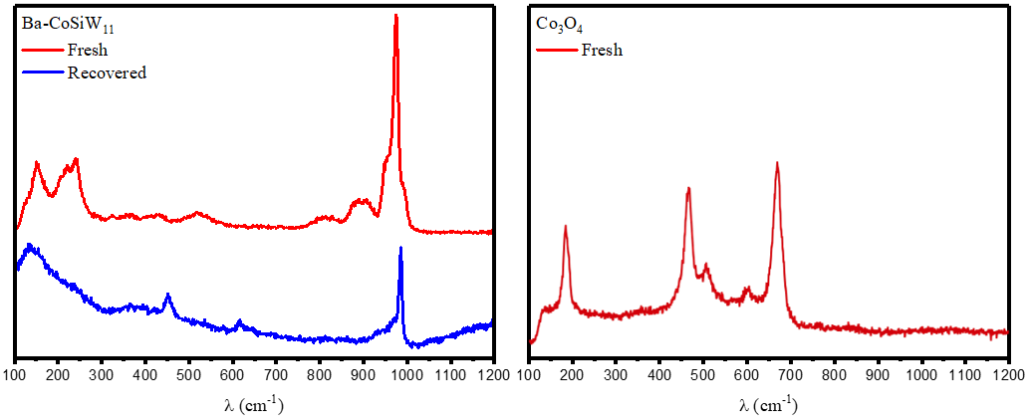

Figure 2.11. (left) Raman spectra for $CoSiW_{11}$ before and after 2 h electrocatalytic water oxidation at a constant current density of 1 $mA \cdot cm^{-2}$ in H_2SO_4 (1 M) (right) Raman spectra Co_3O_4

Despite the XPS spectra after electrolysis is extremely noisy due to the dilution in the carbon paste, the results are consistent with Raman data. As well, the XPS spectra confirms the stability observed with Raman. Regardless of their low reliability, a trend in the Co and O spectra show an increase in the absorption towards higher energy, suggesting higher oxidation states. The most important conclusion from XPS is again the absence of any signal related to CoOx after electrolysis (Figure 2.14 – 2.16).

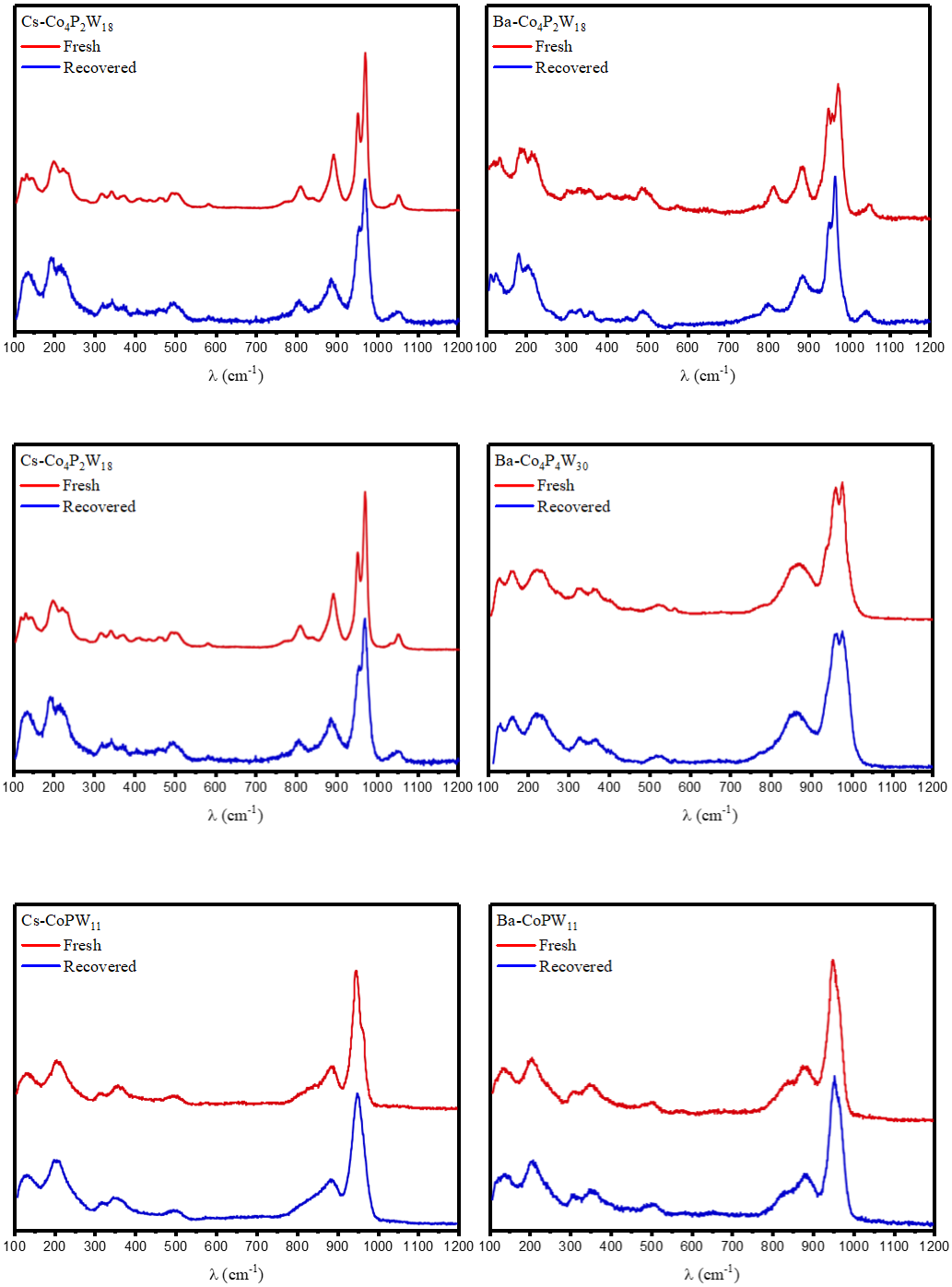

Figure 2.12. Raman spectra for $Co_4P_2W_{18}$, $Co_4P_4W_{30}$ and $CoPW_{11}$, before and after 2 h electrocatalytic water oxidation at a constant current density of 1 $mA \cdot cm^{-2}$ in H_2SO_4 (1 M).

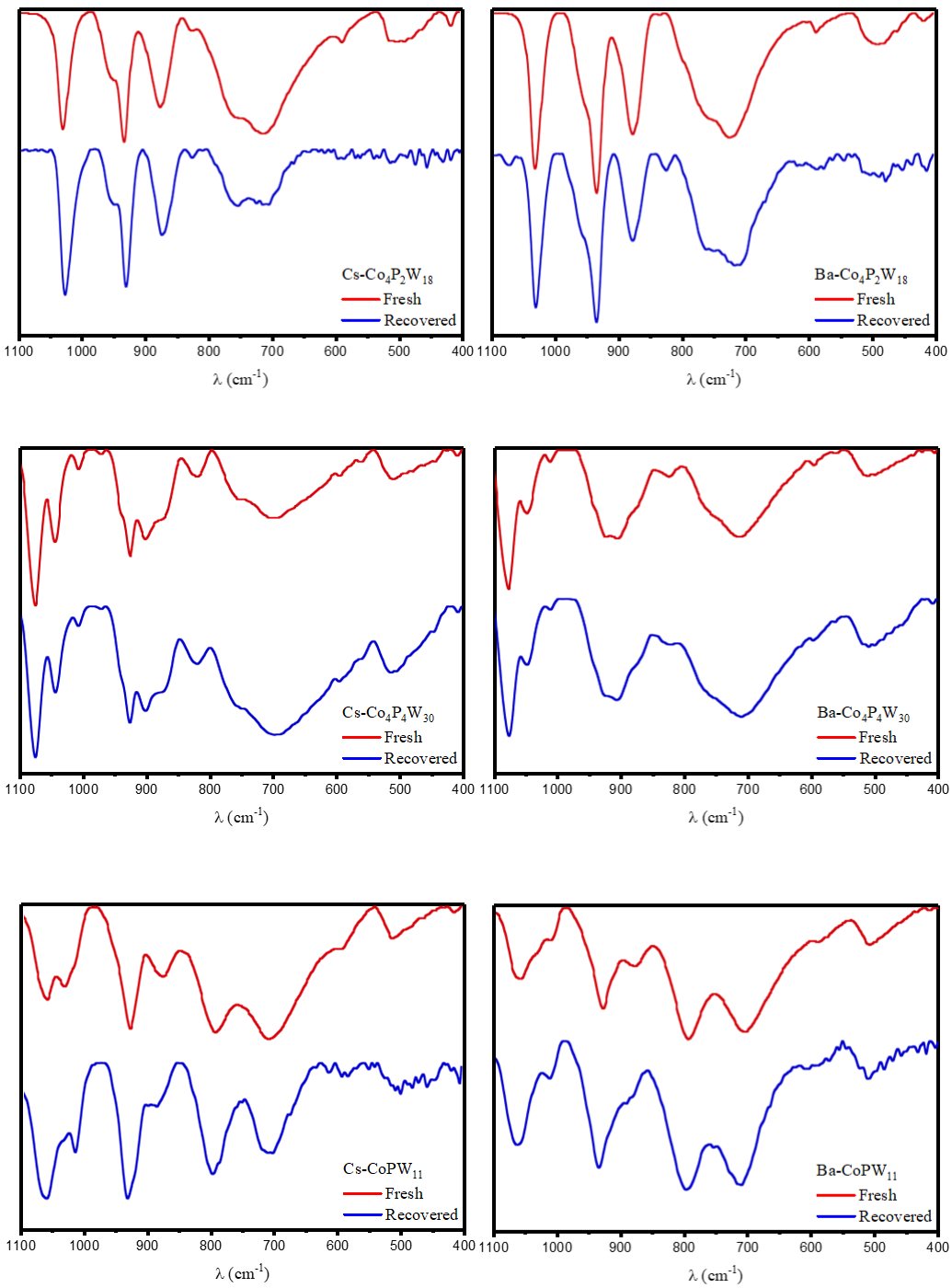

Figure 2.13. IR spectra for **$Co_4P_2W_{18}$, $Co_4P_4W_{30}$** and **$CoPW_{11}$**, before and after 2 h electrocatalytic water oxidation at a constant current density of 1 $mA \cdot cm^{-2}$ in H_2SO_4 (1 M).

The typical XPS peaks for CoOx appear at 930 eV and 925eV for Co (2s), 779.7 eV for Co (2p) and 529.8 for O (1s). The cesium-based compounds were checked using Co 2p and barium based compound were checked using of Co 2s due to the strong overlap between Ba 3d and Co 2p XPS absorptions.

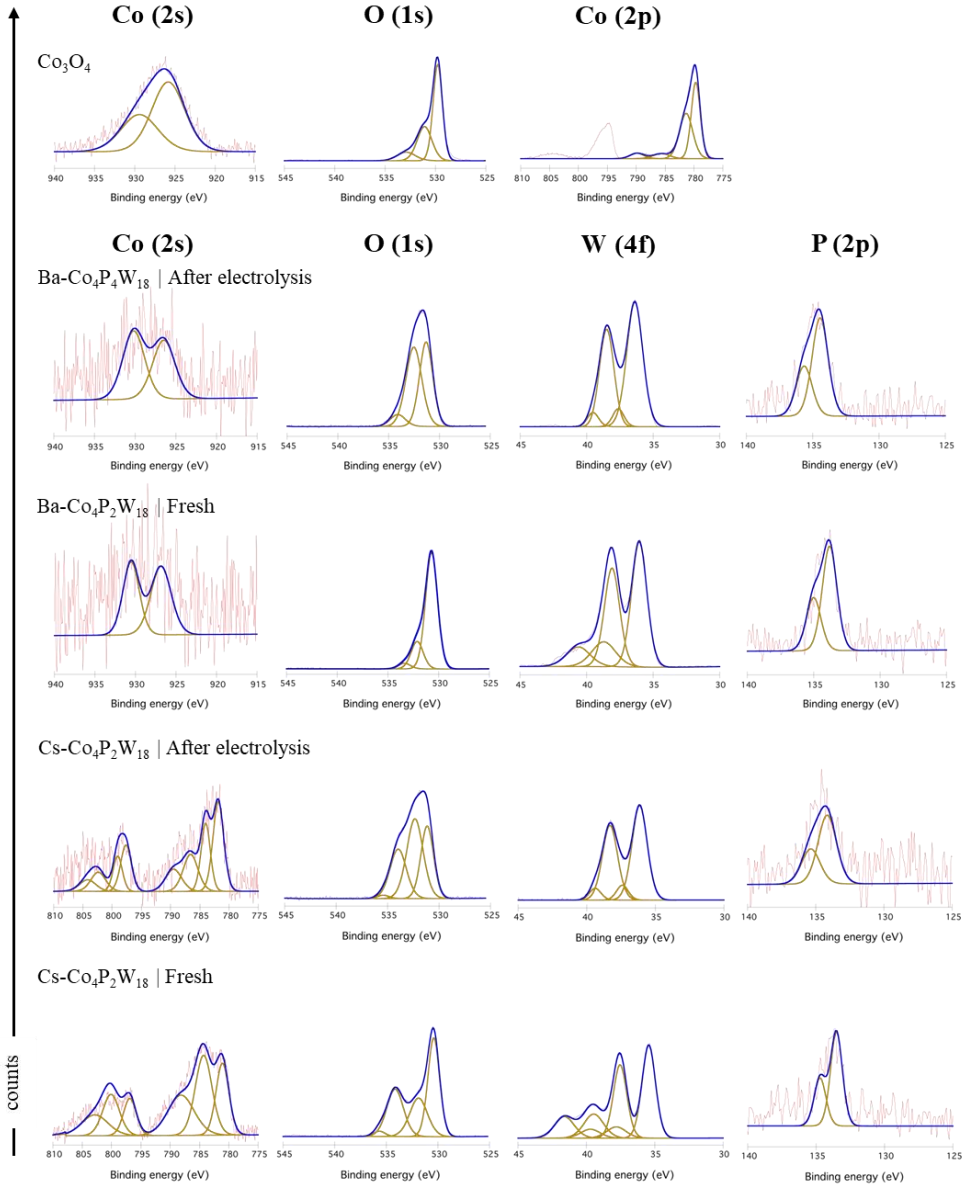

Figure 2.14. XPS data (Co, O, W and P edges) for $Co_4P_2W_{18}$ before and after 2 h electrocatalytic water oxidation at a constant current density of 1 $Ma \cdot cm^{-2}$ in H_2SO_4 (1 M). Co and O edges are compared with the corresponding XPS data for Co_3O_4.

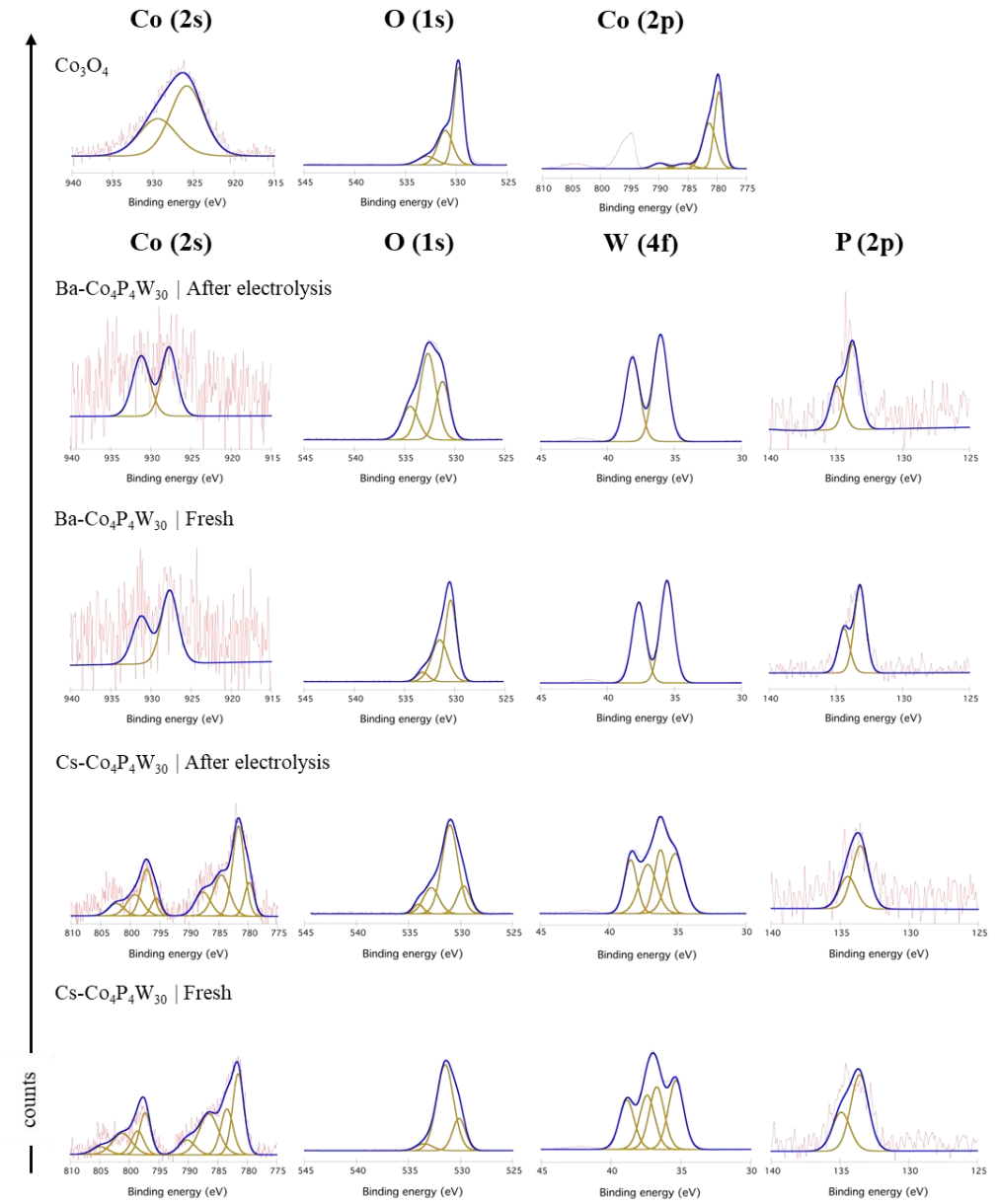

Figure 2.15. XPS data (Co, O, W and P edges) for **$Co_4P_4W_{30}$** before and after 2 h electrocatalytic water oxidation at a constant current density of 1 $Ma \cdot cm^{-2}$ in H_2SO_4 (1 M). Co and O edges are compared with the corresponding XPS data for Co_3O_4.

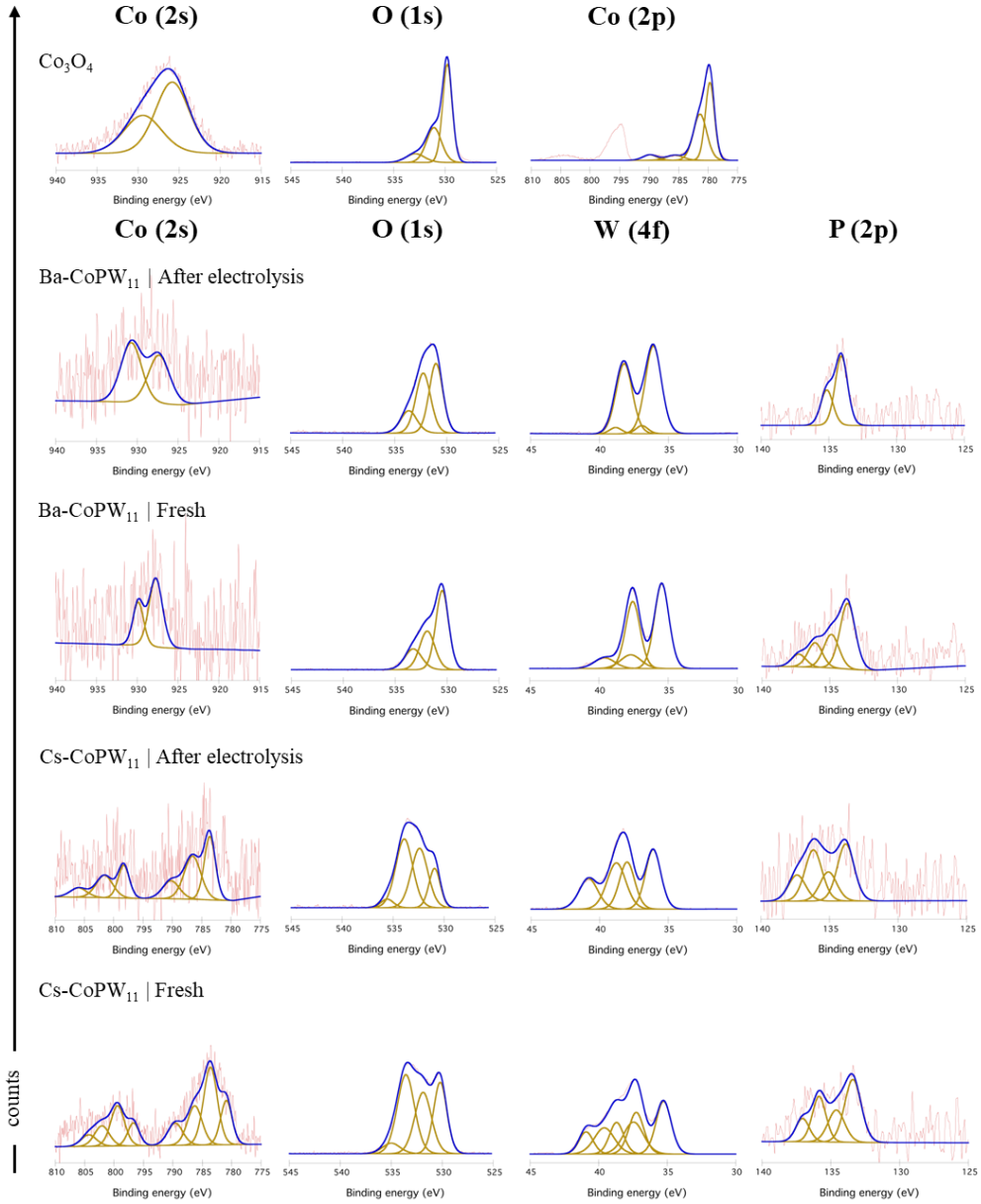

Figure 2.16. XPS data (Co, O, W and P edges) for **$CoPW_{11}$** before and after 2 h electrocatalytic water oxidation at a constant current density of 1 $mA \cdot cm^{-2}$ in H_2SO_4 (1 M). Co and O edges are compared with the corresponding XPS data for Co_3O_4.

2.3. Conclusions

In summary, we have explored the activity and stability of several Co-POMs toward water oxidation in acidic media when incorporated into carbon paste electrodes as Cs^{+} or Ba^{2+} salts. We found some common trends for WOC activity: i) only those POMs containing PV as heteroatom show good stability in working conditions; ii) the Keggin-derivatives exhibit faster performance than their Dawson-Wells counterparts; and iii) among them, catalytic activity is favoured by higher nuclearity of the cobalt cluster embedded by the POM ligands.

Still, we believe that the most relevant observation from all gathered data is the synergetic effect of a partially hydrophobic composite electrode (carbon paste) to stabilize Co-POM-based water oxidation catalysts in acidic media. The activity of these POM/CP composites is certainly remarkable in terms of current densities and catalyst stability. However, carbon paste is not a robust electrode for the long term since the high applied potentials generate electrostatic charges in the carbon paste resulting in mechanical expulsion of the electrode composited from their electrode pocket. In addition, for practical applications at high temperatures, high current densities and very long operation times, carbon is thermodynamically unstable and thus susceptible to corrosion. Therefore, for successful exploitation of Co-POMs and other abundant metal-based WOCs in acidic media, there is a clear need to find a robust and stable alternative electrode support, which mimics the conducting and hydrophobic features of carbon paste, but avoids the long-term stability problems.

2.4. Experimental section

2.4.1. Polyoxometalate synthesis

[$Co_4(H_2O)_2(PW_9O_{34})_2]^{10-}$ ($Co_4P_2W_{18}$)

Co4P2W18 was obtained as by-product in the synthesis of $[Co_9(H_2O)_6(OH)_3(HPO_4)_2(PW_9O_{34})_3]^{16-}$, as described in the literature.[41] $Na_2WO_4{\cdot}2H_2O$ (33.00g, 100.00 mmol) and Na_2HPO_4 (3.30 g, 22.00 mmol) were dissolved in 100 mL aqueous solution and acetic acid was added to adjust the pH of the solution at 7.1.

Afterwards, 30 mL of an aqueous solution containing $Co(OOC\text{-}CH_3)_2 \cdot 4H_2O$ (9.00 g, 35.00 mmol) were added and the violet suspension obtained was refluxed at 100 ºC for 2 hours. After reflux, the hot solution was filtered, and an excess of $K(OOC\text{-}CH_3)$ (2 g) was added. Then, the solution was filtered again, cooled down at room temperature and stored to allow crystallisation of $K_{10}[Co_4(H_2O)_2(PW_9O_{34})_2]$ and $K_{16}[Co_9(H_2O)_6(OH)_3(HPO_4)_2(PW_9O_{34})_3]$. The latter was extracted with cold water, while $K_{10}[Co_4(H_2O)_2(PW_9O_{34})_2]$ remained insoluble. $K_{10}[Co_4(H_2O)_2(PW_9O_{34})_2]$ was then dissolved with water at room temperature, precipitated by adding $K(OOC\text{-}CH_3)$ in excess, collected by filtration, and dried at 60 °C.

Water-insoluble cesium and barium salts of $Co_4P_2W_{18}$ were obtained by simple metathesis reaction, after addition of CsCl or $BaCl_2$ to an aqueous solution of $Co_4P_2W_{18}$ potassium salt.

The FT-IR data for the Cs and Ba salts are summarized in figure 2.18. POM composition was confirmed by EDX, water content was determined by thermogravimetric analysis (TGA) (Figure 2.17) and counter cation content was determined by elemental analysis.

$Cs_{8.3}K_{1.7}[Co_4(H_2O)_2(PW_9O_{34})_2] \cdot 14H_2O$ (Cs- $Co_4P_2W_{18}$) Mw=6152.33 g/mol. Elemental analyses, Calc. (%): Cs, 8.3; K, 1.7. Found (%): Cs, 9.6; K, 2.0. $Ba_5[Co_4(H_2O)_2(PW_9O_{34})_2] \cdot 38H_2O$ (Ba- $Co_4P_2W_{18}$) Mw=6101.42 g/mol. Elemental analysis calculated (%): Ba, 5.0. Found (%): Ba, 5.8.

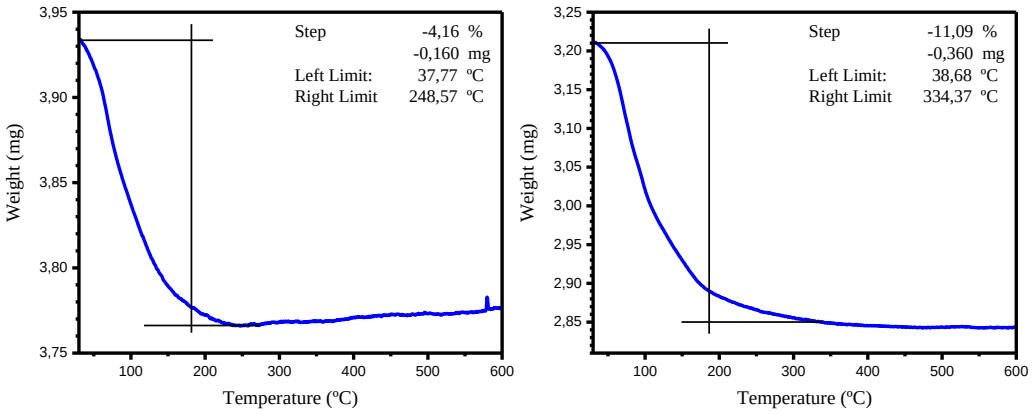

Figure 2.17. Thermogravimetric analysis for Cs- $Co_4P_2W_{18}$ (left) and Ba- $Co_4P_2W_{18}$ (right).

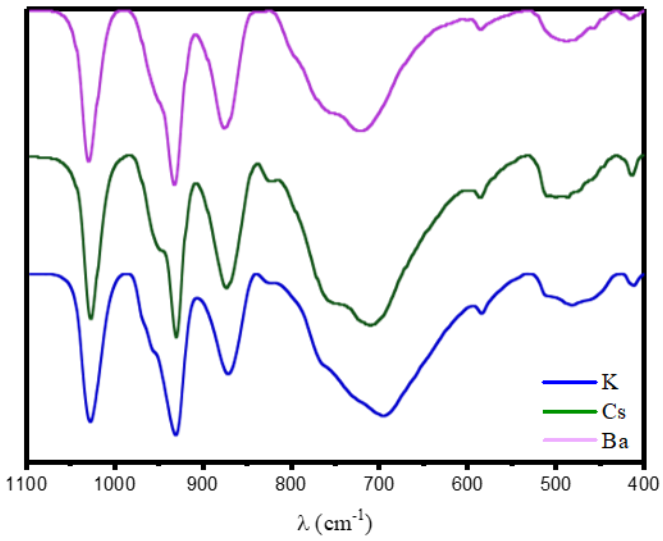

Figure 2.18. IR spectra of $Co_4P_2W_{18}$ with different countercations.

$[Co_4(H_2O)_2\ (SiW_9O_{34})]^{12-}$ ($Co_4Si_2W_{18}$)

$Co_4Si_2W_{18}$ was obtained following the procedure described in literature.[42] $Co(NO_3)_2{\cdot}6H_2O$ (0.32 g, 1.10 mmol) was dissolved in 15 mL of distilled water. Then a-$Na_{10}[SiW_9O_{34}]\cdot 15H_2O$ (1.00 g, 0.37 mmol) was added very slowly at room temperature over one hour. The resulting reddish solution was heated up at 75 °C during 30 minutes and then cooled down to room temperature. Afterwards, the suspension was centrifuged at 3500 rpm for 3 min and filtered through Celite. KNO_3 in excess was added to the transparent reddish solution, after 1 hour stirring the light-red product precipitated, which was isolated by filtration and dried at 60 °C.

The FT-IR data for the Cs and Ba salts are summarized in figure 2.20. POM composition was confirmed by EDX, water content was determined by thermogravimetric analysis (TGA) (Figure 2.19) and counter cation content was determined by elemental analysis. $Cs_{12}[Co_4(H_2O)_2\ (SiW_9O_{34})]\cdot 28H_2O$ (Cs- $Co_4Si_2W_{18}$) M_w=6823.88 g/mol. Elemental analyses, Calc. (%): Cs, 12.0 Found (%): Cs, 9.6; $Ba_{5.4}K_{1.2}[Co_4(H_2O)_2\ (SiW_9O_{34})]$ ·31H2O (Ba- $Co_4Si_2W_{18}$) M_w=6071.35 g/mol. Elemental analysis calculated (%): Ba, 5.4; K, 1.2. Found (%): Ba, 6.2; K, 1.4.

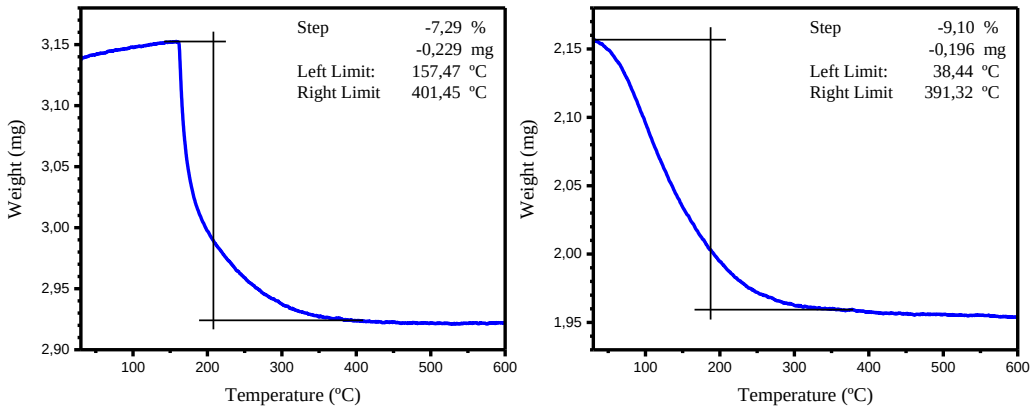

Figure 2.19. Thermogravimetric analysis for Cs-$Co_4Si_2W_{18}$ (left) and Ba-$Co_4Si_2W_{18}$ (right).

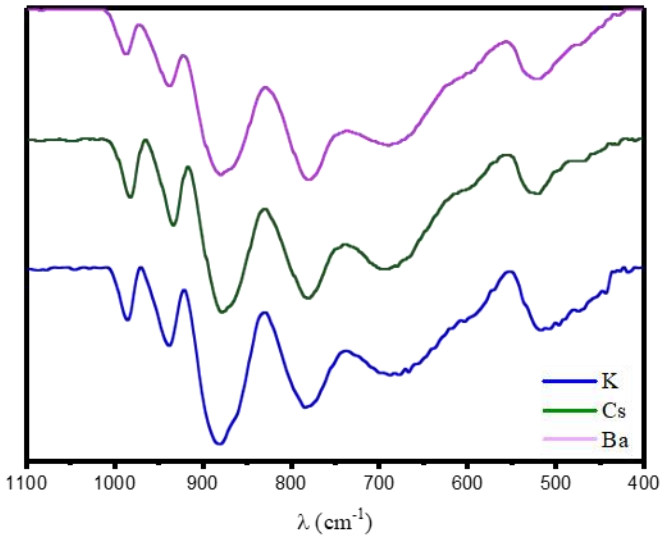

Figure 2.20. IR spectra of $Co_4Si_2W_{18}$ with different countercations.

$[Co_4(H_2O)_2(P_2W_{15}O_{56})_2]^{16-}$ ($Co_4P_4W_{30}$)

$Co_4P_4W_{30}$ was synthesised according to the procedure reported in literature.[43] $Co(NO_3)_2{\cdot}6H_2O$ (0.31 g, 1.07 mmol) was dissolved in 21 mL of a 1 M NaCl aqueous solution. Then, a-$Na_{12}P_2W_{15}O_{56}$ (2.00 g, 0.50 mmol) was added and the suspension was heated up to 50 °C to assure a complete dissolution of all compounds. The initial light-red solution turned to red-brown with green reflections and it was left at 5 °C overnight. A crystalline brown-green solid appeared after one day, which was collected by filtration. The resulting brown-green solid was dried at 60 °C in the oven.

The FT-IR data for the Cs and Ba salts are summarized in figure 2.22. POM composition was confirmed by EDX, water content was determined by thermogravimetric analysis (TGA) (Figure 2.20) and counter cation content was determined by elemental analysis. $Cs_{12}Na_4[Co_4(H_2O)_2(P_2W_{15}O_{56})_2]$ ·17H2O ($Co_4P_4W_{30}$) Mw=9695.62 g/mol. Elemental analyses, Calc. (%): Cs, 12.0; Na, 4.0. Found (%): Cs, 9.4; Na, 3.1. $Ba_{5.4}Na_{5.2}[Co_4(H_2O)_2(P_2W_{15}O_{56})_2]$ ·$30H_2O$ ($Co_4P_4W_{30}$) Mw=9103.80 g/mol. Elemental analysis calculated (%): Ba, 5.4; Na, 5.2. Found (%): Ba, 4.8; Na, 4.6.

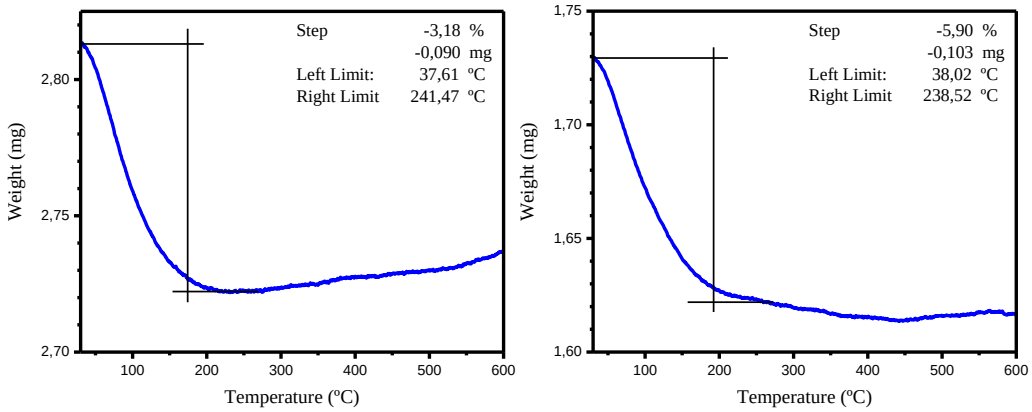

Figure 2.21. Thermogravimetric analysis for Cs- $Co_4P_4W_{30}$ (left) and Ba- $Co_4P_4W_{30}$ (right).

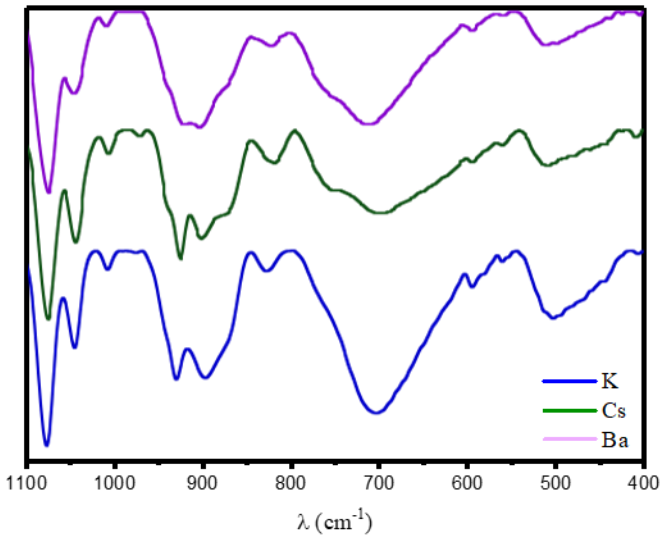

Figure 2.22. IR spectra of $Co_4P_4W_{30}$ with different countercations.

$[Co(H_2O)(PW_{11}O_{39})]^{5-}$ ($CoPW_{11}$)

$CoPW_{11}$ was obtained according to the procedure reported in literature.[44] $Na_8HPW_9O_{34}$ (8.69 g, 3.60 mmol)[3] was dissolved in 100 mL distilled water and 1 mL glacial acetic acid was added. Then, $Co(OOCCH_3)_2 \cdot 4H_2O$ (1.79 g, 6.96 mmol) was added and pH was adjusted to 5 by adding some drops of glacial acetic acid. The solution was kept under reflux at 100°C during 2 hour and then filtered while still hot. After cooling down the solution to room temperature, K(OOC-CH_3) was added in excess to precipitate the desired purple solid. The product was filtered and dried at 60°C.

The The FT-IR data for the Cs and Ba salts are summarized in figure 2.24. POM composition was confirmed by EDX, water content was determined by thermogravimetric analysis (TGA) (Figure 2.23) and counter cation content was determined by elemental analysis.

$Cs_5[Co(H_2O)(PW_{11}O_{39})] \cdot 13H_2O$ (Cs-$CoPW_{11}$) M_w=3652.67 g/mol. Elemental analyses, Calc. (%): Cs, 5.0. Found (%): Cs, 4.4. $Ba_{2.1}K_{0.8}[Co(H_2O)(PW_{11}O_{39})] \cdot 19H_2O$ (Ba-$CoPW_{11}$) M_w=3415.75 g/mol. Elemental analysis calculated (%): Ba, 2.1; K, 0.8. Found (%): Ba, 2.2; K, 0.8.

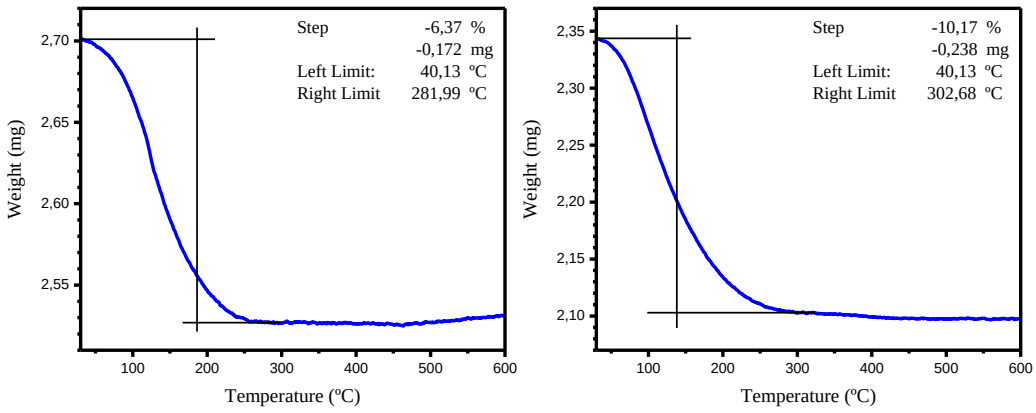

Figure 2.23. Thermogravimetric analysis for Cs-$CoPW_{11}$ (left) and Ba-$CoPW_{11}$ (right).

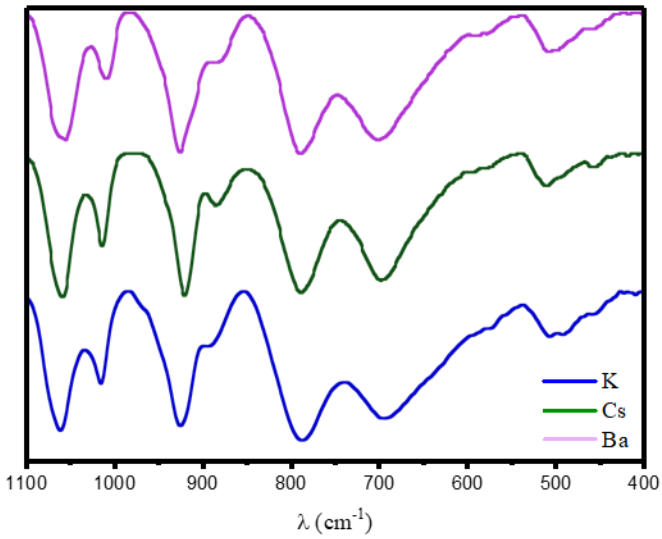

Figure 2.24. IR spectra of $CoPW_{11}$ with different countercations.

$[Co(H_2O)(SiW_{11}O_{39})]^{6-}$ ($CoSiW_{11}$)

$CoSiW_{11}$ was obtained according to the procedure reported in literature.[45] $K_8[\alpha\text{-}SiW_{11}O_{39}]$ (1.61 g, 0.50 mmol) was added to a 5 mL aqueous solution of $Co(NO_3)_2 \cdot 6H_2O$ (0.15 g, 0.52 mmol). The solution was heated up until boiling and kept under stirring at this temperature for some minutes. Then, the hot solution was filtered and 1 mL KCl 2.7 M was added. The solution was kept at 5°C and red crystalline needles of the product appeared after a day. The crystalline product was filtered and dried at 60°C. The The FT-IR data for the Cs and Ba salts are summarized in figure 2.26. POM composition was confirmed by EDX, water content was determined by thermogravimetric analysis (TGA) (Figure 2.25) and counter cation content was determined by elemental analysis.

$Cs_6[Co(H_2O)(SiW_{11}O_{39})] \cdot 5H_2O$ (Cs-$CoSiW_{11}$) M_w=3638.68 g/mol. Elemental analyses, Calc. (%): Cs, 6.0. Found (%): Cs, 6.4. $Ba_3[Co(H_2O)(SiW_{11}O_{39})] \cdot 13H_2O$ (Ba-$CoSiW_{11}$) Mw=3397.23 g/mol. Elemental analysis calculated (%): Ba, 3.0. Found (%): Ba, 3.2.

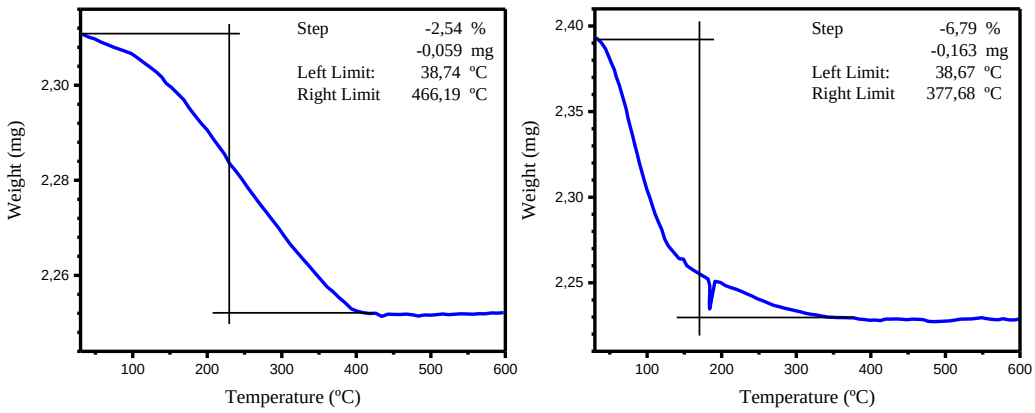

Figure 2.25. Thermogravimetric analysis for Cs-$CoSiW_{11}$ (left) and Ba-$CoSiW_{11}$ (right).

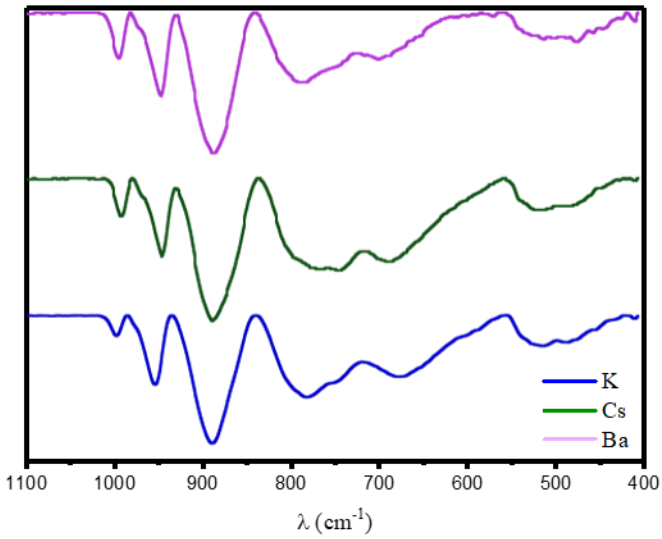

Figure 2.26. IR spectra of $CoSiW_{11}$ with different countercations.

$[Co(H_2O)(CoW_{11}O_{39})]^{7-}$ ($CoCoW_{11}$)

$CoCoW_{11}$ was obtained according to the procedure reported in literature.[46] $Na_2WO_4 \cdot 2H_2O$ (19.80 g, 60.00 mmol) was dissolved in 40 mL distilled water, 4 mL glacial acetic acid were added (pH: 6.5~7.5) and the solution was heated up to 70°C. Then, a 13 mL aqueous solution containing $Co(OOC\text{-}CH_3)_2 \cdot 4H_2O$ (2.50 g, 0.64 mmol) was slowly added to the initial solution. Afterwards, the resulting solution was kept under reflux at 100°C during 30 minutes and then filtered while still hot. The emerald solution was heated up again to 80°C and $K_2S_2O_8$ (7.00 g, 25.90 mmol) was slowly added and evolution of gas was observed. When addition was complete, the solution was heated to boiling and kept at this temperature during 5 minutes. During the heating process a colour change from emerald to dark brown was observed. The solution was filtered while still hot and heated up again to boiling when a 25 mL of hot saturated KNO_3 solution was added. The solution was kept at 5°C during 1 hour with the appearance of a brown precipitate. The brown solid was collected by filtration and dissolved in ~40 mL distilled water after heating at 90°C. The hot mixture was filtrated and the solution was cooled down to room temperature. The clear brown solution was kept at 5°C overnight and cubic dark-brown crystals appeared, which were collected by filtration and dried at 60°C. The FT-IR and XRD data for the Cs and Ba salts are reported in the Supporting Information (Fig. S6 and S12). POM composition was confirmed by EDX, water content was determined by thermogravimetric analysis (TGA) (Fig. S13) and counter cation content was determined by elemental analysis.

$Cs_7[Co(H_2O)(CoW_{11}O_{39})] \cdot 10H_2O$ ($Cs\text{-}CoCoW_{11}$) M_w=3892.40 g/mol. Elemental analyses, Calc. (%): Cs, 7.0. Found (%): Cs, 7.0. $Ba_{2.7}K_{1.6}[Co(H_2O)(CoW_{11}O_{39})] \cdot 12H_2O$ ($Ba\text{-}CoCoW_{11}$) M_w=3431.37 g/mol.

Elemental analysis calculated (%): Ba, 2.7; K, 1.6. Found (%): Ba, 3.2; K, 1.8.

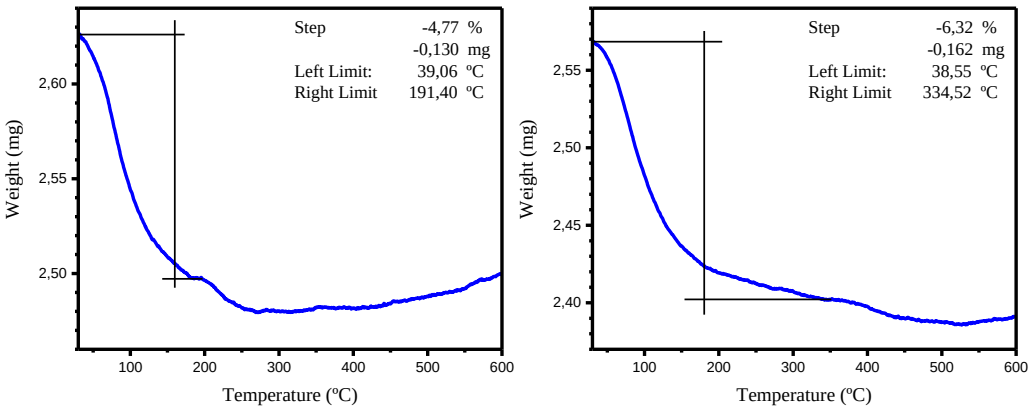

Figure 2.27. Thermogravimetric analysis for Cs-$CoCoW_{11}$ (left) and Ba-$CoCoW_{11}$ (right).

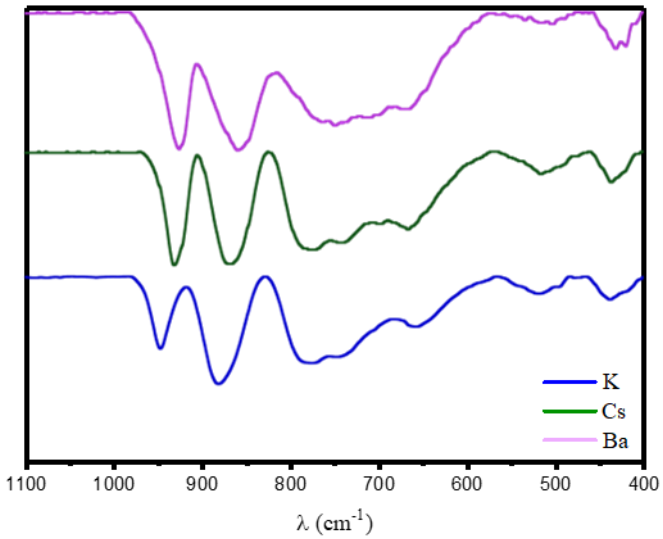

Figure 2.28. IR spectra of $CoCoW_{11}$ with different countercations.

2.4.2. Characterization methods

Thermogravimetric analysis (TGA) was performed under N_2 flow with powder samples using a TGA/SDTA851 Mettler Toledo with a MT1 microbalance. The experiment were carried out using about 2 mg of sample, as powder, in Al-crucible of 40 lL and scan range from 30 to 600 ºC with rate of 10 ºC·min^{-1}. Powder X-ray diffraction data were collected with a Bruker D8 Advance Series equipped with a VANTEC-1 PSD detector. Data were collected in the 10-70º 2Θ diffraction range with 0.008º steps with a total experiment of 60 min. IR spectra were collected with a FTIR Bruker spectrometer model Alpha equipped with an ATR accessory in the 400–4000 cm^{-1} range, averaging 32 scans. Raman measurements were acquired using a Renishaw inVia Reflex Raman confocal microscope (Gloucester- Shire, UK), equipped with a diode laser emitting at 785 nm at a nominal power of 300 mW, and a Peltier-cooled CCD detector (-70 ºC) coupled to a Leica DM-2500 microscope. Calibration was carried out daily by recording the Raman spectrum of an internal Si standard. Rayleigh scattered light was appropriately rejected by using edge-type filters. Laser power was used at nominal 1% to avoid sample damage. Spectra were record ed in the 100–1800 cm^{-1} range with the accumulation of at least 3 scans with a 30 s scan time each one. Cation content was determined by energy-dispersive X-ray spectroscopy (EDX), which was collected with a JEOL- JMS6400 environmental scanning electron microscope equipped with an Oxford Instruments.

X-ray elemental analyzer. X-ray photoelectron spectroscopy (XPS, K-ALPHA, Thermo Scientific, SSTTI at University of Alicante) was used to analyze sample surfaces. All spectra were collected using Al-Ka radiation (1486.6 eV), monochromatized by a twin crystal monochromator, yielding a focused X-ray spot with a diameter of 400 μm, at 3 mA·12 kV. The alpha hemispherical analyzer was operated in the constant energy mode with survey scan pass energies of 200 eV to measure the whole energy band and 50 eV in a narrow scan to selectively measure the particular elements. Charge compensation was achieved with the system flood gun that provides low energy electrons and low energy argon ions from a single source. Sample powder was adhered onto a carbon tape using Alstubs as a support and cleaned with airflow to remove

unattached particles. Measurements were performed under low-vacuum conditions with a Large-Field Detector at 20 kV using a probe current of 17 pA.

Elemental analyses of solid samples were carried out with an Agilent 725-ES inductively coupled plasma optical emission spectrometer (ICP-OES) at the University of Valladolid taking Ba, Cs, K and Na 1000 mg/mL, in 2–5% HNO_3 standards. One gram of solid sample was digested with acidic solution (1 mL distilled water, 3 mL of concentrated HNO_3, 1 mL of concentrated HCl and 2 mL of concentrated HF). This method was more reliable than alternative solution in basic media. Elemental analysis of metal leaching in solution was carried out with an Inductively Coupled Plasma Quadrupolar Mass Spectrometer (ICP-MS) (Thermo, iCAP Qc, Xt interphase and PFA micronebulizer) at the University of País Vasco in Bilbao taking Ba (455.403), Cs (697.327), W (207.912), Co (238.892), P (213.618) and Si (250.690) standards.

2.4.3. Electrochemical details

All electrochemical experiments were performed under ambient conditions with a Biologic SP-150 potentiostat. All experiments were performed with a threeelectrode configuration using H_2SO_4 (1 M) as electrolyte solution, employing a platinum mesh counter electrode, a reference electrode and a carbon paste working electrode (surface area = 0.07 cm^2). For the linear sweep voltammetry experiments (LSV) Saturated Calomel Electrode (SCE) was used as reference electrode, while Ag/AgCl (3.5 M KCl) was chosen for the bulk electrolysis tests and double layer capacitance measurements. Linear sweep voltammetry was performed with an ALS RRDE-3A setup, using a Carbon Paste Rotating Disk Electrode (surface area = 0.07 cm^2) at 500 rpm. All LSV experiments were carried out with a 1 mV/s scan rate. Successive cycles were measured until consistent repeatability for those POMs where additional redox events do not appear (typically > 10 cycles). In addition, all experiments were performed three times showing good reproducibility (only one of the experiments is reported). Two hours bulk electrolysis experiments at a constant current density (1 $mA \cdot cm^{-2}$) were performed in a H-cell with a porous frit in the middle to avoid gas recombination. The electrode was protected with a porous glass frit on the tip to avoid expulsion of the catalyst mixture from the electrode pocket during the measurement. Exact pH was measured for each experiment using an 877 Titrino Plus pH-probe (Metrohm), calibrated weekly.

The pH value was used to calculate the thermodynamic water oxidation potential ($E^o_{H_2O|O_2}$) from the Nerst equation:

$$E^o_{H_2O|O_2} = 1.229 - 0.059pH \; vs \; NHE \; at \; 25^oC$$

The overpotential (g) was calculated by subtracting the thermodynamic water oxidation potential to the applied potential (Eapp vs NHE):

$$\eta = E_{app} - H2O_{H_2O|O_2}$$

All the potentials were converted to the NHE reference scale using $E_{NHE} = E_{Ag|AgCl} + 0.205\ (V)$ or $E_{NHE} = E_{SCE} + 0.241\ (V)$, respectively. All current densities were calculated based on the geometrical surface area of the electrodes.

2.4.3.1. Electrode preparation

Electrode preparation Ba[Co-POM] and Cs[Co-POM] salts were obtained by metathesis by addition of an excess of CsCl or $BaCl_2$ to a 5 mM solution of the corresponding K_xNa_y[Co-POM] salts, which immediately yields the desired precipitate. To prepare the electrodes, these salts were mixed with the carbon paste in a mortar in the desired weight ratio. This modified carbon paste mixture was used to fill the corresponding pocket in a carbon paste electrode.

2.4.3.2. Catalyst recovery

After electrochemical experiments, the Co-POM/CP blend (40 mg) was suspended in acetone (30 mL) and sonicated for five minutes. The supernatant liquid (containing most of the carbon paste) was decanted to retain the Co-POM catalyst in the beaker. This procedure was repeated 10 times to get a clean catalyst sample, ready for post-catalytic characterization.

2.5. References

[1] D. G. Nocera, *Acc. Chem. Res.* **2012**, *45*, 767.

[2] A. Harriman, *Philos. Trans. R. Soc. A Math. Phys. Eng. Sci.* **2013**, *371*, 20110415.

[3] E. H. Yu, X. Wang, U. Krewer, L. Li, K. Scott, *Energy Environ. Sci.* **2012**, *5*, 5668.

[4] A. Harriman, I. J. Pickering, J. M. Thomas, P. A. Christensen, *J. Chem. Soc.{,} Faraday Trans. 1* **1988**, *84*, 2795.

[5] D. A. Corrigan, S. P. Maheswari, *Electrochem. Soc. Ext. Abstr.* **1985**, *85–1*, 934.

[6] L. Trotochaud, J. K. Ranney, K. N. Williams, S. W. Boettcher, *J. Am. Chem. Soc.* **2012**, *134*, 17253.

[7] R. D. L. Smith, M. S. Prévot, R. D. Fagan, Z. Zhang, P. A. Sedach, M. K. J. Siu, S. Trudel, C. P. Berlinguette, *Science (80-.).* **2013**, *340*, 60 LP.

[8] J. B. Gerken, S. E. Shaner, R. C. Massé, N. J. Porubsky, S. S. Stahl, *Energy Environ. Sci.* **2014**, *7*, 2376.

[9] H. Zhou, F. Yu, J. Sun, R. He, S. Chen, C.-W. Chu, Z. Ren, *Proc. Natl. Acad. Sci.* **2017**, *114*, 5607 LP.

[10] B. M. Hunter, H. B. Gray, A. M. Müller, *Chem. Rev.* **2016**, *116*, 14120.

[11] M. Gong, H. Dai, *Nano Res.* **2014**, *8*, 23.

[12] F. Lu, M. Zhou, Y. Zhou, X. Zeng, *Small* **2017**, *13*, 1701931.

[13] M. Görlin, J. Ferreira de Araújo, H. Schmies, D. Bernsmeier, S. Dresp, M. Gliech, Z. Jusys, P. Chernev, R. Kraehnert, H. Dau, P. Strasser, *J. Am. Chem. Soc.* **2017**, *139*, 2070.

[14] J. B. Gerken, J. Gregory McAlpin, J. Y. C. Chen, M. L. Rigsby, W. H. Casey, R.

David Britt, S. S. Stahl, *J. Am. Chem. Soc.* **2011**, *133*, 14431.

[15] M. W. Kanan, D. G. Nocera, *Science (80-.).* **2008**, *321*, 1072 LP.

[16] Y. Surendranath, D. A. Lutterman, Y. Liu, D. G. Nocera, *J. Am. Chem. Soc.* **2012**, *134*, 6326.

[17] M. Huynh, D. Kwabena Bediako, D. G. Nocera, *J. Am. Chem. Soc.* **2014**, *136*, 6002.

[18] J. S. Mondschein, J. F. Callejas, C. G. Read, J. Y. C. Chen, C. F. Holder, C. K. Badding, R. E. Schaak, *Chem. Mater.* **2017**, *29*, 950.

[19] L. G. Bloor, P. I. Molina, M. D. Symes, L. Cronin, *J. Am. Chem. Soc.* **2014**, *136*, 3304.

[20] R. Frydendal, E. A. Paoli, I. Chorkendorff, J. Rossmeisl, I. E. L. Stephens, *Adv. Energy Mater.* **2015**, *5*.

[21] M. Chatti, J. L. Gardiner, M. Fournier, B. Johannessen, T. Williams, T. R. Gengenbach, N. Pai, C. Nguyen, D. R. MacFarlane, R. K. Hocking, A. N. Simonov, *Nat. Catal.* **2019**, *2*, 457.

[22] A. Sartorel, M. Carraro, G. Scorrano, R. De Zorzi, S. Geremia, N. D. McDaniel, S. Bernhard, M. Bonchio, *J. Am. Chem. Soc.* **2008**, *130*, 5006.

[23] M. Quintana, A. M. López, S. Rapino, F. M. Toma, M. Iurlo, M. Carraro, A. Sartorel, C. Maccato, X. Ke, C. Bittencourt, T. Da Ros, G. Van Tendeloo, M. Marcaccio, F. Paolucci, M. Prato, M. Bonchio, *ACS Nano* **2013**, *7*, 811.

[24] Q. Yin, J. M. Tan, C. Besson, Y. V Geletii, D. G. Musaev, A. E. Kuznetsov, Z. Luo, K. I. Hardcastle, C. L. Hill, *Science (80-.).* **2010**, *328*, 342 LP.

[25] H. Lv, J. Song, Y. V. Geletii, J. W. Vickers, J. M. Sumliner, D. G. Musaev, P. Kögerler, P. F. Zhuk, J. Bacsa, G. Zhu, C. L. Hill, *J. Am. Chem. Soc.* **2014**, *136*, 9268.

[26] S. Goberna-Ferrón, L. Vigara, J. Soriano-López, J. R. Galán-Mascarós, *Inorg. Chem.* **2012**, *51*, 11707.

[27] H. Lv, Y. V Geletii, C. Zhao, J. W. Vickers, G. Zhu, Z. Luo, J. Song, T. Lian, D. G. Musaev, C. L. Hill, *Chem. Soc. Rev.* **2012**, *41*, 7572.

[28] J. W. Vickers, H. Lv, J. M. Sumliner, G. Zhu, Z. Luo, D. G. Musaev, Y. V. Geletii, C. L. Hill, *J. Am. Chem. Soc.* **2013**, *135*, 14110.

[29] J. J. Stracke, R. G. Finke, *ACS Catal.* **2013**, *4*, 79.

[30] M. Natali, I. Bazzan, S. Goberna-Ferrón, R. Al-Oweini, M. Ibrahim, B. S. Bassil, H. Dau, F. Scandola, J. R. Galán-Mascarós, U. Kortz, A. Sartorel, I. Zaharieva, M. Bonchio, *Green Chem.* **2017**, *19*, 2416.

[31] S. Goberna-Ferrón, J. Soriano-López, J. R. Galán-Mascarós, M. Nyman, *Eur. J. Inorg. Chem.* **2015**, *2015*, 2833.

[32] J. Wu, L. Liao, W. Yan, Y. Xue, Y. Sun, X. Yan, Y. Chen, Y. Xie, *ChemSusChem* **2012**, *5*, 1207.

[33] J. Soriano-López, S. Goberna-Ferrón, L. Vigara, J. J. Carbó, J. M. Poblet, J. R. Galán-Mascarós, *Inorg. Chem.* **2013**, *52*, 4753.

[34] M. Blasco-Ahicart, J. Soriano-López, J. J. Carbó, J. M. Poblet, J. R. Galan-Mascaros, *Nat. Chem.* **2017**, *10*, 24.

[35] X. López, J. A. Fernández, J. M. Poblet, *Dalt. Trans.* **2006**, 1162.

[36] X. López, J. J. Carbó, C. Bo, J. M. Poblet, *Chem. Soc. Rev.* **2012**, *41*, 7537.

[37] A. Haider, B. S. Bassil, J. Soriano-López, H. M. Qasim, C. S. de Pipaón, M. Ibrahim, D. Dutta, Y.-S. Koo, J. J. Carbó, J. M. Poblet, J. R. Galán-Mascarós, U. Kortz, *Inorg. Chem.* **2019**, *58*, 11308.

[38] J. Soriano-López, D. G. Musaev, C. L. Hill, J. R. Galán-Mascarós, J. J. Carbó, J. M. Poblet, *J. Catal.* **2017**, *350*, 56.

[39] S. J. Folkman, J. Soriano-Lopez, J. Ramón Galán-Mascarós, R. G. Finke, *J. Am. Chem. Soc.* **2018**, *140*, 12040.

[40] C. C. L. McCrory, S. Jung, I. M. Ferrer, S. M. Chatman, J. C. Peters, T. F. Jaramillo, *J. Am. Chem. Soc.* **2015**, *137*, 4347.

[41] J. R. Galán-Mascarós, C. J. Gómez-Garcia, J. J. Borrás-Almenar, E. Coronado, *Adv. Mater.* **1994**, *6*, 221.

[42] P.-E. Car, M. Guttentag, K. K. Baldridge, R. Alberto, G. R. Patzke, *Green Chem.* **2012**, *14*, 1680.

[43] R. G. Finke, M. W. Droege, P. J. Domaille, *Inorg. Chem.* **2002**, *26*, 3886.

[44] J. R. Galán-Mascarós, C. Giménez-Saiz, S. Triki, C. J. Gómez-García, E. Coronado, L. Ouahab, *Angew. Chemie Int. Ed. English* **1995**, *34*, 1460.

[45] A. Müller, L. Dloczik, E. Diemann, M. T. Pope, *Inorganica Chim. Acta* **1997**, *257*, 231.

[46] F. Song, Y. Ding, B. Ma, C. Wang, Q. Wang, X. Du, S. Fu, J. Song, *Energy Environ. Sci.* **2013**, *6*, 1170.

Chapter 3

Understanding POMs as water oxidation catalysts through Iron vs. Cobalt reactivity

3.1. Introduction

The development of sustainable, carbon-free energy concepts has become of paramount importance to meet the growing global energy demands while diminishing anthropogenic CO_2 emissions.[1,2] Solar energy is considered the most powerful source of clean and renewable energy.[3–5] However, due to its intermittency, solar energy needs to be harvested and stored, preferably in the form of chemical bonds such as H_2, to be supplied on demand. In the hydrogen economy, water is used as a clean fuel owing to its ubiquity, providing the required reducing equivalents to produce H_2 through the water splitting reaction, thus mimicking natural photosynthesis.[6,7] Notwithstanding, the water oxidation half reaction to produce O_2 is both thermodynamically and kinetically highly energy demanding, typically illustrated by high overpotentials (η) and sluggish kinetics during the O–O bond formation.[8–10] Hence, the water oxidation half-reaction is considered a bottleneck within the scheme, hampering the development and deployment of this technology.

The use of water oxidation catalysts (WOCs) is imperative in order to alleviate the high-energy demands of the reaction. In this regard, noble metal-based WOCs have shown promising catalytic capabilities.[11,12] However, their implementation in large-scale applications is limited due to their scarcity and prohibitive cost. Intensive efforts have been made during the last years in WOCs research with earth abundant elements.[13–15] Interestingly, first row transition metal oxides provide excellent catalytic activity in alkaline media, but their stability rapidly decays at lower pH, where only cobalt oxide analogues sustain good WOC performance in neutral media with the aid of phosphate electrolytes.[16,17]

To overcome the hydrolysis of transition metal oxides in neutral and acidic media, catalytically active metal ions have been incorporated into polyoxometalate (POM) frameworks, thus providing good stability over a large range of pH values.[18,19]

Moreover, as redox-active materials, POMs can afford different oxidation states without suffering major structural changes, exhibiting high stability under harsh working

conditions.[20] For instance, in 2008 a Ru-containing POM, $[Ru_4O_4(OH)_2(H_2O)_4(g\text{-}SiW_{10}O_{36})_2]^{10-}$, was reported as the first POM showing efficient water oxidation catalytic activity.[21,22] Regarding POMs based on earth abundant elements, Co-containing POMs (Co-POMs) are the most studied because of their good activity and remarkable stability under controlled working conditions. In 2010, the Co-POM with the formula $[Co_4(H_2O)_2(B\text{-}\alpha\text{-}PW_9O_{34})_2]^{10-}$ ($Co_4P_2W_{18}$) was reported as the first WOC of its kind.[23] This POM is composed of a tetracobalt-oxo core stabilized by two trilacunary Keggin moieties ($[B\text{-}\alpha\text{-}PW_9O_{34}]^{9-}$) forming the also-known Weakley sandwich (Figure 3.1).[24] In 2012, a high nuclearity Co-POM, $[Co_9(H_2O)_6(OH)_3(HPO_4)_2(PW_9O_{34})_3]^{16-}$ (Co_9), was reported to render efficient WOC activity, evolving O_2 for weeks without sign of fatigue or decomposition.[25] Later on, it was demonstrated that this Co-POM maintains its water oxidation capabilities with outstanding stability in the solid-state over a wide range of pH, surpassing the catalytic activity shown by benchmarking IrO_2 in strong acidic conditions.[26,27]

Iron, as one of the most abundant and less toxic transition metals, is a promising element to design cost-effective and durable catalysts.[28,29] The redox properties of iron make it essential in biological systems for O_2 involving processes, such as the nonheme iron complex that acts as an electrontransmitter in Photosystem-II.[30] Many iron-based catalysts have been reported with interesting and promising performance and good stability towards water oxidation catalysis.[31] Hydrated oxides (FeOOH),[32] FeOx/CNT composites (FeP@CNT),[33] iron-phosphate (FePO4)[34] and a trimetallic FeCoW oxide[35] are some examples of Fe-based WOCs used in basic (1 M KOH) media performing an overpotential of ca. 200 mV at 10 $mA \cdot cm^{-2}$. Moreover, incorporation of traces of iron into the nickel oxyhydroxide structure is known to dramatically enhance the catalytic activity.[36] Nevertheless, the studies of Fe-containing POMs as WOCs are scarce[37,38] and in some cases the POM acts as a catalyst precursor and not as the true active species.[39]

In addition, the reaction mechanism of the water oxidation catalysed by $Co_4P_2W_{18}$ at close-to-neutral pH was recently studied by computational means.[40] There, the active

species and the O–O bond formation steps were explored using a simple model system. Within this proposed mechanism the potential determining step corresponds to the O–H bond cleavage to facilitate the formation of the active species, a radical Co-oxyl species, through a proton-coupled electron transfer step. Thereafter the O–O bond formation occurs when this electrophilic, active species is attacked by a water molecule, working as a nucleophile. Taking advantage of this theoretical investigation and the extensive experimental studies carried out on the $Co_4P_2W_{18}$, other POMs with similar structural features may be studied to gain a deeper mechanistic understanding. This knowledge will allow to define a strategy for the design of novel efficient and cost-effective POMs working as WOCs. Hence, a clear case study is the Fe-containing POM $[(Fe^{III}OH_2)_2$-$Fe^{III}_2(PW_9O_{34})_2]^{6-}$ ($Fe_4P_2W_{18}$) firstly described by Hill and co-workers.[41] The electronic structure and redox properties of Fe-based anions have been reported previously.[42–45]

In this chapter, we present the water oxidation catalytic activity of $Fe_4P_2W_{18}$ and compare it with that of the $Co_4P_2W_{18}$. We have carried out our catalytic study at neutral pH and in the solid-state using the POM water-insoluble barium salt to assure structural stability. Moreover, we have investigated the reaction mechanism employing computational methods to determine the key aspects in comparison with those of the Co_4-WS. In addition, in order to attain more insight on the structure–reactivity relationship of POMs, we also investigated the OER catalytic properties of the Fe and Co monosubstituted Keggin moieties.

3.2. Results and Discussion

3.2.1.1. Experimental section

We have studied the WOC performance of $Fe_4P_2W_{18}$ at neutral pH and compared it with that of the cobalt analogue $Co_4P_2W_{18}$,[24] with the aim of elucidating the effect of the metal nature of the tetraoxo core belt on the catalytic activity. Furthermore, we have also examined the WOC activity of the iron and cobalt derivatives of the monosubstituted Keggin species, $[Fe^{III}(H_2O)PW_{11}O_{39}]^{4-}$ ($FePW_{11}$) and $[Co^{II}(H_2O)PW_{11}O_{39}]^{5-}$ ($CoPW_{11}$), to gain a deeper understanding on the structure–reactivity relationship of POMs.

The electrocatalytic water oxidation experiments were carried out in the solid-state using the water-insoluble barium salts of the POMs to prepare modified carbon paste (CP) electrodes. The choice of the countercation was made based on our previous works, where we showed its superior WOC performance compared with the cesium salts.[27,46] The catalyst content in the carbon blend was limited to 20% to avoid mechanical sensitivity due to the formation of oxygen bubbles.

The water-insoluble barium salts were obtained by metathesis from POM aqueous solutions. The catalytic performance was studied by running multiple (≥5) linear sweep voltammetry (LSV) scans using a three-electrode configuration with a Pt mesh as the counter-electrode and a Saturated Calomel Electrode (SCE) as the reference electrode. Three independent electrodes were tested in order to evaluate the reproducibility of the measurements.

LSV with 20% Ba-$Fe_4P_2W_{18}$/CP electrodes show a significant catalytic activity with increasing current density rapidly deviating from that obtained with catalyst-free CP electrodes (Figure 3.2). The experimental applied potential values required to reach 1 mA cm_2 for 20% Ba-$Fe_4P_2W_{18}$/CP and Ba-$Co_4P_2W_{18}$/CP are 1.560 V (η = 732 mV) and 1.512 V (η = 684 mV), respectively (see Figure 3.2 and Table 3.1), which represents an overpotential difference of 48 mV. Ba-$FePW_{11}$ and Ba-$CoPW_{11}$ show an apparent better WOC activity than the corresponding Weakley sandwich POMs, with a decrease in the overpotential values of ca. 70 mV to reach 1 $mA \cdot cm^{-2}$, with applied potentials of

1.495 V and 1.442 V, respectively. Again, the influence of the nature of the catalytically active metal center on the activity is noticeable with the cobalt analogue requiring a 53 mV lower potential than Ba-$FePW_{11}$ to achieve a current density of 1 $mA \cdot cm^{-2}$. This lower overpotential at the same total weight derives from the lower molecular weight of the POM-K salts. When we normalized the current density per total number of moles of catalyst, both POM structures show similar activity, with a slightly better performance in the case of the Weakley sandwich POMs, and a significantly better performance for the Co-POMs (Figure 3.2 and Table 3.1). This comparison suggests that the nature of the metal center seems to play a more important role in the WOC performance than the POM structure.

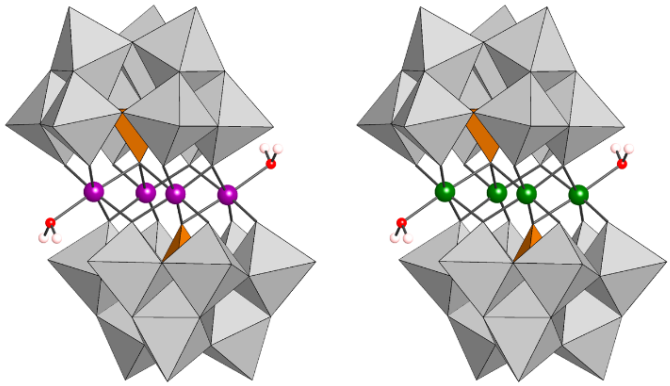

Figure 3.1. Polyhedral representation of $[(Co^{II}OH_2)_2Co^{II}_2(B\text{-}\alpha\text{-}PW_9O_{34})_2]^{6-}$ ($Co_4P_2W_{18}$), $[(Fe^{III}OH_2)_2Fe^{III}_2\ (B\text{-}\alpha\text{-}PW_9O_{34})_2]^{6-}$ ($Fe_4P_2W_{18}$).

The long-term stability of Ba-$Fe_4P_2W_{18}$ was confirmed by repetitive LSV demonstrates chemical stability during turnover conditions (Figure 3.3). And chronopotentiometry measurements at a constant current density of 1 $mA \cdot cm^{-2}$ for 4 hours and 20 hours (Figure 3.4). All POMs show good stability. Post-catalytic characterization of the recovered POMs after bulk water electrolysis confirms the structural stability of the compounds. No signs suggesting the evolution of the catalysts towards a new species, metal leaching or POM decomposition were detected. Raman spectroscopy is a surface-sensitive characterization technique that allows the identification of traces of new species formed on the surface of the catalyst.[46,47]

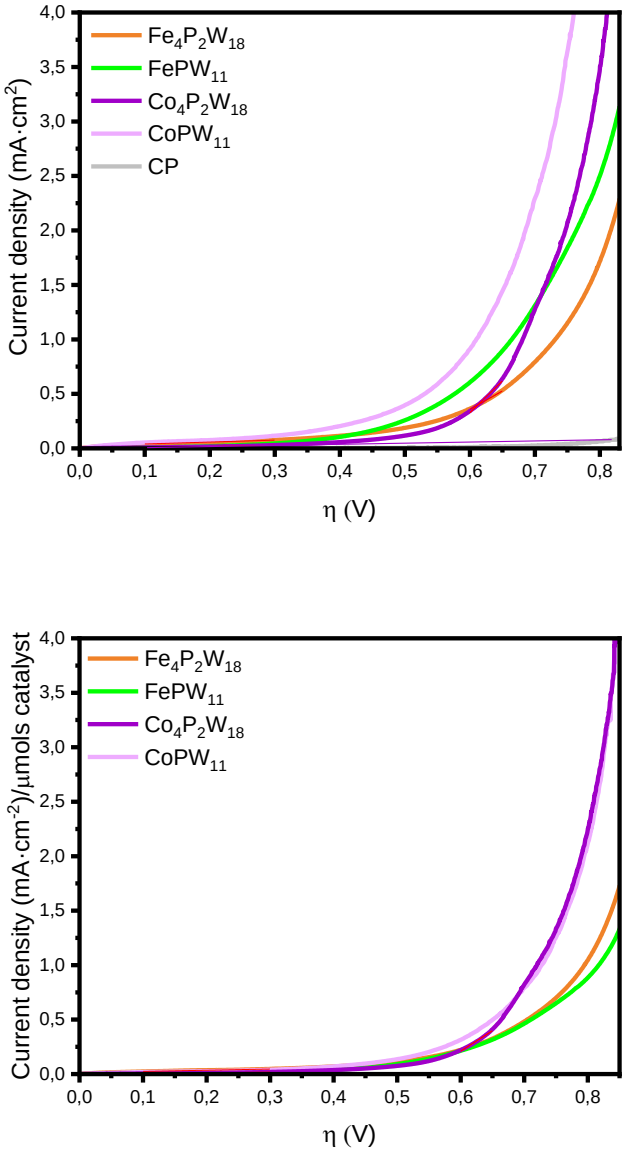

Figure 3.2. (Top) Linear sweep voltammetry of the 20% **Ba-POM**/CP working electrodes and (Bottom) linear sweep voltammetry normalized by the total number of moles of Ba-$FePW_{11}$, Ba-$Fe_4P_2W_{18}$, Ba-$CoPW_{11}$ and Ba-$Co_4P_2W_{18}$.

Table 3.2. Experimental and computed potentials (in V vs NHE) and overpotentials (in mV) for the POMs used in this study at neutral pH.

Potential / Overpotential	**Set**	**Co_4-WS[c]**	**Co-K**	**Fe_4-WS**	**Fe-K**
E_{app}[a]	Measured	1.512 ± 0.004	1.442 ± 0.010	1.560 ± 0.013	1.495 ± 0.008
η	@ 1 mA/cm^2	684 ± 4	614 ± 10	732 ± 13	666 ± 8
E_{app}'	Normalized	1.553 ± 0.006	1.555 ± 0.009	1.610 ± 0.010	1.642 ± 0.012
η'	@ 1 mA/cm^2 per μmol of catalyst	724 ± 6	727 ± 9	793 ± 10	813 ± 12
E_{DFT}[b]	BS1 theory level	1.54[d]	1.69	1.59	1.67
η_{DFT}		723	870	773	853
E_{DFT}	BS2 theory level	1.54	1.58	1.54	1.64
η_{DFT}		723	763	723	823

(a) Two sets of potentials and overpotentials were determined from measured current densities and from current densities normalized per μmols of catalyst (Figure 2); The experimental errors for the potentials were estimated as a standard deviation of three independent measurements. (b) Computed potentials and overpotentials were determined using a smaller (BS1) and a larger (BS2) basis set (see computational section for more details). Computed overpotentials values may be compared with experimental overpotentials at 1 mA/cm^2;[48] (c) An E_{app} of 1.52 V was reported for $Co_4P_2W_{18}$ using a Nafion ink on a GC electrode.[49] (d) Value from Ref. [40] corrected at pH7.

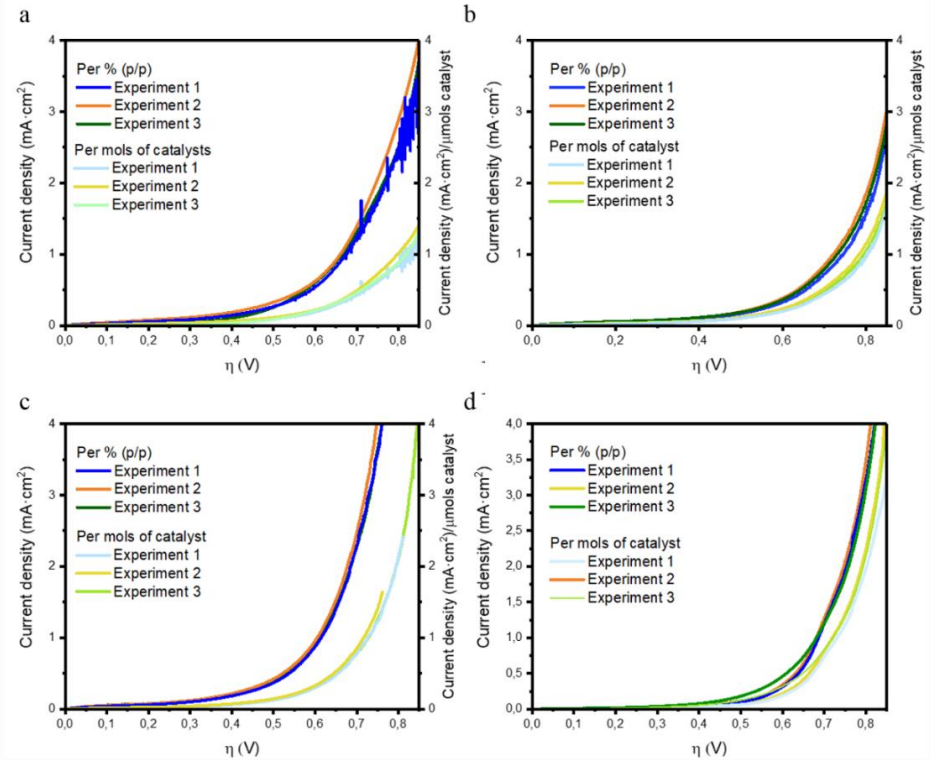

Figure 3.3. Repetitive linear sweep voltammetry of the 20% **Ba-POM**/CP working electrodes and linear sweep voltammetry normalized by the total number of moles of (a) Ba-$FePW_{11}$ (b) Ba-$Fe_4P_2W_{18}$ (c) Ba-$CoPW_{11}$ (d) Ba-$Co_4P_2W_{18}$ used in each blend. All the measurements were done in an aqueous potassium phosphate (50 mM) buffer solution at pH = 6.9 with KNO_3 (1 M) as the electrolyte.

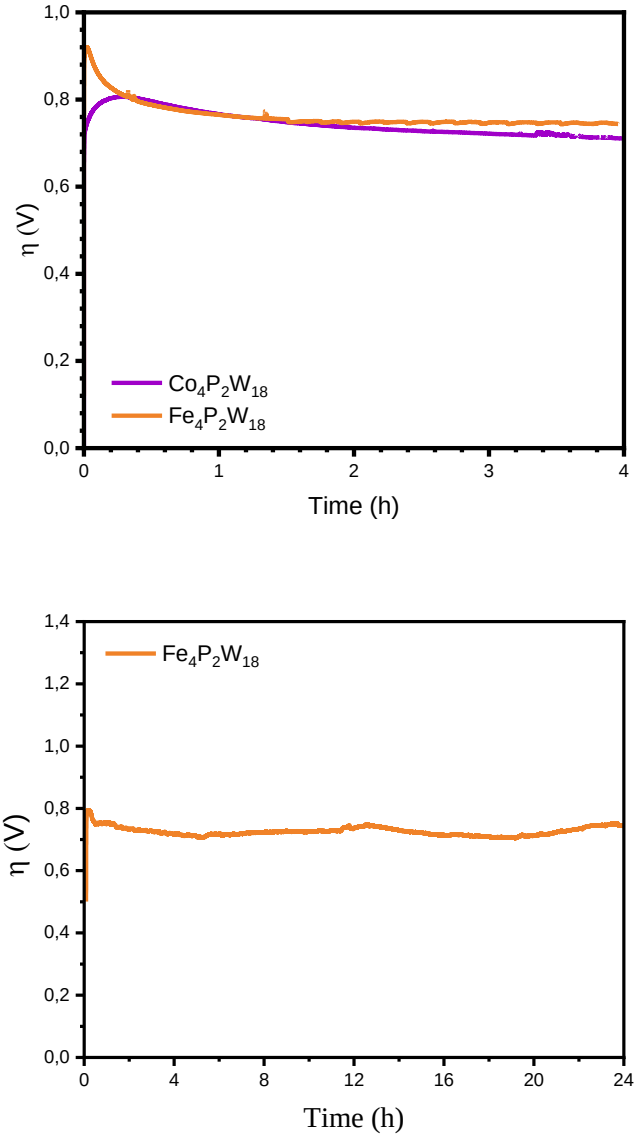

Figure 3.4. Chronopotentiometry at a constant current density of 1 mA·cm^{-2} using 20% (Top) Ba-$Fe_4P_2W_{18}$/CP and Ba-$Co_4P_2W_{18}$/CP (Bottom) Ba-$FePW_{11}$/CP. All the measurements were done in an aqueous potassium phosphate (50 mM) buffer solution at pH = 6.9 with KNO_3 (1 M) as the electrolyte.

The Raman and IR spectra of the recovered Ba-$Fe_4P_2W_{18}$ matches that of the freshly made compound (Figure 3.5). Moreover, the electrolyte solution was analyzed by Inductively Coupled Plasma Mass Spectrometry (ICP-MS) to identify metal leaching (Table 3.1). The concentration of all the elements were below the detection limit of the technique, suggesting a good chemical stability under the working conditions.

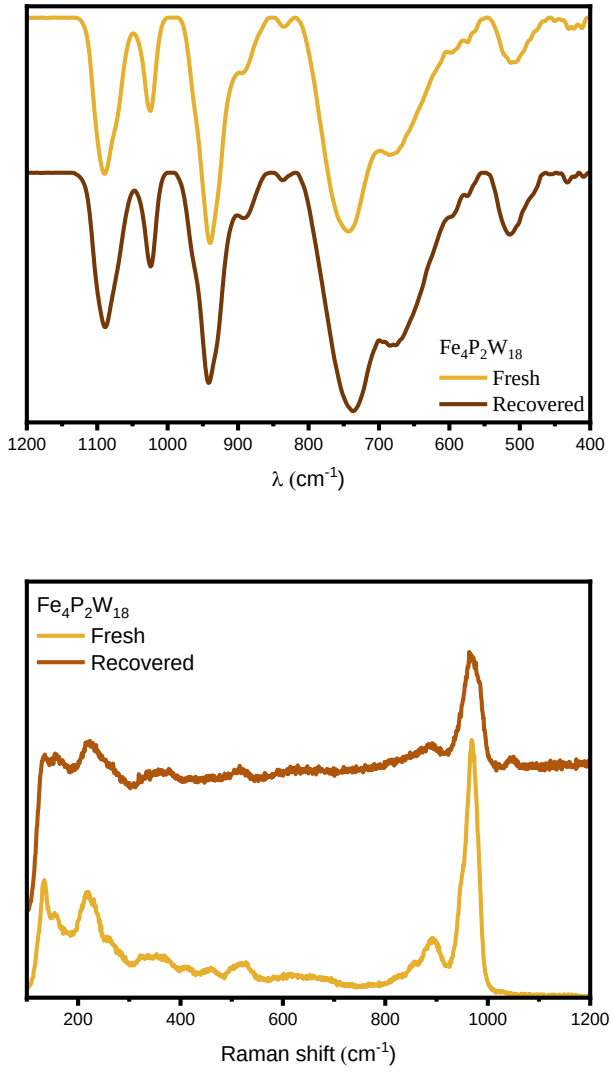

Figure 3.5. (**Top)** Raman spectra and **(Bottom)** IR spectra of Ba-$Fe_4P_2W_{18}$/CP before and after 2 h of electrocatalytic bulk water electrolysis at a constant current density of 1 $mA \cdot cm^{-2}$ in a pH = 6.9 potassium phosphate (50 mM) buffer solution with KNO_3 (1 M) as the electrolyte.

Table 3.1. ICP-MS analyses of the liquid reaction media after 2 h electrocatalytic water oxidation at a constant current density of 1 mA·cm^{-2} in H_2SO_4 (1 M) of stable compounds.

Mother liquor solution	Fe	Ba	W
Blank (KPi, 50mM; KNO_3 1M)	≤1.0 ppm	≤1.0 ppm	≤1.0 ppm
Ba- $FePW_{11}$	≤1.0 ppm	≤1.0 ppm	≤1.0 ppm
Ba-$Fe_4P_2W_{18}$	≤1.0 ppm	≤1.0 ppm	≤1.0 ppm

Moreover, the oxygen evolved employing Ba-$Fe_4P_2W_{18}$ during a chronopotentiometric experiment at 1 mA·cm^{-2} for 30 minutes was measured employing a fluorescence probe. This measurement confirms a faradaic oxygen production (>91%) compared with the theoretical amount of oxygen expected from a stoichiometric 4e$^-$ reaction (Figure 3.6)

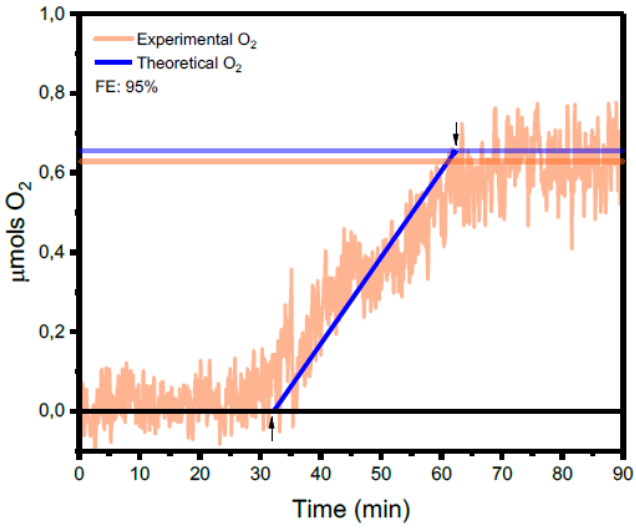

Figure 3.6. Oxygen evolution detection (orange) of the 20% Ba-$Fe_4P_2W_{18}$/CP during water electrolysis (at a constant current of 1 mA · cm^{-2}) in an aqueous potassium phosphate (50 mM) buffer solution at pH = 6.9 with KNO_3 (1 M) as the electrolyte. Theoretical oxygen evolution (blue) taking into account a constant current of 1 mA · cm^{-2}. The arrows indicate initial and final electrolysis times.

In order to understand better the origin of the different WOC activities shown by Ba-$Fe_4P_2W_{18}$ and Ba-$Co_4P_2W_{18}$, we calculated the double-layer capacitance (Cdl) of the modified CP electrodes, which is expected to be proportional to the total electrocatalytic active surface area. Ba-$Fe_4P_2W_{18}$ electrodes show lower Cdl values than Ba-$Co_4P_2W_{18}$ ones, which indicates that the cobalt analogue possesses an intrinsically higher

electrocatalytic surface area than the iron derivative (Figure 3.7). This difference can be somehow related to the total charge of the POM, which determines the number of cations needed to counterbalance the high anionic charge of the POMs. Hence, a higher number of countercations may lead to a higher number of accessible active sites on the insoluble POM particles.

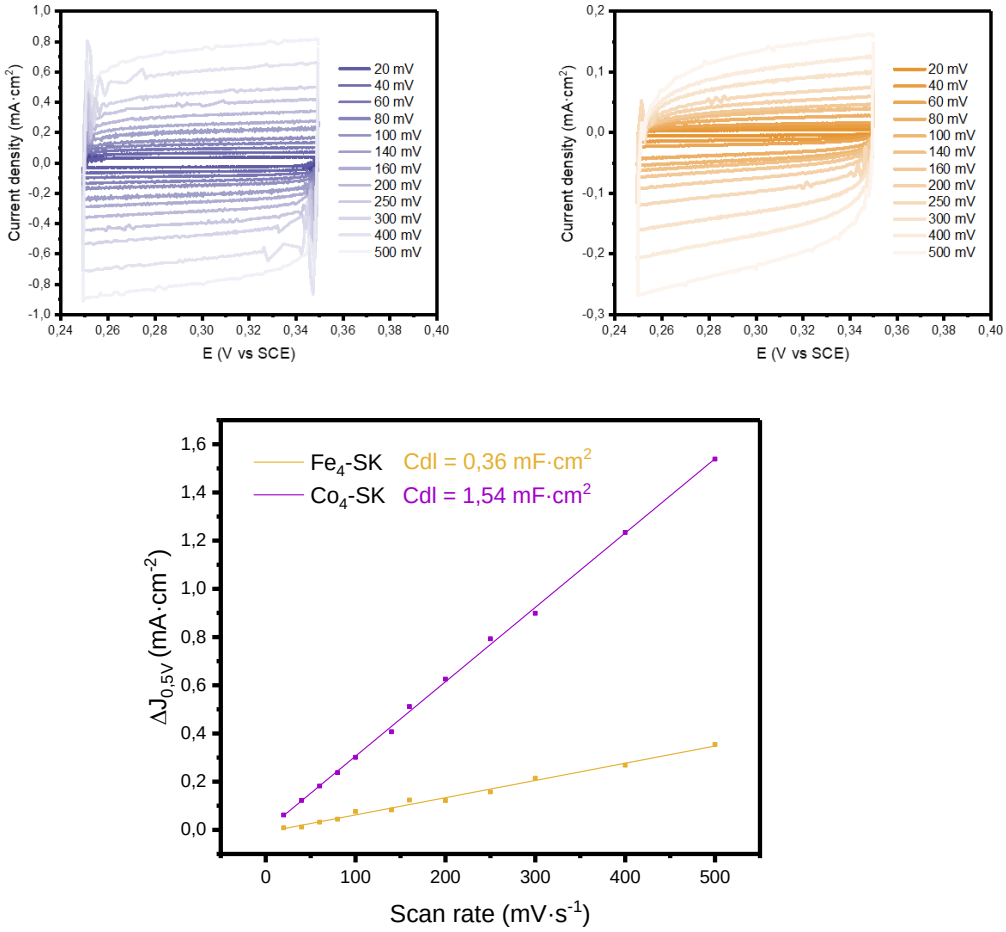

Figure 3.7. Double-layer capacitance (C_{dl}) measurements in a potassium phosphate (50 mM) buffer solution at pH = 6.9 with KNO_3 (1 M) as the electrolyte for 20% Ba-$Fe_4P_2W_{18}$/CP (orange) and 20% Ba-$Co_4P_2W_{18}$/CP (purple) electrodes. (Top) Cyclic voltammograms in the non-Faradaic region with increasing scan rates between 20 and 500 mV. (Bottom) Plot of Δj (j_a-j_c) versus the scan rate where the slope is twice the C_{dl}. Within the measured potential range, the current response does not arise from any redox or catalytic process, so it is attributed to the charging of the double layer.

We also studied the Tafel behavior of these POMs through steady-state analysis (Figure 3.8). The Tafel slope depends exclusively on the rate-determining step of the catalytic reaction, being independent on the total number of active sites.[50] We found Tafel slopes of 99 mV dec^{-1} and 73 mV dec^{-1} for Ba-$Fe_4P_2W_{18}$ and Ba-$Co_4P_2W_{18}$, respectively. These values indicate a competition between a chemical and an electron-transfer limiting step for both catalysts and confirm the faster kinetics for the Co-POM.[27]

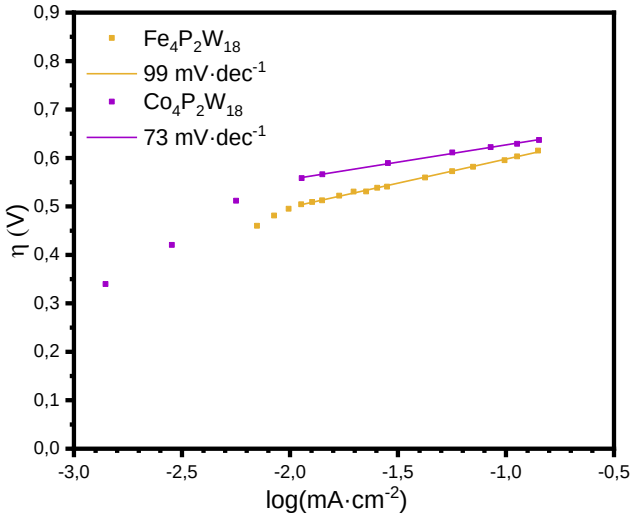

Figure 3.8. Tafel behavior of 20% Ba-$Fe_4P_2W_{18}$/CP and Ba-$Co_4P_2W_{18}$/CP electrodes obtained from steady-state chronoamperometric experiments. All the measurements were done in an aqueous potassium phosphate (50 mM) buffer solution at pH = 6.9 with KNO_3 (1 M) as the electrolyte.

3.2.2. Theoretical section

3.2.2.1. Determination of the pKa values

The protonation–deprotonation equilibrium is key to understand and predict the mechanistic behaviour of POMs as WOCs.[40] Luckily, we have been able to determine experimentally a pKa value of 6.0 for $Fe_4P_2W_{18}$ (Figure 3.9) by acid–base titration. In our previous work we computationally estimated a pKa value for $Co_4P_2W_{18}$ above 10[40] where the POM becomes unstable hindering the experimental determination.[20,51,52] The different pKa values between $Fe_4P_2W_{18}$ and $Co_4P_2W_{18}$ are attributed to a stronger metal center–O_{water} interaction in the case of iron with respect to the cobalt analogue, due to the higher oxidation state of the metal (Fe^{III} vs. Co^{II}).

We have also studied the protonation–deprotonation equilibrium by computational means. The computed pKa value for $Fe_4P_2W_{18}$ is 6.1, which is in very good agreement with experiments. It is worth noting that the computational M–O_w distances in the aqua system are 2.151 Å and 2.220 Å for $Fe_4P_2W_{18}$ and $Co_4P_2W_{18}$, respectively, supporting that $Fe_4P_2W_{18}$ has a stronger M–O_w interaction than the cobalt derivative.

In order to get more insight into the deprotonation of these type of POMs, we have computed and determined experimentally the pK_a value of the Fe–monosubstituted Keggin POM ($FePW_{11}$) to be 4.4 and 4.3, respectively. The value is slightly lower than that of $Fe_4P_2W_{18}$, probably due to the difference in the overall charge of these two POMs (-6 for the sandwich $Fe_4P_2W_{18}$ and -4 for the monosubstituted $FePW_{11}$). We have used the Bond Valence Sum model[53] to estimate the oxidation state of the Fe in both systems, obtaining values of 2.7 for the sandwich $Fe_4P_2W_{18}$ and 2.9 in the case of the monosubstituted $FePW_{11}$. This also agrees with the Fe–O distances that are a slightly larger for the sandwich $Fe_4P_2W_{18}$.

$Fe_4P_2W_{18}$ possesses a C_2h symmetry with two equivalent aqua ligands. Consequently, this POM shows two different pK_a values derived from the removal of a proton from each H_2O ligand. The first deprotonation changes the overall charge of the POM to -7, thus rendering the second deprotonation higher in energy. According to our DFT

calculations, the value of pKa_2 is 9.0. Unfortunately, we could not establish the pKa_2 value during the acid–base titration experiments up to pH = 10, after which $Fe_4P_2W_{18}$ becomes unstable. Nevertheless, we can assume that the second deprotonation would occur at higher pH values than the catalytic working conditions we are considering in this work and, hence, it will not be involved in our proposed reaction mechanism. We can conclude that, at neutral pH, both Fe-POMs are present as POM-Fe^{III}–OH species at the resting state (vide infra).

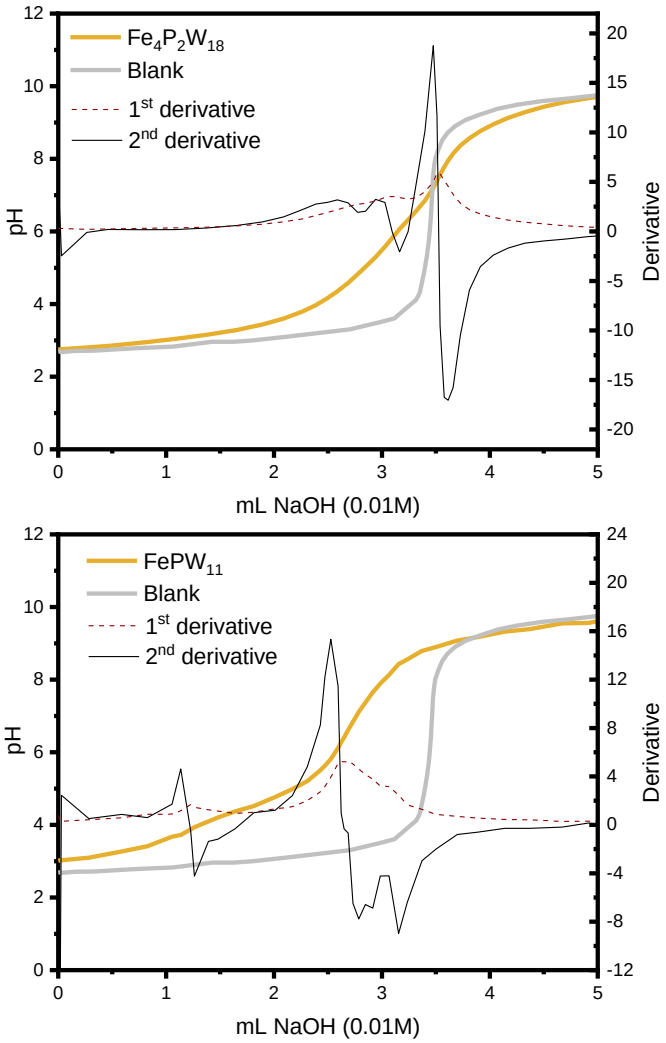

Figure 3.9. Acid-base titration of K-$Fe_4P_2W_{18}$ (top) and K-$FePW_{11}$ (bottom) in a 0.010 mM $HClO_4$:$NaClO_4$ solution with the addition of a 0.010 mM NaOH solution.

3.2.2.2. Reaction mechanism

The $Co_4P_2W_{18}$, analogue to $Fe_4P_2W_{18}$, was mechanistically investigated in our previous work.[40] The postulated mechanism for $Co_4P_2W_{18}$ was described in two stages: first the electrochemical formation of the active species via an electron-then-proton transfer event followed by a proton coupled electron transfer (PCET) step. In the second stage of the mechanism, the active species leads to the O–O bond via a water nucleophilic attack (WNA). Additionally, the electronic structure of $Fe_4P_2W_{18}$ was computationally investigated by some of us back in 2007.[45]

In the present work, we followed a similar strategy defining as starting system the four iron centers to be Fe^{III} with a high-spin d^5 electron configuration. The magnetic coupling between the iron centers was not considered. We investigated the influence of the metallic center on the key steps leading to the formation of the active species and the O_2 bond formation process. Experimentally, water oxidation catalysis is performed electrochemically, where an applied potential drives the catalytic reaction. As found in the cobalt analogue, we expect to differentiate two governing factors: (i) the oxidative character of the active center, i.e. the ability to lose electrons and reach high oxidation states and (ii) the rate of the non-electrochemical steps, i.e. the WNA, which is driven by the electrophilicity of the oxidized POM, and the proton transfer events that are dictated by the acid/base properties. In addition, the chemically controlled equilibrium can determine, as we will see below, the resting state species and the kinetics of the global process.

Thus, we have analyzed each step of the $Fe_4P_2W_{18}$ catalyzed water oxidation cycle at pH 7 starting from the S_1 Fe^{III}–OH species. The different steps involved in the catalytic cycle are summarized in Figure 3.10 and they will be described below.

Formation of the active species

As discussed above, $Fe_4P_2W_{18}$ (S_1^0, the (Fe^{III}–OH2) species) has an experimental pKa value of 6.0, which is in very good agreement with our computed value of 6.1. This means that the speciation of $Fe_4P_2W_{18}$ depends on the pH. Above pH 6, there is a high

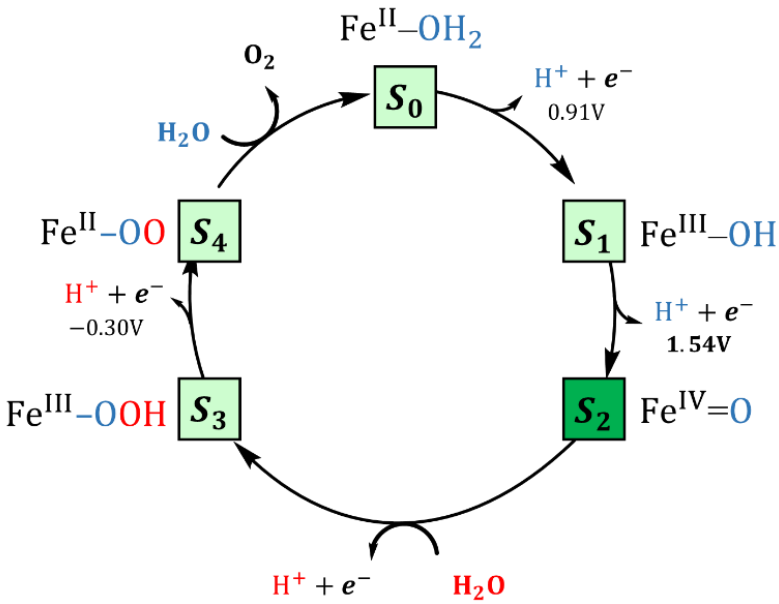

Figure 3.10. Water oxidation mechanism using Fe-POMs considered as single-site catalysts. Potentials and energies correspond to the catalytic cycle computed for $Fe_4P_2W_{18}$ electrocatalyst. The dark green square indicates the active specie.

deprotonation degree of $Fe_4P_2W_{18}$, leading to the formation of the hydroxyl speciesS_1 (Fe^{III}–OH), whereas at pH values below 6 the aqua species (S_1^0) is favoured. As the present work is carried at pH 7 (one pH unit higher than the pKa value), S_1 is the predominant form of the catalyst, where $S_1/S_1^0 \approx 8$ (according to Henderson–Hasselbalch equation). Furthermore, any oxidation process from the iron-aqua species (S_1^0) would be highly energy demanding because the computed potentials are 2.34 and 2.16 V involving either an electron transfer (ET) or a proton-coupled electron transfer (PCET), respectively (see Figure 3.11).

The first step of the reaction starting from the resting state S_1 (Fe^{III}–OH) species clearly consists of a PCET event leading to the iron-oxo species S_2 (Fe^{IV}=O). The sequential electron-then-proton transfer pathways are more energy demanding, as can be seen in the square diagram in Figure 3.11. In this figure, vertical processes correspond to oxidation reactions (ET), horizontal ones to proton cleavage (O–H, only proton transfer (PT) acid–base reaction) and diagonal arrows represent PCET steps with one electron and one proton loss.

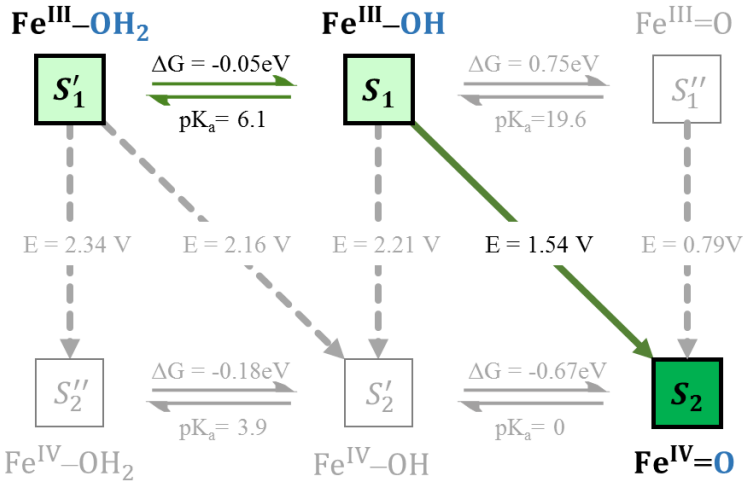

Figure 3.11. Square diagram representation of the PCET, PT and ET events for $Fe_4P_2W_{18}$ acting as WOC starting from the resting state species at pH = 7 to reach the *active* species. Potentials are given in V vs NHE for the electrochemical processes (PCET and ET), while the chemical processes related to acid-base equilibria (PT) are expressed as free Gibbs energy (in eV) with the corresponding pK_a value.

Therefore, the first step S_1 (Fe^{III}–OH) / S_2 (Fe^{IV}=O) takes place, according to calculations, at 1.54 V. An ET would require a very high potential of 2.21 V. This is because the hydroxyl ligand does not stabilize high oxidation states such as Fe^{IV}. Moreover, the deprotonation of S_1 is thermodynamically unfavorable, and it would require strong basic conditions, where the $Fe_4P_2W_{18}$ is unstable. The S_1 (Fe^{III}–OH) species is expected to have five unpaired electrons in each iron. However, DFT calculations tend to somewhat over delocalize the electron spin density leading to values of 4.1 e^- on all four irons and 0.4 e^- on the hydroxyl oxygen (see Table 3.2).

S_2 (Fe^{IV}=O), shows an electron spin density on the reactive iron of 3.1 e^- and 0.6 e^- on the terminal oxo moiety. Hence, this species can be regarded as an average of the two Lewis structures Fe^{IV}=O and Fe^{III}–Oc. The computed spin density is more consistent with a Fe^{IV}=O species, since a complete electron has been removed from the iron center upon one-electron oxidation of the Fe^{III}–OH species. The computed Fe–O bond length of 1.609 Å also suggests that S_2 must be seen preferably as an Fe^{IV}=O species (Figure 3.12). However, the high electron spin density localized at the terminal oxygen in S_2,

gives a significant reactivity to this oxygen. At this point, the reaction mechanism can proceed through two different pathways, either the S_2 (Fe^{IV}=O) species is the electrophilic reactive center (WNA takes place at this point) or the S_2 is one-electron oxidized to give a Fe^{V}=O species. The latter requires a high applied potential (2.11 V), similar to that reported for the cobalt analogue anion.[54] Given that the LUMO of S_2 (Figure 3.12a) has an important p(oxo) contribution, it is expected that S_2 may act as an electrophile and be the active species that oxidizes water.

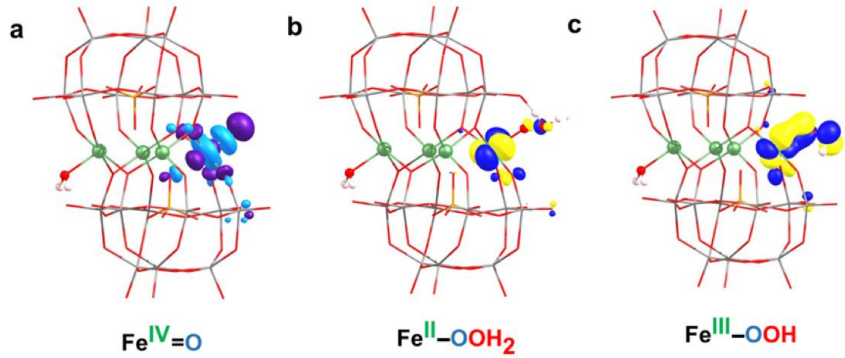

Figure 3.12. (a) LUMO of Fe^{IV}=O (**S2**), (b) SOMO (β) of Fe^{II}-OOH_2 (**Int**) and (c) SOMO (β) of Fe^{III}-OOH (**S3**) species.

Table 3.2. Anion charge, Mulliken spin densities at the reactive Fe center, active and nucleophilic O (O_{WNA}) and selected bond distances for different intermediates and transition states of the Fe_4-WS catalyzed water oxidation cycle (a)

	S_0 $Fe^{II}OH_2$	S_1' $Fe^{III}OH_2$	S_1 $Fe^{III}OH$	S_2 $Fe^{IV}O$
Charge	-7	-6	-7	-7
ρ(Fe)	3.778	4.137	4.100	3.125
ρ(O)	0.027	0.070	0.414	0.563
ρ(O_{WNA})	-	-	-	-
d(Fe–O)	2.227	2.151	1.836	1.609
d(O–O_{WNA})		-	-	-
	S_0 [$Fe^{II}O\cdots OH_2$+H_2O]	S_1' Fe^{II}–O–OH_2	S_1 Fe^{III}–O–OH	S_2 Fe^{II}–O–O
Charge	-7	-7	-7	-7
ρ(Fe)	3.769	3.744	3.912	3.741
ρ(O)	0.139	0.094	0.552	1.007
ρ(O_{WNA})	-0.126	-0.003	0.198	1.005
d(Fe–O)	1.818	2.001	1.964	3.924
d(O–O_{WNA})	1.700	1.501	1.375	1.214

(a) Bonds lengths are in Å and Mulliken spin densities in e. All data correspond to BS2 calculations without explicit water molecules except for TS_2 and Int, which values correspond to the calculations performed with an extra water molecule. (b) Int: Intermediate species generaed from TS2.

O–O bond formation

After reaching the active species S_2 (Fe^{IV}=O), the O–O bond formation should take place via a water nucleophilic attack, leading to the formation of an intermediate species *Int* (Fe^{II}–OOH_2). As shown in Figure 3.12, the attack of a water molecule induces a significant electronic reorganization at the iron center.

The formation of a relatively strong O–O bond of 1.501 °A is combined with an elongation of the Fe–O bond from 1.609 °A in S_2 to 2.001 °A in *Int*. In turn, the iron centre is formally reduced from IV to II. We computed the corresponding transition state (TS) exploring different mechanistic possibilities, i.e. different hydrogen bond modes between the attacking water molecule and the oxygen atoms of the POM cluster, and different number of water molecules.

Using the basis set BS_2, two different TSs were located when computing just one water molecule (see Figure 3.14). Both TSs showed relatively high activation energies (25.6 and 25.7 kcal·mol^{-1}). In the first TS, namely TS_{1B}, the attacking water molecule is stabilized by the formation of a hydrogen bond with one of the bridging oxygens of the POM (H_{wat}–O_{POM} distance of 1.482 °A). In this case, the O–O and Fe–O distances are 1.715 °A and 1.846 °A. In the second TS, TS_{1T}, the hydrogen bond occurs between the attacking molecule of water and a terminal oxygen atom of the POM, with a larger H_{wat}–O_{POM} distance (1.508 °A) than in the previous case.

The weaker hydrogen bond interaction yields a shorter O–O distance of 1.664 °A, and a longer Fe–O distance of 1.860 °A, compared to TS_{1B}. Remarkably, both TSs have almost identical activation energies, even though the oxygen atoms placed at the Fe–O–W bridging positions have been shown to be the most basic atoms in the POM structure.[55–58] However, the computed structure in TS_{1B} is more constrained than that in TS_{1T}, where the O_{POM}–O_{wat}–O_{Fe} angle is 81.1º for TS_{1B} and 94.0º for TS_{1T}. Arguably, both factors may compensate each other, resulting in almost isoenergetic structures (see Figure 3.14)

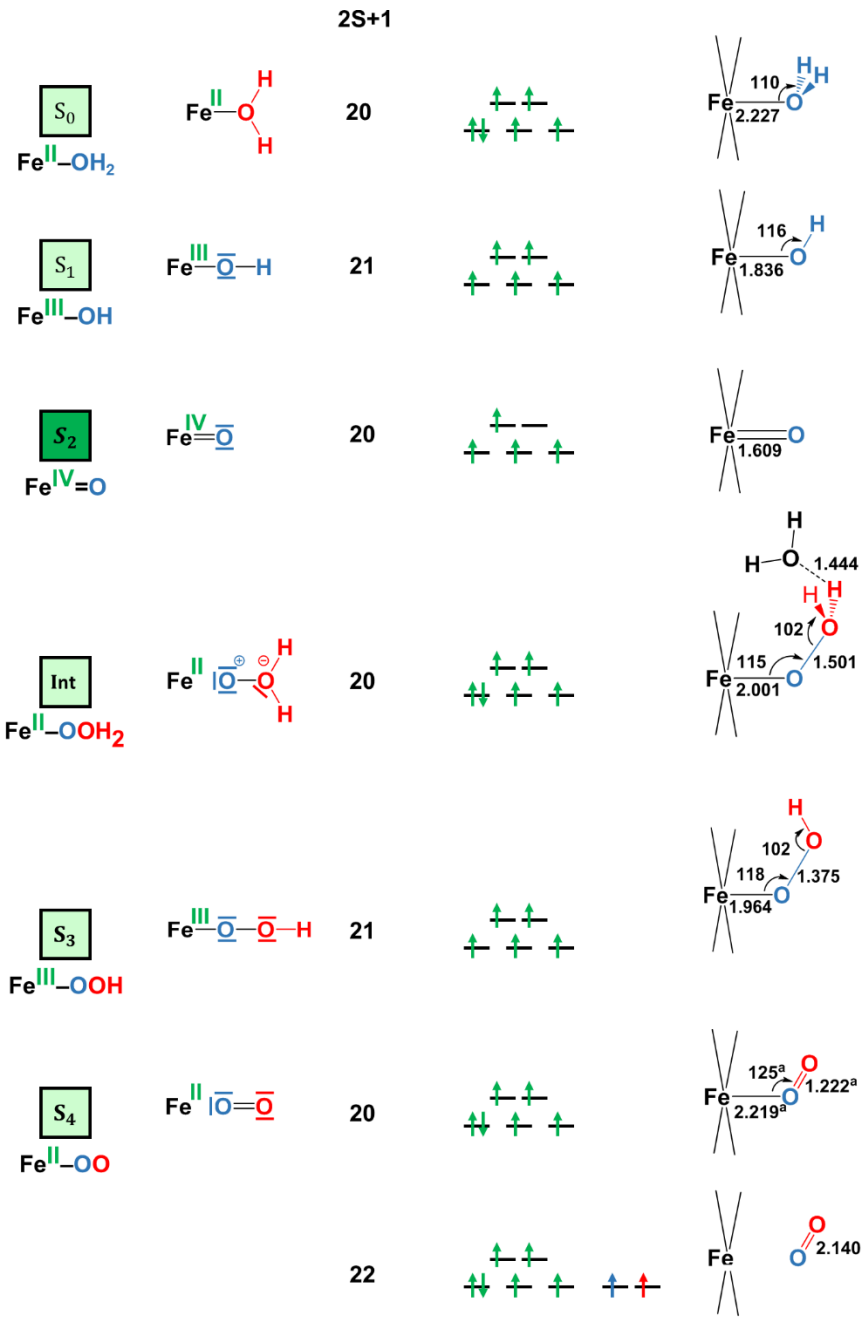

Figure 3.13. Electronic and structural data for S_0 to S_4 species. Angles are given in degrees and bond lengths in Angstroms. [a]The geometrical parameters of this structure were obtained using BS1.

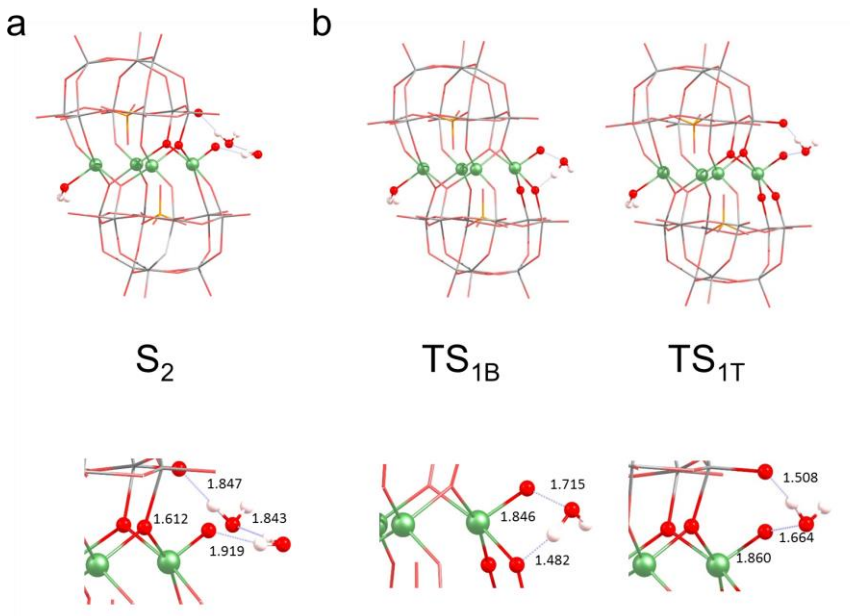

Figure 3.14. Ball and stick representations of (a) **S_2** specie (b) **TS_{1B}**, **TS_{1T}** species.

When a second molecule of water is included in the calculations (TS_2), the activation barrier significantly decreases to 19.8 kcal·mol^{-1} (0.86 eV). In this case, we could only find a transition state that exhibits hydrogen bonds with terminal oxygens (Figure 3.15). We have repeated these series of calculations using the smaller basis set BS_1. In general, the results are very similar but with lower activation energy barriers.

According to these results, TS2 is the preferred pathway for the O–O bond formation. This step should be rather fast, since the computed activation energy is easily surmountable at room temperature. Moreover, bulk water and buffering molecules may assist in speeding up the process. The transition state TS_2 leads to the *Int* (Fe^{II}–OOH_2) species, where the hydrogen atoms of the inserted water molecule form hydrogen bonds with both a terminal oxygen atom of the POM and the oxygen atom of the assisting water molecule.

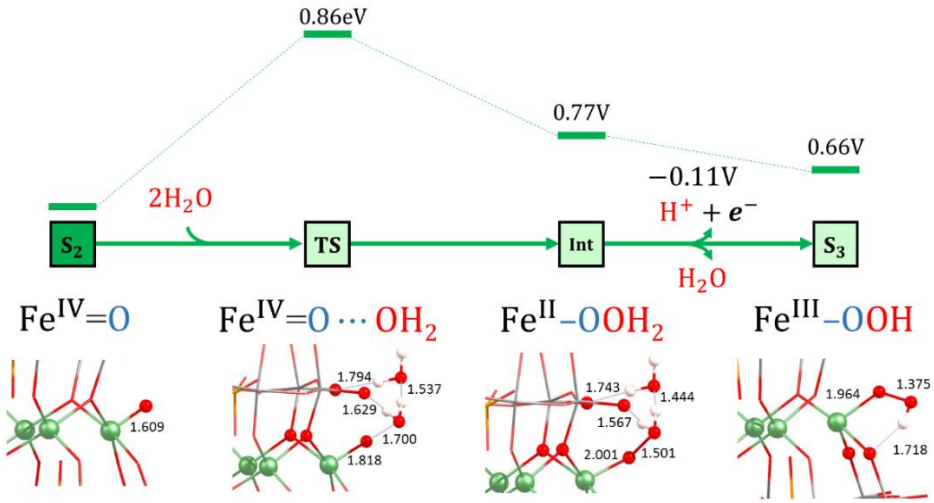

Figure 3.15. Ball and stick representations of **S_2**, **TS_2**, **Int** and **S_3** species. For a description see footnote in Table 2. Selected distances are in Å. Energies are given in eV. The **S_2** to **Int** transformation is controlled thermally, whereas the **Int** to **S_3** one is controlled electrochemically.

Notably, the WNA process involves the reorganization of the electrons in the active metal center, which is the result of an electron-donation effect from the attacking water molecule to the iron center (Figure 3.13). This is reflected in a reduction of the oxidation state of the active iron center from Fe^{IV} to Fe^{II}. Indeed, Int (Fe^{II}–OOH_2) species presents a spin density of 3.7 e^- on the reactive iron, whereas a negligible spin density is localized on the nearby oxygens (Table 3.2). The Fe^{II} nature of this atom is also confirmed by orbital inspection. Figure 3.12b shows the SOMO beta localized in the reactive iron atom indicating that it cannot have a higher oxidation state. In addition, a bond distance of 1.501 °A indicates the formation of a relatively strong O–O single bond, which is combined with an elongation of the Fe–O bond length from 1.609 °A in S_2 to 2.001 °A in *Int*.

The influence of the POM structure was analyzed by computing the corresponding TSs for the Fe–K anion. The results are very similar to those obtained for $Fe_4P_2W_{18}$, even though all the free activation energies are slightly higher (Table 3.3). One possible explanation for this is that all hydrogen bonds occur with bridging oxygen sites (Figure 3.16) The computed energies agree well with the experimental normalized current densities (Figure 3.2), where $Fe_4P_2W_{18}$ shows slightly better OER activity than $FePW_{11}$.

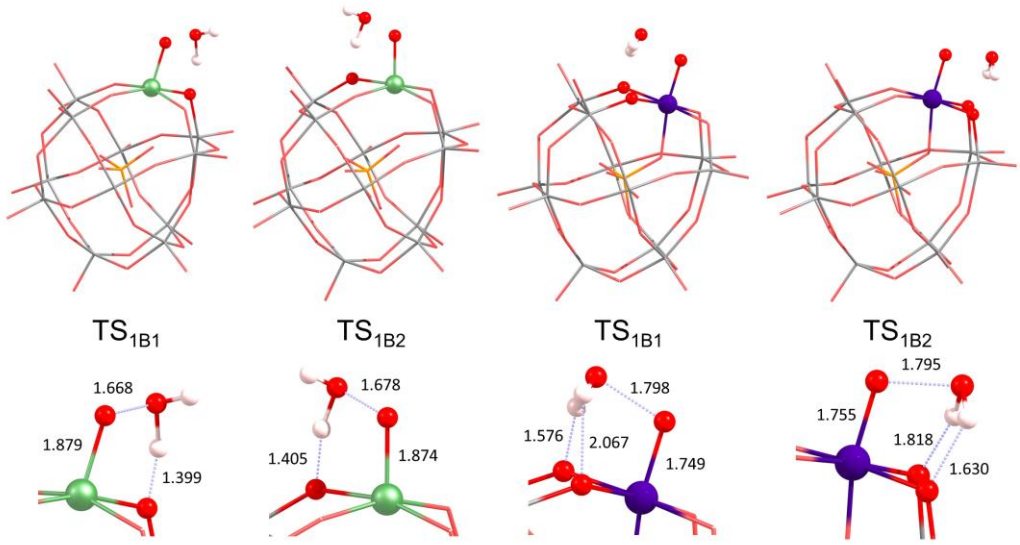

Figure 3.16. Structures of the computed transition states for **Fe-K** and **Co-K** using one molecule of water using the BS2 level of theory. Selected distances are given in Å.

We also compared the activation barriers between the Fe and Co based POMs using the small basis set BS_1. The reported Gibbs free energy for $Co_4P_2W_{18}$ in TS_{1B} was 22.9 kcal·mol^{-1},[40] which corresponds to a 0.3 kcal·mol^{-1} lower energy than the corresponding value for $Fe_4P_2W_{18}$. Additionally, we have obtained a systematic series of results for the $CoPW_{11}$ catalyst using BS_1 and BS_2. In this case, the activation barriers were found to be ca. 2 kcal·mol^{-1} lower in energy than the Fe analogue (Table 3.3). These results are consistent with the greater catalytic activity shown by the cobalt compounds (Figure 3.2).

Table 3.3. Comparison of free activation energy barriers for O-O bond formation using Fe and Co monosubstituted Keggin anions as catalysts.

POM	Basis Set	TS_{1B1}	TS_{1B2}
$FePW_{11}$	BS2	27.3 [(a)]	27.3 [(a)]
	BS1	25.5	25.1
$CoPW_{11}$	BS2	25.5 [(a)]	25.2 [(a)]
	BS1	24.0	23.2

O_2 evolution

Once the *Int* (Fe^{II}–OOH_2) species is reached, the following steps in the reaction mechanism are two PCET events that lead to the oxygen evolution from the reaction site. Finally, the POM is regenerated by adding a water molecule followed by a last PCET event, leading to the resting sate S_1 (Fe^{III}–OH) species. *Int* (Fe^{II}–OOH_2) is not a very stable intermediate, which easily transforms into S_3 (FeIII–OOH) by removing one electron from the SOMO (β) localized at the Fe atom (Figure 3.12b). A direct consequence is that the electron spin density slightly increases at the Fe center, together with a much larger increase at the reactive O atom (Table 3.2). This suggests that S_3 would probably be better represented by a combination of the two resonance forms $Fe^{III}-\overline{O}-\overline{O}-H \leftrightarrow Fe^{II}-\dot{O}-\overline{O}-H$.

The next PCET event involves the oxidation and deprotonation of the hydroperoxo ligand of the S_3 (FeIII–OOH) species due to the significant contribution of the p(O) orbital in its SOMO (Figure 3.12c). This step leads to the formation of the S_4 (Fe^{II}–OO) species in a very favored process with an associated potential of -0.30 V. It is worth mentioning that an electron-donation effect is again observed from ligand to metal, which implies the formal reduction of the iron center from Fe^{III} to Fe^{II}. It must be noted that all attempts to allocate S_4 (Fe^{II}–OO) as "end-on" (η^1) or "side-on" (η^2) led to an adduct with a long Fe–O_2 distance, where O_2 can be considered uncoordinated to the metal center. A structure with coordinated O_2 similar to the one found for the cobalt analogue could be located by using BS_1. However, this structure is found 0.8 kcal·mol^{-1} above the uncoordinated equivalent (2S + 1 = 20) and at 17.0 kcal·mol^{-1} above the equivalent structure with uncoordinated triplet oxygen (2S + 1 = 22). This indeed suggests that O_2 is a very labile ligand in this POM.

Once the oxygen molecule is released, a new water molecule will favorably coordinate to iron (ΔG = -8.6 kcal·mol^{-1}), to form the S_0 (Fe^{II}–OH_2) species. The last step consists in the regeneration of the catalyst to its resting state from S_0 (Fe^{II}–OH_2). This step can occur via a PCET step that leads directly to S_1 (Fe^{III}–OH), or through a sequential

electron-then-proton transfer event at pH 7. Both paths are expected to occur applying a potential below +1 V.

The overall mechanism can be described in two equivalent ways: (i) taking the initial species S_1 (Fe^{III}–OH) as the initial stage (PCET + WNA + 2PCET + O_2 evolution + PCET) or (ii) taking the S_0 (Fe^{II}–OH_2) species as the initial stage (2PCET +WNA + 2 PCET + O_2 evolution). The latter mechanism is analogous to other postulated ones for water oxidation, in which usually two protons and two electrons are released (coupled or not) before the water nucleophilic attack.[59] The major difference here is that the S_0 (Fe^{II}–OH_2) species naturally suffers a PCET event in solution under aerobic conditions, yielding the S_1 (Fe^{III}–OH) species in the crystalline solid. Once it enters the WOC reaction, the complete cycle is needed to move the reaction further. Either way, the potential-limiting step in the reaction mechanism is the S_1 (Fe^{III}–OH) / S_2 (Fe^{IV}=O) PCET event with a required applied potential of 1.54 V, whereas a chemical barrier of 19.8 kcal·mol^{-1} (0.86 eV) must be overcome to form the O–O bond through a WNA step.

3.3. Conclusions

We have studied the electrocatalytic OER activity in neutral media of the $[(FeIIIOH_2)_2Fe^{III}{}_2(B\text{-}\alpha\text{-}PW_9O_{34})_2]^{6-}$ ($Fe_4P_2W_{18}$) and $[(Fe^{III}OH_2)PW_{11}O_{39}]^{4-}$ ($FePW_{11}$) polyanions. The insoluble barium salts of the POMs were used to modify carbon paste electrodes and their activities were compared with that of the isostructural cobalt derivatives. Experiments show that both Fe-POMs display similar OER activity, and slightly slower kinetics than the Co-POM counterparts.

The speciation of molecular WOCs at the working conditions is key to understand the reaction mechanisms. Acid–base titration experiments and DFT calculations allowed us to calculate a pK_{a1} value of 6.0 in the case of $Fe_4P_2W_{18}$ and 4.3 for $FePW_{11}$. This indicates that under our experimental conditions of pH 7, both Fe-POM catalysts are found as POM-Fe^{III}–OH species (S_1) in the solid. Thus, a detailed DFT study of the OER mechanism promoted by $Fe_4P_2W_{18}$ shows two key steps in the catalytic reaction, (i) the potential-limiting step, S_1 (Fe^{III}–OH) / S_2 (Fe^{IV}=O), proceeds via a PCET event and requires an applied potential of 1.54 V; (ii) the chemical-limiting step corresponds to the O–O bond formation during the WNA and has an associated activation barrier of 19.8 kcal·mol^{-1} (0.86 eV). Moreover, we have seen that the presence of hydrogen bonds during the WNA helps in decreasing the activation barrier for the O–O bond formation.

These hydrogen bonds are more effective in the sandwich species compared to the monosubstituted Keggin structures, as illustrated by their calculated lower activation energies. Despite the different initial states in the solid for $Fe_4P_2W_{18}$ (S_1) and $Co_4P_2W_{18}$ (S_0) at neutral pH, the computed potential-limiting steps Fe^{III}–OH/ Fe^{IV}=O and Co^{III}–OH / Co^{III}–O· involve analogous associated energies. These results are in good agreement with experimental observations, since $Fe_4P_2W_{18}$ requires just a higher applied potential than $Co_4P_2W_{18}$. Moreover, the lower Tafel slope displayed by $Co_4P_2W_{18}$ indicates faster kinetics than $Fe_4P_2W_{18}$, which correlates well with the lower activation barriers found for the Co-POM.

It is very illustrative to see that even though POM-Fe^{III}OH and POM-$Co^{II}OH_2$ anions show significant differences in their electronic structures, the observed overpotentials

are rather similar and trends are well reproduced by our computational studies. This is very relevant for at least two reasons: (1) Co^{II}POMs have shown excellent OER activity under strong acidic conditions; (2) given the questioned stability of POMs under electrocatalytic conditions and the complexity of the reaction mechanisms, the agreement between experimental and theoretical observations reinforces both experimental characterizations and theoretical studies. The current results strongly suggest that Fe^{III}-POMs are stable under heterogeneous electrocatalytic conditions and active as OER catalysts. With these promising results, our groups are currently working to show that Fe^{III}-POMs can be active and stable in acidic conditions.

3.4. Experimental section

3.4.1. Polyoxometalate synthesis

$[Fe_4(H_2O)_2(PW_9O_{34})_2]^{6-}$ ($Fe_4P_2W_{18}$):

About 1.43 of $FeSO_4.7H_2O$ (Fluka puriss. p.a. > 99.5%, 278.02 $g.mol^{-1}$, 5.1 mmol) was dissolved in 25 mL of water. Then 6.0 g of $Na_9PW_9O_{34}.11H_2O$ (A-β isomer, M.W. 2634.59 $g.mol^{-1}$, 2.3 mmol) are added in small portions under stirring and heating (60°C). After 20 minutes of evolution, the dark brown solution is hot-filtered, and the clear filtrate treated with 7.5 g of solid KCl. A light brown precipitate starts to appear after a few minutes. The preparation is kept in the refrigerator overnight. After about 12 hours of this stay at 4°C, the light brown solid is collected and dissolved in 30 mL and then heat for about 4 hours at 80°C under stirring. After filtration and cooling at room temperature, the dark yellow solution is transferred into the refrigerator, in order to promote precipitation of the compound of interest. The yellow crystalline powder that forms is recovered by filtration after a few days and dried in the open air. We obtain 4.21 g of $K_6[Fe_4(PW_9O_{34})_2].20H_2O$.

Ba-$Fe_4P_2W_{18}$ salts were obtained by metathesis of a **K-$Fe_4P_2W_{18}$** aqueous solution upon addition of an excess of $BaCl_2$, which immediately yields the desired precipitate. The **Ba-$Fe_4P_2W_{18}$** precipitate was filtered, cleaned with water and acetone and dried in air.

The FT-IR and RAMAN data for the K and Ba salts are summarized in figure 3.17. POM composition was confirmed by EDX, water content was determined by thermogravimetric analysis (TGA) (Figure 3.18) and counter cation content was determined by elemental analysis.

$K_6[Fe_4(H_2O)_2(PW_9O_{34})_2]\cdot 20H_2O$ **K-$Fe_4P_2W_{18}$** M_w=5492.29 g/mol. Elemental analysis calculated: K, 6 Found (%): K, 6.3; $Ba_3[Fe_4(H_2O)_2(PW_9O_{34})_2]\cdot 39H_2O$ **Ba-$Fe_4P_2W_{18}$** M_w=5838.54 g/mol. Elemental analysis calculated (%): Ba, 3 Found (%): Ba, 3.4.

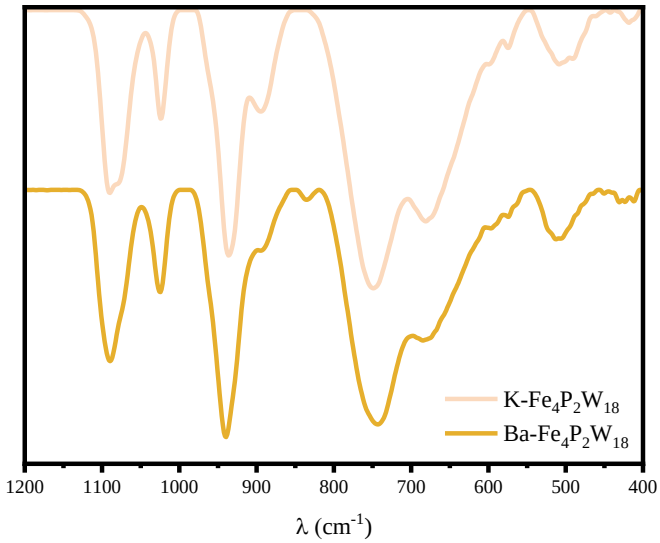

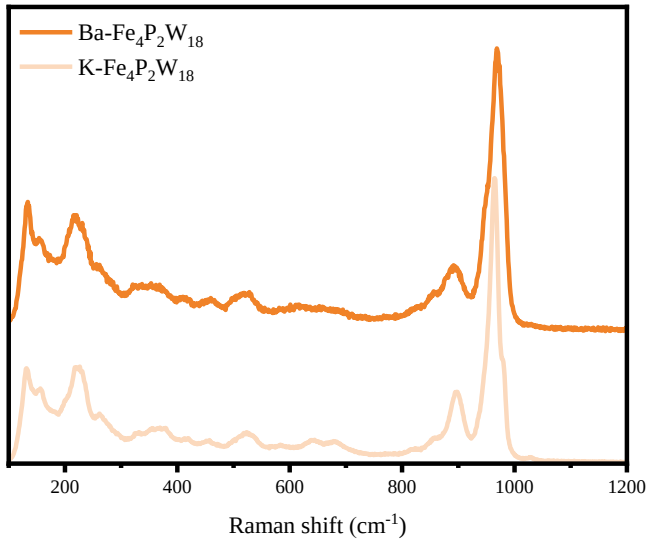

Figure 3.17. (Top) FT-IR (Bottom) Raman spectra of [Fe4(H2O)2(PW9O34)2]$^{6-}$ (**$Fe_4P_2W_{18}$**) with different countercations: K+ (**K- $Fe_4P_2W_{18}$**) (light) and Ba2+ (**Ba- $Fe_4P_2W_{18}$**) (bold).

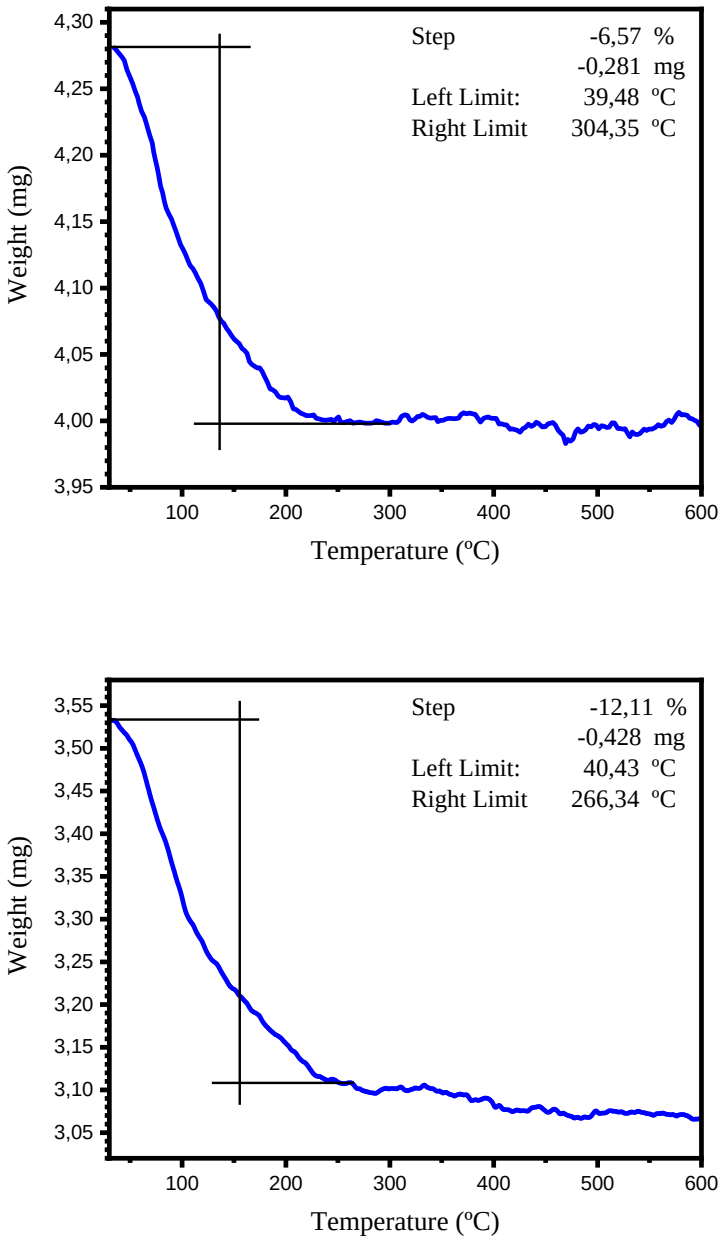

Figure 3.18. Thermogravimetric analysis for **K- $Fe_4P_2W_{18}$** (Bottom) and **Ba- $Fe_4P_2W_{18}$** (Top).

$[Fe(H_2O)(PW_{11}O_{39})]^{4-}$ ($FePW_{11}$):

Solid $Fe(NO_3)_3 \cdot 9H_2O$ (230 mg) was added to 6 mL of a hot (90ºC) distillated water solution containing 1.73 g of $K_7PW_{11}O_{39} \cdot H_2O$ under continuous stirring and kept at that temperature for 10 minutes... Then, the solution was filtered using a Nylon membrane filter. To the cooled filtrated solution 10 ml of a Tetra-n-butylammonium bromide (260 mg) aqueous solution were gradually added under stirring. The **TBA- $FePW_{11}$** salt precipitates immediately, which did not contain any potassium cations.

Ba- $FePW_{11}$ salts were obtained by metathesis of a **TBA- $FePW_{11}$** acetonitrile solution upon addition of an excess of $BaCl_2$, which immediately yields the desired precipitate. The **Ba- $FePW_{11}$** precipitate was filtered, cleaned with water and acetone and dried in air.

The FT-IR and RAMAN data for the K and Ba salts are summarized in figure 3.19. POM composition was confirmed by EDX, water content was determined by thermogravimetric analysis (TGA) (Figure 3.20) and counter cation content was determined by elemental analysis.

$TBA_4[Fe(H_2O)(PW_{11}O_{39})] \cdot 3H_2O$ (**TBA-$FePW_{11}$**) M_w=3784.49 g/mol. $Ba_2[Fe(H_2O)(PW_{11}O_{39})] \cdot 7H_2O$ **Ba-$FePW_{11}$** M_w=3566.32 g/mol. Elemental analysis calculated (%): Ba, 2 Found (%): Ba, 2.1

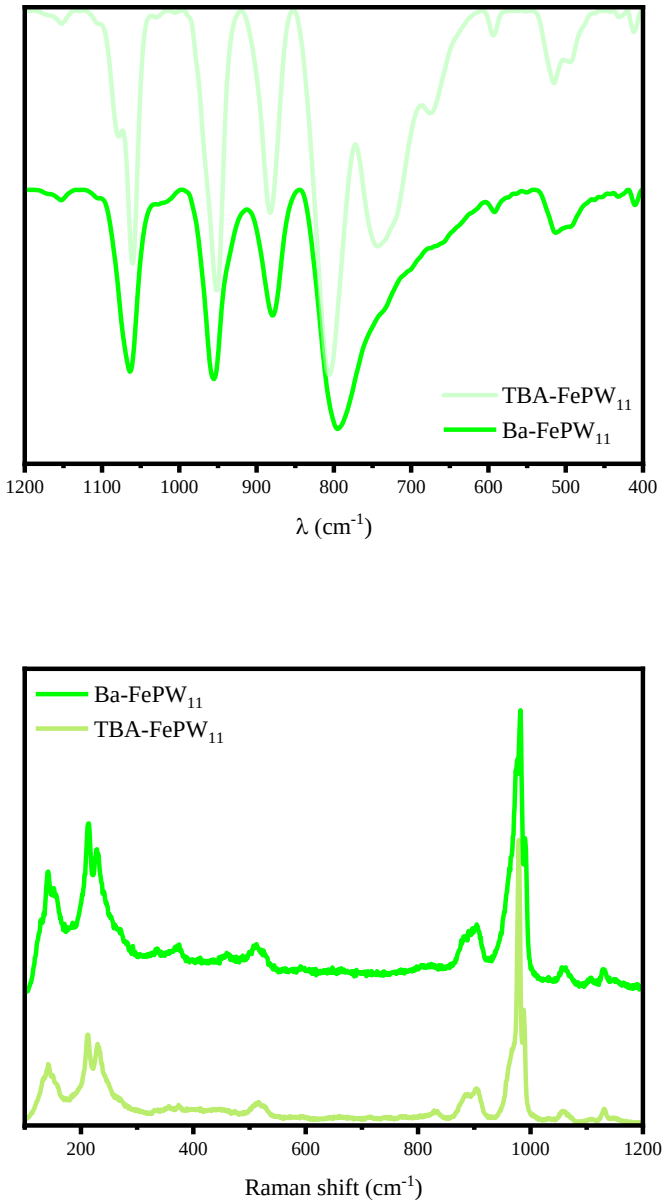

Figure 3.19. (Top) FT-IR (Bottom) Raman spectra of $[Fe_4(H_2O)_2(PW_9O_{34})_2]^{6-}$ (**$Fe_4P_2W_{18}$**) with different countercations: K+ (**K- $Fe_4P_2W_{18}$**) (light) and Ba2+ (**Ba- $Fe_4P_2W_{18}$**) (bold).

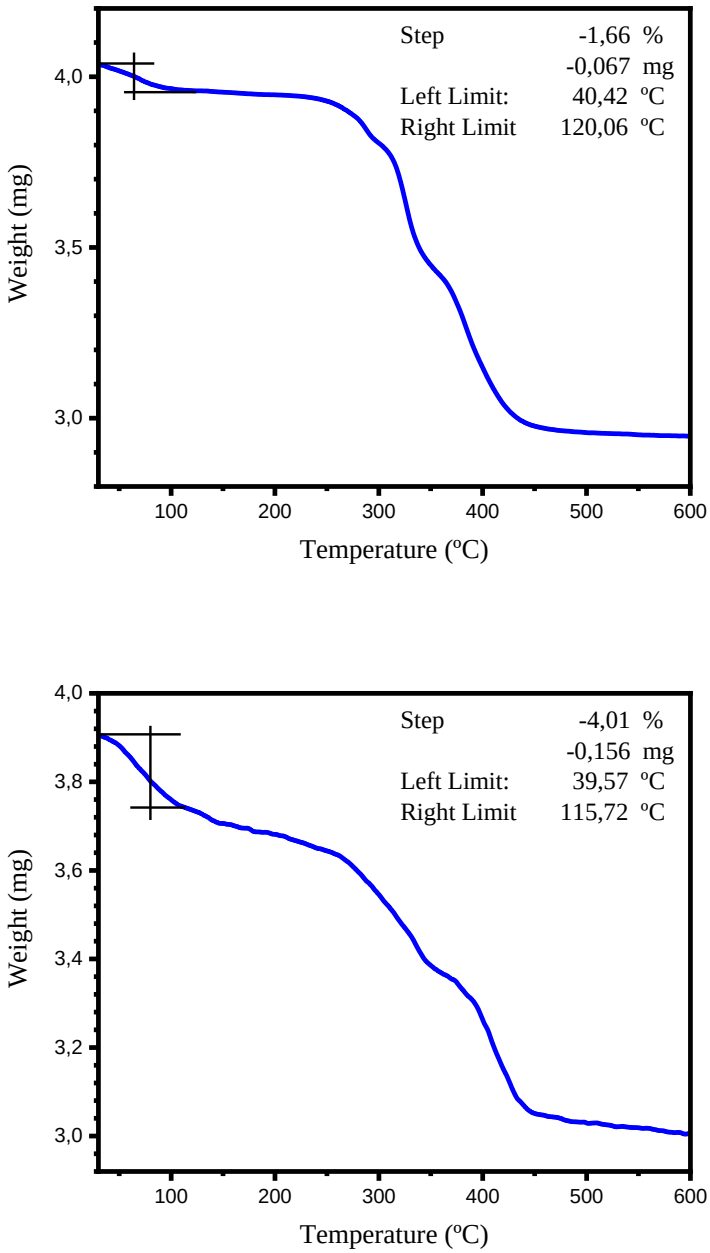

Figure 3.20. Thermogravimetric analysis for TBA-**$FePW_{11}$** (Top) and Ba-**$FePW_{11}$** (Bottom).

3.4.2. Characterization methods

All the POMs were characterized by thermogravimetric analysis (TGA), infrared spectroscopy, Raman spectroscopy and energy dispersive Xray spectroscopy (EDX). Thermogravimetric analysis (TGA) was performed under N2 flow with powder samples using a TGA/SDTA851 Mettler Toledo with a MT1 microbalance. The experiments were carried out by weighing about 3 mg of sample in an Al-crucible of 40 mL and with a temperature scan range from 30 ºC to 600 ºC at a heating rate of 10 ºCmin^{-1}. IR spectra were collected with a FT-IR Bruker spectrometer model Alpha equipped with an ATR accessory. The spectra were acquired in the range 400–4000 cm^{-1} with 32 scans Raman measurements were acquired using a Renishaw in Via Reflex Raman confocal microscope (Gloucester-Shire, UK), equipped with a diode laser emitting at 785 nm at a nominal power of 300 mW, and a Peltier-cooled CCD detector (-70 ºC) coupled to a Leica DM2500 microscope. Calibration was carried out daily by recording the Raman spectrum of an internal Si standard. Rayleigh scattered light was appropriately rejected by using edge-type filters. The spectra were acquired in the range 100–1800 cm^{-1}. Laser power was used at nominal 1% to avoid sample damage. Spectra were recorded with the accumulation of at least 3 scans with a 30 s scan time. Cation content was determined by energy-dispersive X-ray spectroscopy (EDX), which was collected with a JEOL-JMS6400 environmental scanning electron microscope equipped with an Oxford Instruments X-ray elemental analyzer. The sample was adhered on a carbon tape using Al-stubs as a support. Before measurements, the sample

was cleaned with an airflow to remove non-attached compound. The measurements were performed under low-vacuum conditions with a Large-Field Detector at 20 kV using a probe current of 17 pA. Quantification of metal leached into the buffer solution was carried out with an Inductively Coupled Plasma Quadrupolar Mass Spectrometer (ICP-MS) (Thermo, iCAP Qc, Xt interphase and PFA micronebulizer) at the University of Valencia. Elemental analysis was carried out with an Agilent 725-ES inductively coupled plasma optical emission spectrometer (ICP-OES) at the University of Valladolid, taking the following standards: Ba (455.403nm), Cs (697.327 nm), W

(207.912 nm), Co (238.892 nm), P (213.618 nm) and Si (250.690 nm). The digestion of the POM was carried out by dissolving 10 mg of POM in 10 mL of acidic solution (concentrated HNO3, concentrated HCl).

3.4.3. Electrochemical details

All electrochemical experiments were performed using a Biologic SP150 potentiostat. Ohmic drop was compensated using the positive feedback compensation implemented in the instrument. All experiments were performed with a three-electrode configuration using the CP electrode as a working electrode, whereas a Saturated Calomel Electrode (SCE) and a Pt mesh were used as a reference and counter electrodes, respectively. Linear sweep voltammetry experiments (LSV) were performed using an ALS RRDE-3A set-up, with a CP Rotating Disk Electrode (RDE, surface area = 0.07 cm^2) at 1600 rpm and at scan rate of 1 mV s^{-1}. Bulk water electrolysis was performed at a constant current density of 1 mA cm_2 for 20 h. All current densities were calculated based on the geometrical surface area of the electrodes (0.07 cm2). The experiments were carried out in an aqueous potassium phosphate (50 mM) buffer solution containing KNO3 (1 M) as the electrolyte at pH = 6.9. The thermodynamic potential for the water oxidation was corrected by the pH value using the Nernst equation:

$$E^{o}_{H_2O|O_2} = 1.229 - 0.059pH\ vs\ NHE\ at\ 25^{o}C$$

All potentials were converted to the NHE reference scale using ENHE ¼ ESCE + 0.241 (V). The water oxidation overpotentials (h) were calculated by subtracting the thermodynamic water oxidation potential to the applied potential:

$$\eta = E_{app} - H2O_{H_2O|O_2}$$

3.4.3.1. Electrode preparation

The CP blends were prepared by mixing the barium salts of the POMs with CP in the desired weight ratios using an agate mortar. Then, the blend was introduced into the CP electrode pocket. A small piece of staple cotton was used to cover the electrode surface

for long-term electrocatalytic experiments to avoid the expulsion of the blend out of the electrode pocket.

3.4.3.2. Oxygen evolution

The oxygen evolved was measured using an Ocean Optics Neo-FOX oxygen sensing system equipped with a FOXY probe. The FOXY probe was calibrated employing a two-point calibration, taking (a) 0% of O_2 determined under a N_2 flow and (b) 20.9% of O_2 measured in the air. The experiments were carried out in an H-cell, with the anode and cathode compartments peparated by a porous frit. The FOXY probe was inserted into the gas space of the anodic compartment ($V_{Gas\ space} \approx 21$ mL). The solution was completely deaerated by purging with N2 for at least 1 h. The N_2 flow was then removed and a base line of 30 min was recorded before starting the chronopotentiometry at a constant current density of 1 mA cm^{-2}. The O_2 generated during the electrochemical experiment was expressed as the partial pressure of O_2. The number of moles of oxygen produced were calculated using the Ideal Gas Law as: $n_{O_2} = \frac{P_{O_2} V_{gs}}{RT}$

where P_{O2} (atm) is the measured partial pressure of O_2, Vgs (L) is the volume of the gas space, R = 0.082 (atm L/K mol) is the ideal gas law constant and T = 298 K is the temperature. The theoretical amount of O_2 produced was calculated from the number of charges passed through the working electrode during the chronopotentiometry experiment as: $n_{O_2}(theor) = \frac{Q}{\nu_e F}$

where Q (C) is the charge passed through the system, $\nu_e = 4$ is the number of electrons needed to generate one molecule of O_2 and F is the Faraday constant (96 485 $C \cdot mol^{-1}$).

3.4.3.3. Catalyst recovery

After the electrochemical experiments, the Ba[POM]/CP blend (ca. 40 mg) was suspended in acetone (30 mL) and sonicated for 30 minutes. The supernatant liquid (containing carbon black and the organic oil binder) was decanted to retain the POM catalyst in the beaker. This procedure was repeated 10 times to get a clean catalyst sample, ready for post-catalytic characterization.

3.5. Computational section

The calculations were performed using the Gaussian-16 package.[60] The B3LYP functional[61–63] was chosen based on the successful results obtained for similar systems.[40] We used two types of basis set combinations, herein BS1 and BS2. BS1 is a combination of small basis sets firstly used to explore in detail the potential energy surface of the computed POMs. In BS1, we used the 6-31G(d,p) basis set for all the H and O atoms directly bonded to either the iron or the cobalt atoms and the 6-31G basis set for the rest of the oxygens.[64–66] In the BS2 combination, the 6-31G(d,p) basis set was used for all the oxygens to re-optimize all the relevant structures. In both methods, the LANL2DZ effective core potential (ECP) and associated basis sets were used for the P, W, Co and Fe atoms.[67] All the structures were optimized using the IEF-PCM approach to model implicitly the solvent effects of water (ε = 78.36 and UFF radii).[68] We tested Grimme's dispersion corrections GD2,[69] GD3[70] and GD3BJ[71] to our calculations. However, these calculations lead to a poor reproduction of the experimentally observed pKa's, while the combination of the B3LYP functional with BS2 yielded results in close agreement with the experimental values. The nature of all the stationary points was verified by computation of the vibrational frequencies. All the energies reported correspond to the computed free Gibbs energies in solution; electrochemical steps are reported either in V or eV, and chemical steps in eV and kcal mol^{-1}. All the experimental and computed potentials and overpotentials given in the present work are referred to the NHE reference scale. A collection data set of all computational data is accessible in the ioChem-BD repository and may be accessed via https://doi.org/10.19061/iochem-bd-2-48. [72]

3.6. References

[1] N. S. Lewis, D. G. Nocera, *Proc. Natl. Acad. Sci.* **2006**, *103*, 15729.

[2] W. Steffen, K. Richardson, J. Rockstrom, S. E. Cornell, I. Fetzer, E. M. Bennett, R. Biggs, S. R. Carpenter, W. de Vries, C. A. de Wit, C. Folke, D. Gerten, J. Heinke, G. M. Mace, L. M. Persson, V. Ramanathan, B. Reyers, S. Sorlin, *Science (80-.).* **2015**, *347*, 1259855.

[3] J. R. McKone, N. S. Lewis, H. B. Gray, *Chem. Mater.* **2014**, *26*, 407.

[4] D. G. Nocera, *Acc. Chem. Res.* **2012**, *45*, 767.

[5] J. R. Galán-Mascarós, *Catal. Sci. Technol.* **2020**, *10*, 1967.

[6] S. A. Sherif, F. Barbir, T. N. Veziroglu, *Sol. Energy* **2005**, *78*, 647.

[7] K. Mazloomi, C. Gomes, *Renew. Sustain. Energy Rev.* **2012**, *16*, 3024.

[8] C. C. L. McCrory, S. Jung, I. M. Ferrer, S. M. Chatman, J. C. Peters, T. F. Jaramillo, *J. Am. Chem. Soc.* **2015**, *137*, 4347.

[9] R. L. D. and M. E. G. Lyons, *Photoelectrochemical Solar Fuel Production: From Basic Principles to Advanced Devices*, Springer International Publishing, Cham, **2016**.

[10] J. Soriano-López, W. Schmitt, M. García-Melchor, *Curr. Opin. Electrochem.* **2018**, *7*, 22.

[11] L. Duan, F. Bozoglian, S. Mandal, B. Stewart, T. Privalov, A. Llobet, L. Sun, *Nat. Chem.* **2012**, *4*, 418.

[12] L. C. Seitz, C. F. Dickens, K. Nishio, Y. Hikita, J. Montoya, A. Doyle, C. Kirk, A. Vojvodic, H. Y. Hwang, J. K. Norskov, T. F. Jaramillo, **2016**, *353*.

[13] J. R. Galán-Mascarós, *ChemElectroChem* **2015**, *2*, 37.

[14] I. Roger, M. A. Shipman, M. D. Symes, *Nat. Rev. Chem.* **2017**, *1*, 0003.

[15] J. D. Blakemore, R. H. Crabtree, G. W. Brudvig, *Chem. Rev.* **2015**, *115*, 12974.

[16] M. W. Kanan, D. G. Nocera, *Science (80-.).* **2008**, *321*, 1072.

[17] A. J. Esswein, Y. Surendranath, S. Y. Reece, D. G. Nocera, *Energy Environ. Sci.* **2011**, *4*, 499.

[18] H. Lv, Y. V Geletii, C. Zhao, J. W. Vickers, G. Zhu, Z. Luo, J. Song, T. Lian, D. G. Musaev, C. L. Hill, *Chem. Soc. Rev.* **2012**, *41*, 7572.

[19] D. Gao, I. Trentin, L. Schwiedrzik, L. González, C. Streb, *Molecules* **2020**, *25*, 1.

[20] S. Goberna-Ferrón, J. Soriano-López, J. R. Galán-Mascarós, M. Nyman, *Eur. J. Inorg. Chem.* **2015**, *2015*, 2833.

[21] Y. V. Geletii, B. Botar, P. Kögerler, D. A. Hillesheim, D. G. Musaev, C. L. Hill, *Angew. Chemie Int. Ed.* **2008**, *47*, 3896.

[22] A. Sartorel, M. Carraro, G. Scorrano, R. De Zorzi, S. Geremia, N. D. McDaniel, S. Bernhard, M. Bonchio, *J. Am. Chem. Soc.* **2008**, *130*, 5006.

[23] Q. Yin, J. M. Tan, C. Besson, Y. V Geletii, D. G. Musaev, A. E. Kuznetsov, Z. Luo, K. I. Hardcastle, C. L. Hill, *Science (80-.).* **2010**, *328*, 342 LP.

[24] T. J. R. Weakley, H. T. Evans, J. S. Showell, G. F. Tourné, C. M. Tourné, *J. Chem. Soc., Chem. Commun.* **1973**, *139*, 140.

[25] S. Goberna-Ferrón, L. Vigara, J. Soriano-López, J. R. Galán-Mascarós, *Inorg. Chem.* **2012**, *51*, 11707.

[26] J. Soriano-López, S. Goberna-Ferrón, L. Vigara, J. J. Carbó, J. M. Poblet, J. R. Galán-Mascarós, *Inorg. Chem.* **2013**, *52*, 4753.

[27] M. Blasco-Ahicart, J. Soriano-López, J. J. Carbó, J. M. Poblet, J. R. Galan-Mascaros, *Nat. Chem.* **2017**, *10*, 24.

[28] S. Enthaler, K. Junge, M. Beller, *Angew. Chemie Int. Ed.* **2008**, *47*, 3317.

[29] C. Casadevall, A. Bucci, M. Costas, J. Lloret-fillol, *Water oxidation catalysis with well-defined molecular iron complexes*, 1st ed., Vol. 74, Elsevier Inc., **2019**.

[30] F. Müh, A. Zouni, *Photosynth. Res.* **2013**, *116*, 295.

[31] H. Bandal, K. K. Reddy, A. Chaugule, H. Kim, *J. Power Sources* **2018**, *395*, 106.

[32] P. T. Babar, B. S. Pawar, A. C. Lokhande, M. G. Gang, J. S. Jang, M. P. Suryawanshi, S. M. Pawar, J. H. Kim, *J. Energy Chem.* **2017**, *26*, 757.

[33] Y. Yan, B. Zhao, S. C. Yi, X. Wang, *J. Mater. Chem. A* **2016**, *4*, 13005.

[34] D. Zhong, L. Liu, D. Li, C. Wei, Q. Wang, G. Hao, Q. Zhao, J. Li, *J. Mater. Chem. A* **2017**, *5*, 18627.

[35] B. Zhang, X. Zheng, O. Voznyy, R. Comin, M. Bajdich, M. Garcia-Melchor, L. Han, J. Xu, M. Liu, L. Zheng, F. P. Garcia de Arquer, C. T. Dinh, F. Fan, M. Yuan, E. Yassitepe, N. Chen, T. Regier, P. Liu, Y. Li, P. De Luna, A. Janmohamed, H. L. Xin, H. Yang, A. Vojvodic, E. H. Sargent, *Science (80-.).* **2016**, *352*, 333.

[36] L. Trotochaud, S. L. Young, J. K. Ranney, S. W. Boettcher, *J. Am. Chem. Soc.* **2014**, *136*, 6744.

[37] M. Zheng, Y. Ding, X. Cao, T. Tian, J. Lin, *Appl. Catal. B Environ.* **2018**, *237*, 1091.

[38] X. Du, Y. Ding, F. Song, B. Ma, J. Zhao, J. Song, *Chem. Commun.* **2015**, *51*, 13925.

[39] M. Zheng, X. Cao, Y. Ding, T. Tian, J. Lin, *J. Catal.* **2018**, *363*, 109.

[40] J. Soriano-López, D. G. Musaev, C. L. Hill, J. R. Galán-Mascarós, J. J. Carbó, J. M. Poblet, *J. Catal.* **2017**, *350*, 56.

[41] X. Zhang, Q. Chen, D. C. Duncan, R. J. Lachicotte, C. L. Hill, *Inorg. Chem.* **1997**, *36*, 4381.

[42] N. Vilà, P. A. Aparicio, F. Sécheresse, J. M. Poblet, X. López, I. M. Mbomekallé, *Inorg. Chem.* **2012**, *51*, 6129.

[43] I. M. Mbomekalle, B. Keita, L. Nadjo, P. Berthet, K. I. Hardcastle, C. L. Hill, T. M. Anderson, *Inorg. Chem.* **2003**, *42*, 1163.

[44] C. S. A. Mezui, P. de Oliveira, A.-L. Teillout, J. Marrot, P. Berthet, M. Lebrini, I. M. Mbomekallé, *Inorg. Chem.* **2017**, *56*, 1999.

[45] S. Romo, J. A. Fernández, J. M. Maestre, B. Keita, L. Nadjo, C. de Graaf, J. M. Poblet, *Inorg. Chem.* **2007**, *46*, 4022.

[46] J. T. Arens, M. Blasco-ahicart, K. Azmani, J. Soriano-lópez, A. García-eguizábal, J. M. Poblet, *J. Catal.* **2020**, *389*, 345.

[47] A. G. MacDiarmid, *Inorganic Syntheses* (Ed.: Inorganic Syntheses, I.), Vol. 17, **2007**.

[48] Z. W. Seh, J. Kibsgaard, C. F. Dickens, I. Chorkendorff, J. K. Nørskov, T. F. Jaramillo, *Science (80-.).* **2017**, *355*.

[49] M. Martin-Sabi, J. Soriano-López, R. S. Winter, J.-J. Chen, L. Vilà-Nadal, D.-L. Long, J. R. Galán-Mascarós, L. Cronin, *Nat. Catal.* **2018**, *1*, 208.

[50] M. N. Kushner-Lenhoff, J. D. Blakemore, N. D. Schley, R. H. Crabtree, G. W. Brudvig, *Dalt. Trans.* **2013**, *42*, 3617.

[51] C. A. Ohlin, S. J. Harley, J. G. McAlpin, R. K. Hocking, B. Q. Mercado, R. L. Johnson, E. M. Villa, M. K. Fidler, M. M. Olmstead, L. Spiccia, R. D. Britt, W. H. Casey, *Chem. – A Eur. J.* **2011**, *17*, 4408.

[52] D. Lieb, A. Zahl, E. F. Wilson, C. Streb, L. C. Nye, K. Meyer, I. Ivanović-Burmazović, *Inorg. Chem.* **2011**, *50*, 9053.

[53] S. M. Kanowitz, G. J. Palenik, *Inorg. Chem.* **1998**, *37*, 2086.

[54] M. Zheng, X. Cao, Y. Ding, T. Tian, J. Lin, *J. Catal.* **2018**, *363*, 109.

[55] S. Piccinin, A. Sartorel, G. Aquilanti, A. Goldoni, M. Bonchio, S. Fabris, **2013**, *110*, 1.

[56] V. A. Online, H. Lei, A. Han, F. Li, M. Zhang, Y. Han, P. Du, W. Lai, R. Cao, **2014**, 1883.

[57] L. Vigara, M. Z. Ertem, N. Planas, F. Bozoglian, N. Leidel, H. Dau, M. Haumann, L. Gagliardi, C. J. Cramer, A. Llobet, *Chem. Sci.* **2012**, *3*, 2576.

[58] W. Lai, R. Cao, G. Dong, S. Shaik, J. Yao, H. Chen, *J. Phys. Chem. Lett.* **2012**, *3*, 2315.

[59] J. Lloret-fillol, M. Costas, *Water oxidation at base metal molecular catalysts*, 1st ed., Vol. 71, Elsevier Inc., **2019**.

[60] M. J. Frisch, G. W. Trucks, H. B. Schlegel, G. E. Scuseria, M. a. Robb, J. R. Cheeseman, G. Scalmani, V. Barone, G. a. Petersson, H. Nakatsuji, X. Li, M. Caricato, a. V. Marenich, J. Bloino, B. G. Janesko, R. Gomperts, B. Mennucci, H. P. Hratchian, J. V. Ortiz, a. F. Izmaylov, J. L. Sonnenberg, Williams, F. Ding, F. Lipparini, F. Egidi, J. Goings, B. Peng, A. Petrone, T. Henderson, D. Ranasinghe, V. G. Zakrzewski, J. Gao, N. Rega, G. Zheng, W. Liang, M. Hada, M. Ehara, K. Toyota, R. Fukuda, J. Hasegawa, M. Ishida, T. Nakajima, Y. Honda, O. Kitao, H. Nakai, T. Vreven, K. Throssell, J. a. Montgomery Jr., J. E. Peralta, F. Ogliaro, M. J. Bearpark, J. J. Heyd, E. N. Brothers, K. N. Kudin, V. N. Staroverov, T. a. Keith, R. Kobayashi, J. Normand, K. Raghavachari, a. P. Rendell, J. C. Burant, S. S. Iyengar, J. Tomasi, M. Cossi, J. M. Millam, M. Klene, C. Adamo, R. Cammi, J. W. Ochterski, R. L. Martin, K. Morokuma, O. Farkas, J. B. Foresman, D. J. Fox, *G16_C01*, **2016**, p. Gaussian 16, Revision C.01, Gaussian, Inc., Wallin.

[61] C. Lee, W. Yang, R. G. Parr, *Phys. Rev. B* **1988**, *37*, 785.

[62] A. D. Becke, *J. Chem. Phys.* **1992**, *96*, 2155.

[63] P. J. Stephens, F. J. Devlin, C. F. Chabalowski, M. J. Frisch, *J. Phys. Chem.* **1994**, *98*, 11623.

[64] M. M. Francl, W. J. Pietro, W. J. Hehre, J. S. Binkley, M. S. Gordon, D. J. DeFrees, J. A. Pople, *J. Chem. Phys.* **1982**, *77*, 3654.

[65] W. J. Hehre, K. Ditchfield, J. A. Pople, *J. Chem. Phys.* **1972**, *56*, 2257.

[66] P. C. Hariharan, J. A. Pople, *Theor. Chim. Acta* **1973**, *28*, 213.

[67] P. J. Hay, W. R. Wadt, *J. Chem. Phys.* **1985**, *82*, 270.

[68] E. Cancès, B. Mennucci, J. Tomasi, *J. Chem. Phys.* **1997**, *107*, 3032.

[69] S. Grimme, S. Ehrlich, L. Goerigk, *J. Comput. Chem.* **2011**, *32*, 1456.

[70] S. Grimme, J. Antony, S. Ehrlich, H. Krieg, *J. Chem. Phys.* **2010**, *132*, 154104.

[71] S. Grimme, *J. Comput. Chem.* **2006**, *27*, 1787.

[72] M. Álvarez-Moreno, C. de Graaf, N. López, F. Maseras, J. M. Poblet, C. Bo, *J. Chem. Inf. Model.* **2015**, *55*, 95.

Chapter 4

Water oxidation electrocatalysis in acidic media with Fe-containing Polyoxometalates

4.1. Introduction

Storage energy is indeed the key point to emerge the use of renewable energy source (i.e solar energy) and make it competitive to reach the carbon independency. The clean and efficient strategy to store this intermittent energy is its conversion into chemical bonds. Hydrogen is the most promising candidate, owing to its high energy density and carbon-free features. Thus, water is nowadays the promising fuel to store electrical energy into chemical bond by splitting water in H_2 and O_2. This is known as green hydrogen because hydrogen is obtained from free carbon source. The researcher's challenge is to reduce the electrochemical cost of the process. This is mainly focused to find cost-effective earth-abundant, efficient, and robust catalyst to reduce the required overpotential.

As explained in the introducing chapter, in the water splitting process two semireactions take place: the oxidation of water to molecular oxygen (OER) and the reduction of protons to molecular hydrogen (HER). The thermodynamic potential of both semireactions is pH dependent and the water oxidation reaction is generally considered as the bottleneck of the whole process.

Huge findings confirm viable, low-cost, and promising catalysts for the hydrogen evolution reaction.[1–4] However, this are focused mainly on alkaline media. Acidic solutions would be preferred as media to perform water splitting. Hydrogen production is much easier at lower pH, where the high proton concentration, and proton exchange membranes are able to support high currents minimizing crossover and resistance loses.[5,6] However, the catalysts used must survive under such demanding conditions and, up to now, only noble scarce materials are capable to do it, such as those based on iridium and ruthenium.[7]

The most promising electrolysis device to perform water splitting in a commercial scale is based on solid polymer electrolyte membrane technology (PEM-electrolyser). This device can operate at high current densities (~2 A/cm^2) thanks to the presence of a very thin electrolyte membrane with a high proton conductivity (0.1 ± 0.02 $S\cdot cm^{-1}$) and minimum ohmic losses. Moreover, there is low gas crossover rate through the polymer electrolyte membrane, yielding hydrogen with high purity and allowing the system to

work under a wide range of power input. Nevertheless, there are some negative aspects that minimise the implementation of these compact devices in the market, which are directly related to the corrosive acidic regime provided by the proton exchange membrane.

Clever strategies have been reported along last decades to stabilize earth abundant based catalyst in acidic media to compete with IrO_2. Unfortunately, all shows non efficient performance. However, cobalt based polyoxometalates (Co-POM) shows to be the promising bridge to achieve the transition from noble to earth-abundant metals.[8–11] Specially, in 2017, Galán-Mascarós et al reported excellent catalytic activity of water-insoluble $[Co_9(H2O)_6(OH)_3(HPO_4)_2(PW_9O_{34})_3]^{16-}$ salts in acidic media, known as Co9.[12] Modified electrodes incorporating barium salts of Co_9 in carbon paste matrix promote OER during water electrolysis experiments, with superior performance to the state-of-the-art IrO_2 in sulfuric acid solution (1 M).[12]

Furthermore, it is important to highlight the genuine role of the carbon paste. The better reported performance of the Co-POM in comparison with IrO_2 can be provided in some way by the matching between the catalyst with the support. Indeed, an overall hydrophobic environment is known to enhance POM redox activity and stability. Galán-Mascarós et al have observed a better performance of some metal oxide when this is introduced in carbon paste matrix.[12,13] In other words, insulating hydrocarbon binder and an appropriate conducting support helps afford the extreme acidic conditions making viable the oxygen evolution reaction.

Motivated by its abundancy and innocuous character, iron becomes a promising transition metal to be explored as water oxidation catalyst. Water oxidation catalysts based on mononuclear iron complexes have been explored but they often deactivate rapidly and exhibit relatively low activities. Recently, Masaoka et al. have reported pentanuclear iron complex with formula $[Fe^{II}_4Fe^{III}(\mu_3\text{-}O)(\mu\text{-}L)_6]^{3+}$ (1; LH=3,5-bis(2-pyridyl)pyrazole) showing remarkable performance and robustness in an acetonitrile/water (10:1) mixed solution with Et_4NClO_4 (0.1M).[14] Our group has reported last year as is well described in the previous chapter, Fe-POM with a promising

feature as WOC.[15] $Fe_4P_2W_{18}$ are stable under heterogeneous electrocatalytic conditions and active as OER catalysts. The similar performance observed at neutral pH in comparison with the analogous Co-POM motivate us to evaluate the performance of $Fe_4P_2W_{18}$ in acidic conditions.

In this chapter, we present the water oxidation catalytic activity of $Fe_4P_2W_{18}$ in same conditions as Ba-Co_9. We have carried out our catalytic study in the solid-state using the POM water-insoluble barium salt to assure structural stability. We have evaluated the stability in order to confirm its resistance in a strongly acidic condition. In addition, we measured the catalytic efficiency measuring the faradaic efficiency.

4.2. Results and Discussion

Due to the high level of interest in acid water oxidation catalysis, we have decided to evaluate the activity of the insoluble salt of $Fe_4P_2W_{18}$ obtained by the addition of $BaCl_2$ to $Fe_4P_2W_{18}$ water solution described and characterized in the previous chapter. The water-insoluble salt was blended with commercial carbon paste to obtain modified anodes. To put in context our results, we carried out experiments using the same experiment conditions with the cobalt analog $Fe_4P_2W_{18}$ and IrO_2. Furthermore, extra experiments were carried out using iron-based metal oxides to confirm the true catalytic activity.

Three-electrode configuration was used to study the catalytic performance in strong acidic media of 1M H_2SO_4. In our case we have used Pt mesh as the counter-electrode and a Saturated Calomel Electrode (SCE) as the reference electrode. The catalyst content in conductive carbon matrix was fixed up to 30% to compare with the reported values of the unprecedent nonacobalt(II) Polyoxometalate Co_9.

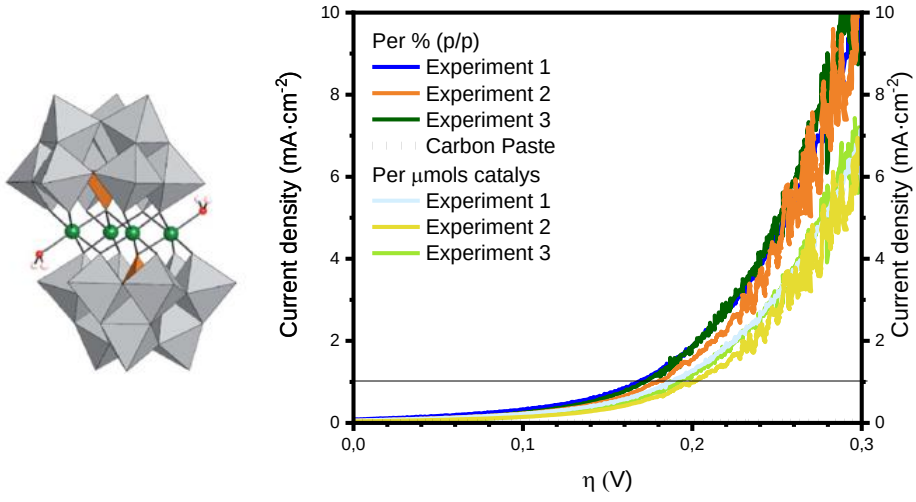

Figure 4.1. a. Molecular structure of the $[(Fe^{III}OH_2)_2Fe^{III}_2(PW_9O_{34})_2]^{6-}$ b. Repetitive linear sweep voltammetry for 20% blend working electrodes at 1M H_2SO_4 c. Linear sweep voltammetry for different weigh ratio blend working electrodes at 1M H2SO4 normalized by the total number of moles.

To evaluate the reproducibility of the performance, we have tested three independent working electrodes with 20% catalyst content. The experimental results by means of multiple Linear Sweep Voltammetry show an identical activity (Figure 5.1.b). Furthermore, electrocatalytic activity of Ba-$Fe_4P_2W_{18}$/CP electrodes involves a significant current density in comparison with catalyst-free CP electrode. To our surprise, Ba-$Fe_4P_2W_{18}$/CP showed a comparable performance in comparison with the reported Ba-Co_9/CP at 20%. The overpotential difference corresponding at 1mA·cm^{-2} current density is 10mV.

The optimal catalyst content for Co-POMs to get an optimum activity was blends at 30-40% content (in weight). Taking this into account we have performed an optimization of the catalyst content for Ba-$Fe_4P_2W_{18}$/CP (Figure 4.2). The results show a maximum catalyst content of 20% for the Ba-$Fe_4P_2W_{18}$/CP. Blends with higher blend content became too brittle for accurate measurements giving unreal information after the current density is normalized by the number of mols of catalyst.

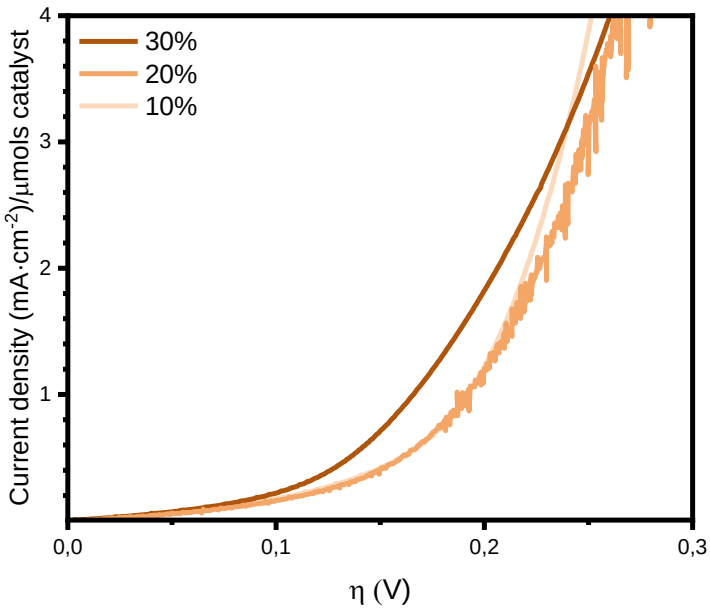

Figure 4.2. Linear sweep voltammetry normalized by the total number of moles of a series % (w/w) Ba-$Fe_4P_2W_{18}$/CP working electrodes. All the measurements were done in 1M H2SO4M at pH = 0.

To put our catalyst results in context, we carried out electrochemical study of Ba-$Co_4P_2W_{18}$/CP, IrO_2 and some iron-based metal oxides like $Ni_{0.9}Fe_{0.1}O_x$ (NiFe) and Fe_2O_3 using the same working conditions excepting the catalyst content, which is defined to be 30%. The not treated LSV results show the exceed performance of Ba-$Fe_4P_2W_{18}$/CP in comparison with rest of catalyst. The comparison with the Co-based POM makes Iron the new gold mine for water-splitting technology. Furthermore, the Ba-$Fe_4P_2W_{18}$/CP shows an onsetpotential at 1mA·cm^{-2} difference of 180mV versus the noble-metal oxide. On the other hand, the surprising fact is the performance of Ba-$Fe_4P_2W_{18}$/CP in comparison with NiFe and Fe_2O_3 which confirms at first instance the integrity of the catalyst and discard the oxide formation.

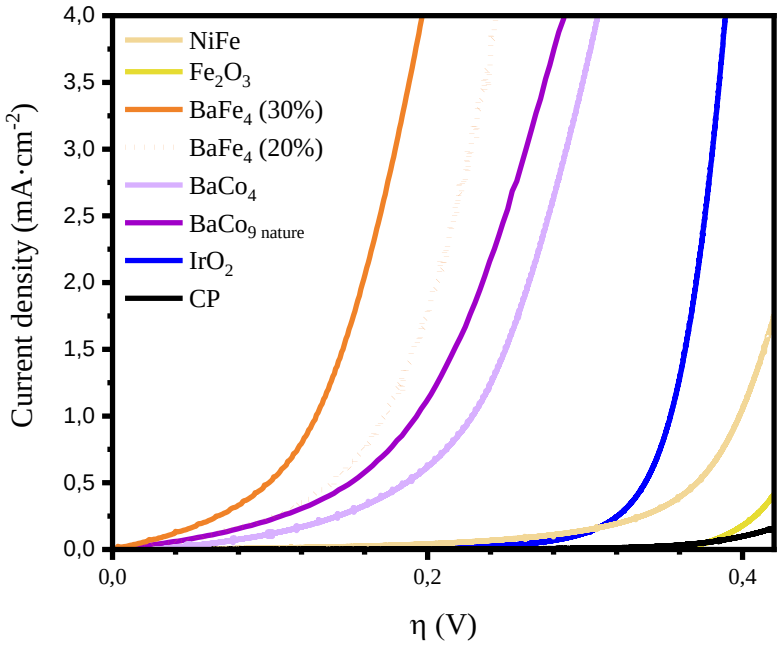

Figure 5.3. Linear sweep voltammetry of the 20% **Catalyst**/CP working electrodes. All the measurements were done in 1M H2SO4M at pH = 0.

In order to have real lecture of this highlight performance of Ba-$Fe_4P_2W_{18}$/CP, it is compulsory to take into account the number of moles of catalyst given by the different molecular weight. The electrochemical data was normalized by the total number of moles of catalyst (Figure 5.4). In the case of Ba-$Fe_4P_2W_{18}$/CP, 20% catalyst content normalized data is used to compare. The same trend is observed, nevertheless we observe highs difference in current density. In first instance, the oxide-based catalyst including the noble metal shows an insignificant activity. On the other hand, Ba-$Fe_4P_2W_{18}$/CP has the same performance than the reported Ba-Co_9 with a difference overpotential in comparison with analog POM of 84mV (Table 5.1).

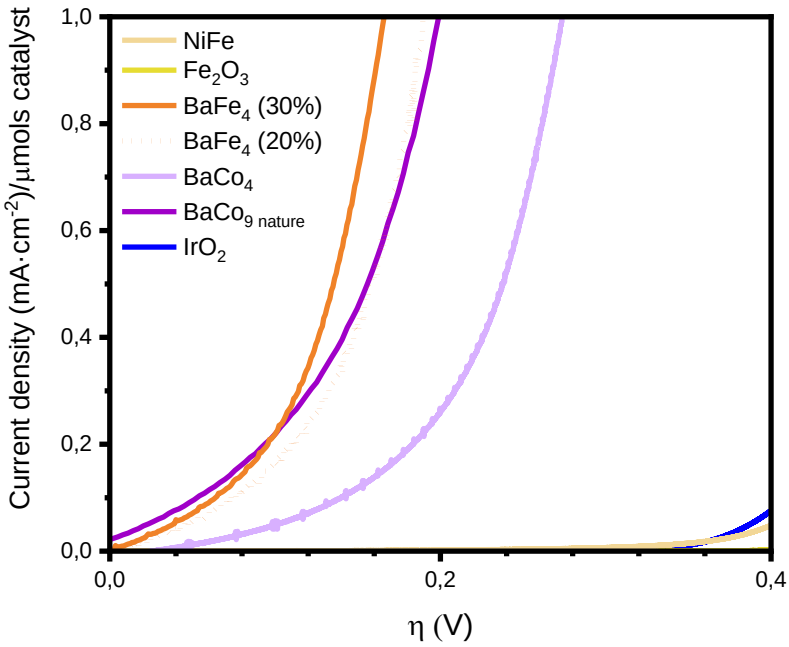

Figure 5.4. Linear sweep voltammetry normalized by the total number of moles of the 20% **Catalyst**/CP working electrodes. All the measurements were done in 1M H2SO4M at pH = 0.

Table 5.1. Experimental potentials (in V) and overpotentials (in mV) for 30% blend working electrodes of BaFe4, BaCo4 and BaCo9 in 1M H2SO4.

Potential/Overpotential	Set	$BaFe_4$[a]	$BaCo_4$	$BaCo_9$[b]
E vs RHE	@1mA·cm^{-2}	1.361	1.459	1.420
E vs SCE		1.120	1.218	1.179
η		129	229	190
E vs RHE	@1mA·cm^{-2}/μmols	1.419	1.502	1.426
E vs SCE		1.173	1.261	1.185
η		189	272	196

[a] Normalized currents density extracted from 20% blend [b] Extracted from reference [12].

Looking for any evidence of degradation we carried out a long-term chronopotentiometry measurements. The excellent energy efficiency offered by our Ba-$Fe_4P_2W_{18}$/CP catalyst is also matched by good long-term catalytic stability. This was confirmed by chronopotentiometry at 1mA·cm^{-2} for at least 4h. We assigned the initial decay to charge localization processes. For this experiment, we have covered the pocket electrodes which are mechanically unstable and tend to be expelled into the solution. On the other hand, we carried out an analogous experiment including periodic stops after each half-hour of electrolysis. The constant and reproducible starting performance is not compatible with catalyst degradation.

After two hours electrolysis at 1 mA·cm^{-2}, we collected the mother liquor and recovered the catalyst from the blend in order to characterize and confirm the observed stability of the catalyst. Raman and IR were used to detect traces of possible generated species during the catalysis. On the other hand, mother liquor was checked by elemental analysis (ICP-OES) to confirm ions leaching.

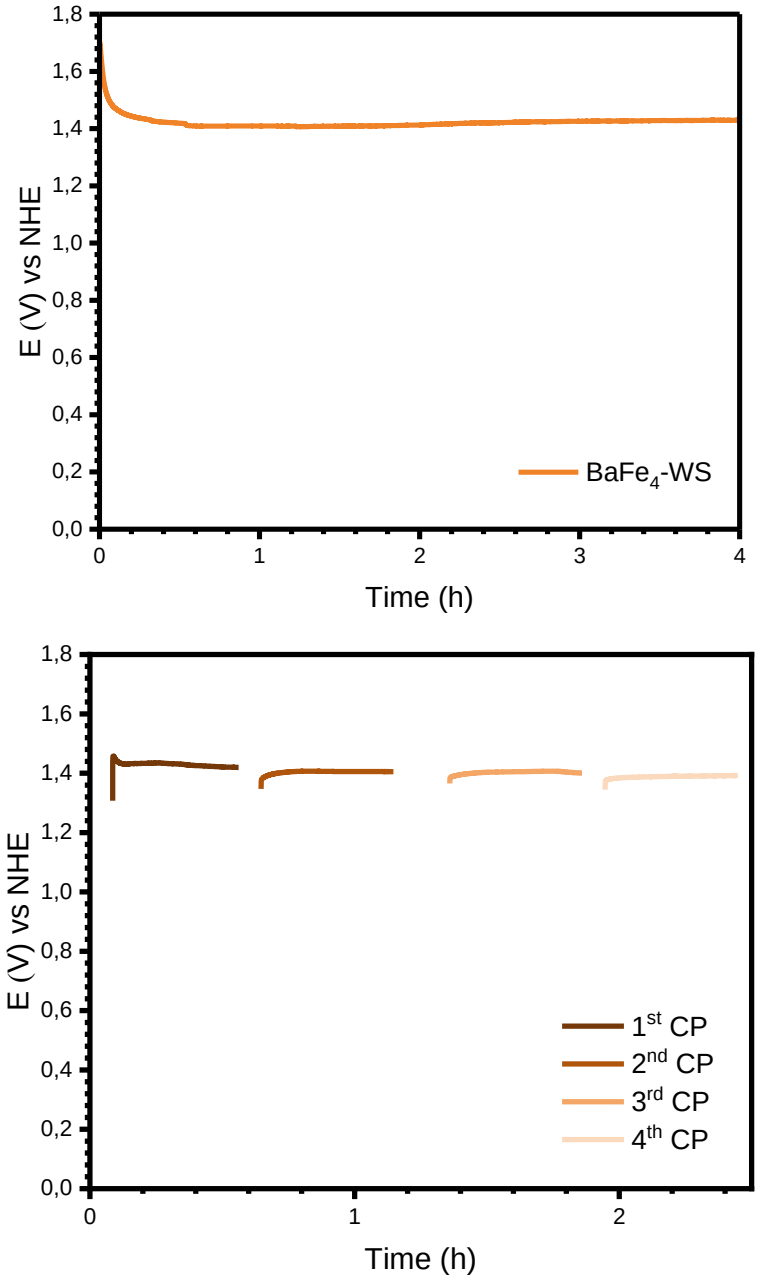

Figure 5.2. Top Chronopotentiometry data in 1M H_2SO_4 as the electrolyte at a constant current density of 1 $mA \cdot cm^{-2}$ with 20% Ba-$Fe_4P_2W_{18}$/CP. **Bottom** Intermittent chronoamperometry in H2SO4 (1 M) solution at a constant anodic current density of 1$mA \cdot cm^{-2}$ with 20 % Ba-$Fe_4P_2W_{18}$/CP: Anodic potential was applied for 30 min, and then open circuit voltage was maintained. This cycle was repeated 4 times showing identical response.

The Raman and IR spectra of the recovered Ba-$Fe_4P_2W_{18}$ matches that of the freshly made compound (Figure 4.5). Moreover, the electrolyte solution was analyzed by Inductively Coupled Plasma Mass Spectrometry (ICP-MS) to identify metal leaching (Table 4.1). The concentration of all the elements were below the detection limit of the technique, suggesting a good chemical stability under the working conditions.

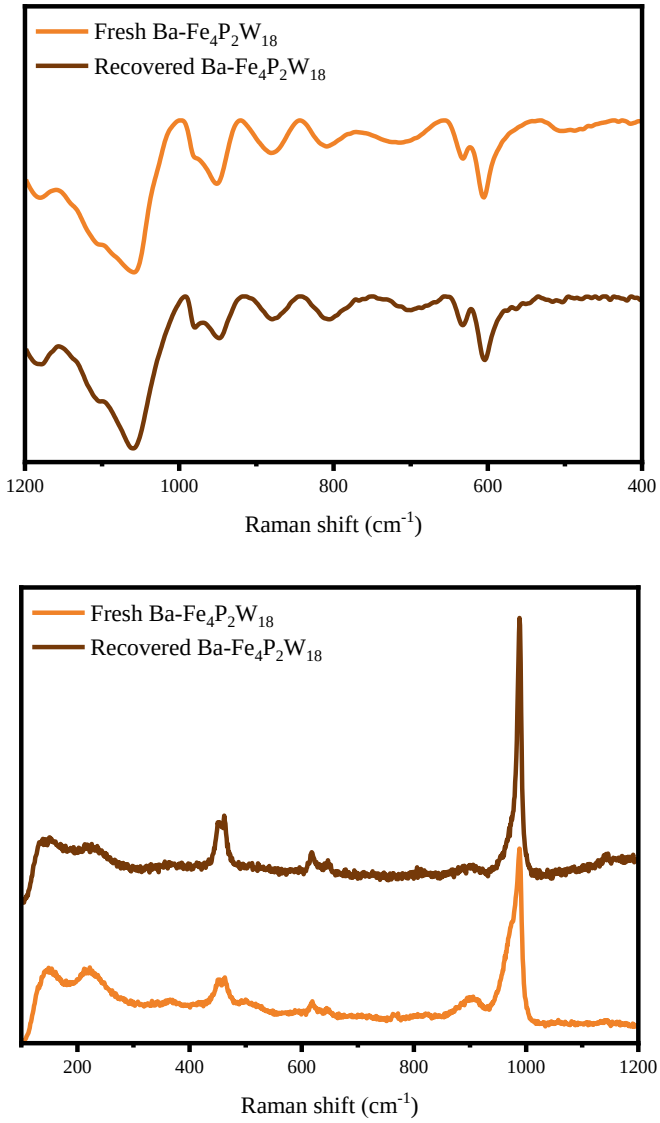

Figure 4.5. (**Top)** Raman spectra and **(Bottom)** IR spectra of Ba-$Fe_4P_2W_{18}$/CP before and after 2 h of electrocatalytic bulk water electrolysis at a constant current density of 1 mA·cm^{-2} in a pH = 6.9 potassium phosphate (50 mM) buffer solution with KNO_3 (1 M) as the electrolyte.

Table 4.1. ICP-MS analyses of the liquid reaction media after 2 h electrocatalytic water oxidation at a constant current density of 1 mA·cm^{-2} in H_2SO_4 (1 M) of stable compounds.

Mother liquor solution	Fe	Ba	W
Blank (KPi, 50mM; KNO_3 1M)	≤1.0 ppm	≤1.0 ppm	≤1.0 ppm
Ba-$Fe_4P_2W_{18}$	≤1.0 ppm	≤1.0 ppm	≤1.0 ppm

The unprecedent catalytic activity of Ba-$Fe_4P_2W_{18}$ must be confirmed by identifying the bubble evolution. The oxygen evolved employing Ba-$Fe_4P_2W_{18}$ during a chronopotentiometric experiment at 1 mA·cm^{-2} for one hour was measured employing a fluorescence probe. Unfortunately, this measurement confirms a faradaic oxygen production (>30%) compared with the theoretical amount of oxygen expected from a stoichiometric 4e$^-$ reaction (Figure 4.6). This result makes us touch the ground because the impressive electroactivity is result of a competitive electrochemical process. In order to determine the parallel redox process, we have measured the bubble evolution using gas chromatography accoupled to Mass Spectrometry (GC-MS). We have developed a new set up with the capacity to accumulate the gas formed from electrolysis and then drive it to GC-MS (Figure 4.7).

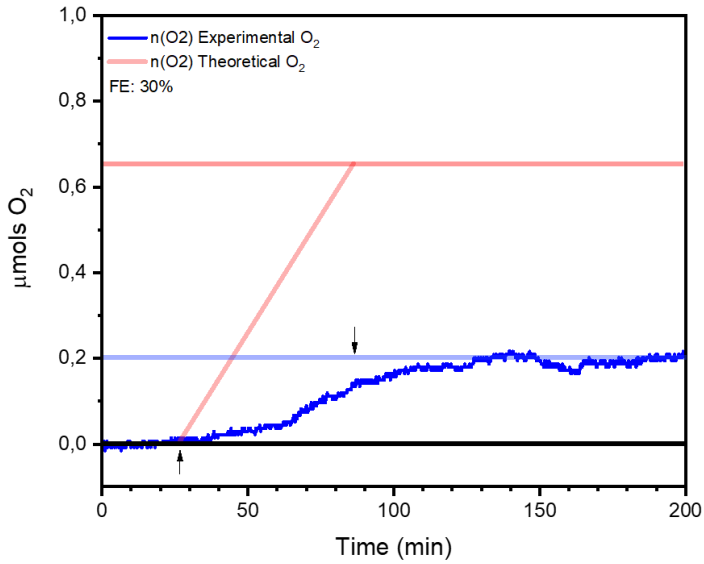

Figure 4.6. Oxygen evolution detection (blue) of the 20% Ba-$Fe_4P_2W_{18}$/CP during water electrolysis (at a constant current of 1 mA · cm^{-2}) in 1M H2SO4 at pH = 0. Theoretical oxygen evolution (red) taking into account a constant current of 1 mA·cm^{-2}. The arrows indicate initial and final electrolysis times.

We have performed electrolysis overnight (16 hours and 40 minutes) in a free oxygen environment using an acrylic box with a constant flow of Argon simulating glove box, to avoid any influence of atmospheric oxygen. The setup consists of a hermetic divided H-Cell with a glass frit defining two compartments, cathodic where takes place the HER and anodic where evolve the OER. On one hand, the hermetic cell has an entrance on liquid area in the cathodic compartment for Counter Electrode (CE) and two entrances on liquid area in the anodic compartment for Reference Electrode (Ref) and Working Electrode (WE). On the other hand, the cell has two entries in gas area in each compartment. In figure 4.7 can differentiate green entry which represents gas entrance and in red entry which represents gas exit. As the cathodic is not our interest, the gas exist has only an open-closing valve to close or open the compartment. Nevertheless, the anodic compartment, the gas entrance has a triple valve and the exist gas has another triple valve connected each other leading to a Bypass configuration. After that the exist gas of anodic is driven to GC-MS after to pass through inverted tramp to avoid any entrance of water to MS.

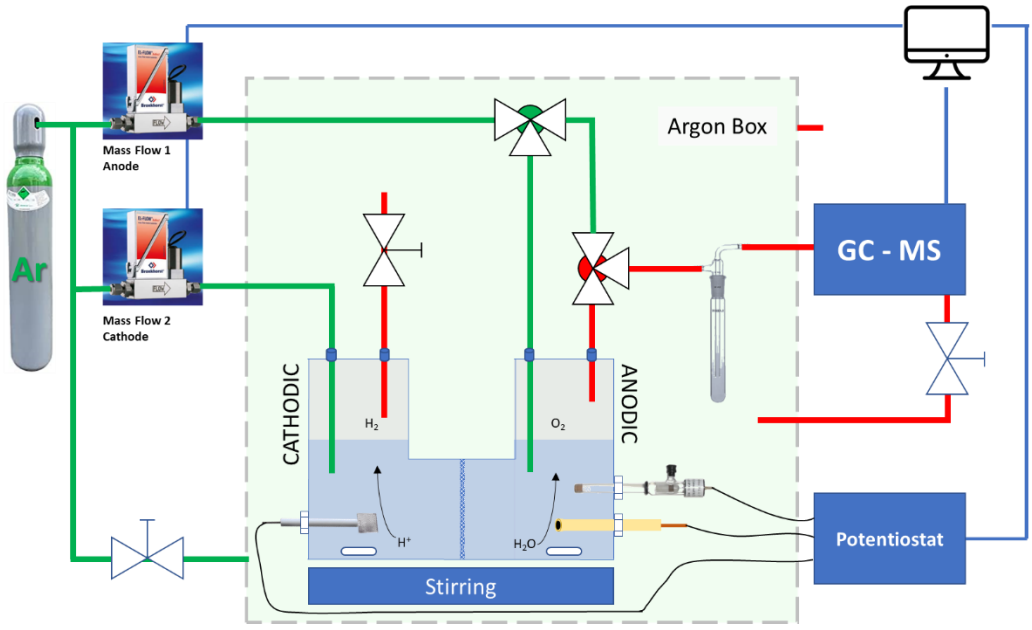

Figure 4.7. schematic representation of the O2 and CO2 setup detection.

In practice, first, the cell is purged with 10 ml/min of Argon for one hour and then the flow is reduced to the working flow which is 1.6 ml/min for three hours more. IN all moment the flow is controlled by automatic Mass Flow. The second step consist of close the cell, closing the cathode and stopping the flow and bypass the gas in the case of anodic compartment to GC-MS to obtain the base line. In this moment, the electrolysis has been performed along overnight. During this time the gas formed in the cell are accumulated in cell. Finally, after the electrolysis is stopped the gas accumulated in the gas area is driven by adjusting the three valves to the GC with Argon flow of 1.6 ml/min. Therefore, signal of the gas formed during the electrolysis can be detected.

Definitely, GC-MS results confirms qualitatively the formation of CO_2 in higher proportion considering O_2 (Figure 4.8). Considering the conductive support of the anode electrode is based on Carbon, the main source of this CO_2 is the amorphous graphite. Iron is a genuine transition metal with enhancing role in catalytic oxidation of carbon.[16]

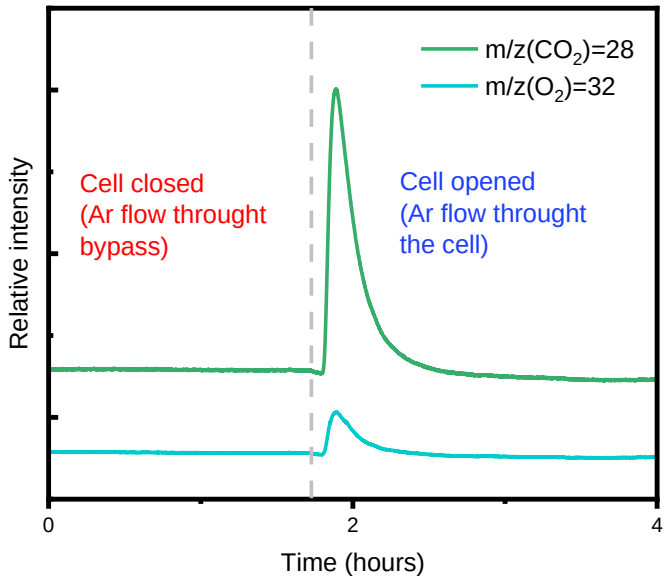

Figure 4.8. Oxygen and CO_2 evolution detection of the 20% Ba-$Fe_4P_2W_{18}$/CP during water electrolysis (at a constant current of 1 mA · cm^{-2}) in 1M H_2SO_4 at pH = 0 for 16 hours and 40 min.

Recent example was reported by Wei et al., where inorganic-ligand supported iron catalyst $(NH_4)_3[FeMo_6O_{18}(OH)_6]\cdot 7H_2O$ was described as a heterogeneous molecular catalyst in acetic acid for carbon–carbon bond cleavage of 1,2-diols.[17] However, the most interesting result here is the particular capacity of Fe-POM framework in comparison with alternative iron based oxide like NiFe and Fe_2O_3. Regarding this, we have also tested the performance of free Fe^{3+} in aqueous solution. We carried out the same experiment using an Equimolar amount of iron (III) as sulfate iron (III) into CP matrix to mimic identical working conditions (Figure 4.9).

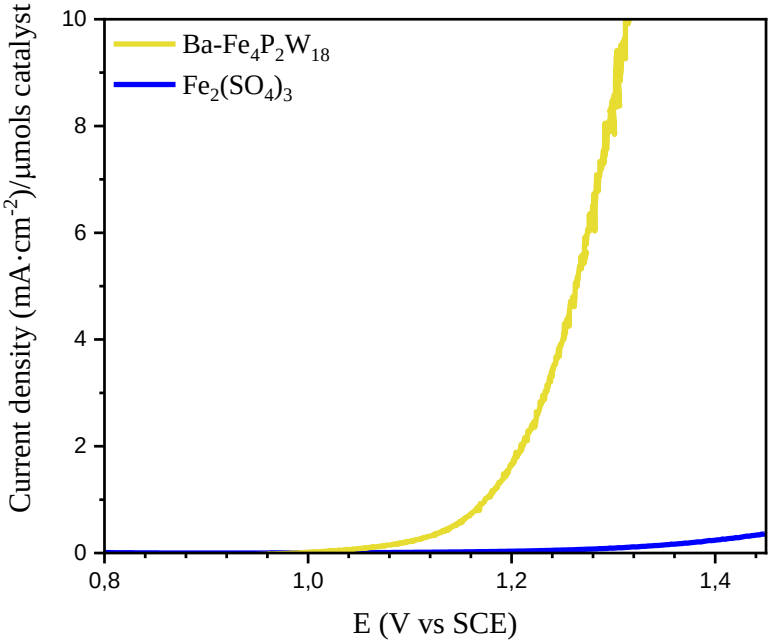

Figure 4.9. Linear sweep voltammetry normalized by the total number of moles of the 20% Ba-$Fe_4P_2W_{18}$/CP in comparison with equimolar amount of iron center using $Fe_2(sO4)_3$ working electrodes. All the measurements were done in 1M H2SO4M at pH = 0.

The experimental results are in agreement with a preliminary search of the active specie that we have performed using theoretical methodology. Unprotonated and protonated POM pathways have been studied. As is summarized in the square diagram representation (figure 4.10), the formation of the active specie requires a significant overpotential due to the exceed proton cations in the solution which makes the Proton

Couple Electron Transfer (PCET) and Proton Transfer (PT) thermodynamically more unaffordable.

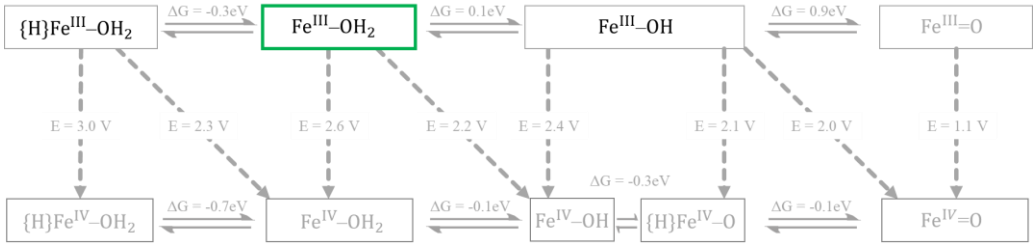

Figure 4.10. Square diagram representation of the PCET, PT and ET events for $Fe_4P_2W_{18}$ acting as WOC starting from the resting state species at pH = 0 to reach the *active* species. Potentials are given in V vs NHE for the electrochemical processes (PCET and ET), while the chemical processes related to acid-base equilibria (PT) are expressed as free Gibbs energy (in eV).

4.3. Conclusions

The earth-abundant catalyst for oxygen evolution reaction in acidic condition is now a days the key to make competitive the renewable energy. Our results lead us to reflect on the possibility of using iron-based compound, such as Ba[Fe-POM], as water oxidation catalyst in acidic conditions. The proposed $[(Fe^{III}OH_2)_2Fe^{III}_2(PW_9O_{34})_2]^{6-}$ in Carbon Paste matrix shows a remarkable resistance in a strongly acidic condition. We have studied his catalytical activity and confirmed that this iron-based POM is a true catalyst at 1 M H_2SO_4.

Our experimental data shows a reproducible and stable electrochemical performance without any signs of pre-catalytical event or active specie evolution. However, the excellent and unique catalytical performance of Ba-$Fe_4P_2W_{18}$ (η =189 mV @ 1mA·cm^{-2}) in comparison with Co-POM cannot be associated only to oxygen evolution reaction. Our results confirm the presence of a competitive electrochemical process involving carbon oxidation reaction given the formation of O_2 and CO_2. This phenomenon brings to light the versatility of iron with its ability to oxidize carbon as well as water in strongly acidic condition. Unfortunately, the protective role of CP matrix supposes a source of the competitive reaction. Further studies are needed to substitute the CP since is not a robust electrode for the long term and can involve a secondary reaction. In summary, our study bears out the importance of study deeper iron compounds as catalysts for water oxidation in acidic condition.

4.4. References

[1] L. Trotochaud, S. L. Young, J. K. Ranney, S. W. Boettcher, *J. Am. Chem. Soc.* **2014**, *136*, 6744.

[2] R. D. L. Smith, M. S. Prévot, R. D. Fagan, Z. Zhang, P. A. Sedach, M. K. J. Siu, S. Trudel, C. P. Berlinguette, *Science (80-.).* **2013**, *340*, 60 LP.

[3] J. R. Galán-Mascarós, *ChemElectroChem* **2015**, *2*, 37.

[4] J. Suntivich, K. J. May, H. A. Gasteiger, J. B. Goodenough, Y. Shao-Horn, *Science (80-.).* **2011**, *334*, 1383.

[5] A. Harriman, *Philos. Trans. R. Soc. A Math. Phys. Eng. Sci.* **2013**, *371*, 20110415.

[6] E. H. Yu, X. Wang, U. Krewer, L. Li, K. Scott, *Energy Environ. Sci.* **2012**, *5*, 5668.

[7] A. Harriman, I. J. Pickering, J. M. Thomas, P. A. Christensen, *J. Chem. Soc.{,} Faraday Trans. 1* **1988**, *84*, 2795.

[8] Q. Yin, J. M. Tan, C. Besson, Y. V Geletii, D. G. Musaev, A. E. Kuznetsov, Z. Luo, K. I. Hardcastle, C. L. Hill, *Science (80-.).* **2010**, *328*, 342 LP.

[9] J. W. Vickers, H. Lv, J. M. Sumliner, G. Zhu, Z. Luo, D. G. Musaev, Y. V. Geletii, C. L. Hill, *J. Am. Chem. Soc.* **2013**, *135*, 14110.

[10] S. Goberna-Ferrón, L. Vigara, J. Soriano-López, J. R. Galán-Mascarós, *Inorg. Chem.* **2012**, *51*, 11707.

[11] J. Soriano-López, S. Goberna-Ferrón, L. Vigara, J. J. Carbó, J. M. Poblet, J. R. Galán-Mascarós, *Inorg. Chem.* **2013**, *52*, 4753.

[12] M. Blasco-Ahicart, J. Soriano-López, J. J. Carbó, J. M. Poblet, J. R. Galan-Mascaros, *Nat. Chem.* **2017**, *10*, 24.

[13] J. Yu, F. A. Garcés-Pineda, J. González-Cobos, M. Peña-Díaz, C. Rogero, S. Giménez, M. C. Spadaro, J. Arbiol, S. Barja, J. R. Galán-Mascarós, *Nat. Commun.* **2022**, *13*, 1.

[14] M. Okamura, M. Kondo, R. Kuga, Y. Kurashige, T. Yanai, S. Hayami, V. K. K. Praneeth, M. Yoshida, K. Yoneda, S. Kawata, S. Masaoka, *Nature* **2016**, *530*, 465.

[15] K. Azmani, M. Besora, J. Soriano-López, M. Landolsi, A. L. Teillout, P. de Oliveira, I. M. Mbomekallé, J. M. Poblet, J. R. Galán-Mascarós, *Chem. Sci.* **2021**, *12*, 8755.

[16] E. T. Turkdogan, J. V Vinters, *Carbon N. Y.* **1972**, *10*, 97.

[17] W. Chen, X. Xie, J. Zhang, J. Qu, C. Luo, Y. Lai, F. Jiang, H. Yu, Y. Wei, *Green Chem.* **2021**, *23*, 9140.

Chapter 5

General Conclusions and Future Work

5.1. General Conclusions

In this thesis, we have explored different parameters in order to deeply understand polyoxometalates based on the earth abundant transition metal as suitable water oxidation catalysts. Below we summarize the specific conclusions that we have drawn in each chapter.

Conclusion 1: From the evaluation of a series of cobalt polyoxometalates (Co-POMs) we have confirmed that the stability of the POM is partially determined by the heteroatom, being P the preferred candidate in the working conditions (acidic media).

Conclusion 2: Considering the performance we observed a clear trend favoring Keggin-derivatives in comparison with their Dawson-counterparts in Weakley sandwich structures.

Conclusion 3: The catalytic activity is favored by higher nuclearity of the cobalt cluster embedded by the POM ligands.

Conclusion 4: We have confirmed the remarkable role that the carbon paste plays with the partial hydrophobic environment to stabilize stable water oxidation catalysts even in acidic media.

Conclusion 5: From an accurate analysis of insoluble barium salts of anion $[Fe^{III}_4(H_2O)_2(B\text{-}\alpha\text{-}PW_9O_{34})_2]^{6-}$, we have concluded that the Fe-POMs display similar OER activity, and slightly slower kinetics than the corresponding Co-POM derivative.

Conclusion 6: Fe-POMs shows a remarkable stability under heterogeneous electrocatalytic conditions regarding the oxygen evolution reaction.

Conclusion 7: Computational studies show that understanding molecular WOC speciation at the working conditions is critical to rationalizing the catalyst activity. Computed chemical potentials, in general, agree with the experimental ones.

Conclusion 8: The promising results of tetrairon POM in chapter 3 motivate us to evaluate its activity and stability in acidic conditions, confirming the synergetic effect of a partially hydrophobic composite electrode (carbon paste) to stabilize Fe-POM-based catalysts under strongly acidic conditions.

Conclusion 9: Our results confirm a competitive catalyst performance of Fe_4-POM regarding the oxygen evolution reaction. The Fe_4-POM shows a versatile ability to oxidize carbon as well as water under strongly acidic conditions. This means that alternative electrode support is needed to explore the real activity of the Fe_4-POM in acidic media.

5.2. Future Work

The superior performance of Ba-Co_9 encourage us to investigate and understand the science behind. Thus, we have begun to study the important effect exerted by the cation, observed for the first time by the Galán-Mascarós group between the insoluble salts of cesium and barium. We decided to test the activity in acidic media of different cations salts of Co_9, which were obtained by simple metathesis of the corresponding potassium salt. In order to understand the performance, we selected cations with different valence charge and ionic radius corresponding to groups 1, 2,3 and 4 of periodic table. However, the most important feature of this salt is the insolubility. We have analyzed the behavior of several salts of Co_9 anion including as counter cations, Cs^+, Rb^+, Ba^{2+}, Sr^{2+}, Y^{3+}, La^{3+} and Zr^{4+}.

The proposed salts become insoluble once are precipitated from the potassium salts. Then, we carried out linear sweep voltammetry (LSV) to investigate the electrochemical activity. To our surprise, Ba-Co_9/CP electrode still shows the best electrocatalytic performance (Figure 5.1) with at least 50 mV difference at 1 mA·cm^{-2}.

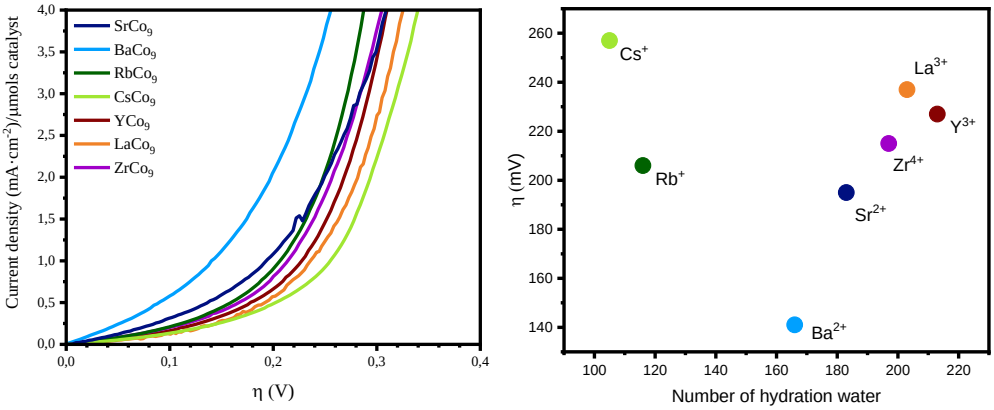

Figure 5.1. Left) Linear sweep voltammetry in H_2SO_4 (1 M) solution with 30% Co-POM/CP blend working electrodes with different counter cations Right) Onset overpotential at 1mA·cm^{-2} from normalized current density by mols of catalyst versus number of hydration water.

Our preliminary results confirm the persistent superior performance of Ba-Co_9/CP. In general terms, we could observe a trend regarding the charge valence of the counter cations, where bivalents are better than trivalent and these better that monovalent. However, there is an exception with Rb-Co_9, which becomes the most efficient after bivalent cations. On the other hand, we have observed a relationship between the onset overpotential and the number of hydration water molecules. It seems that a number of water molecules not too high or not too low favors the oxidation process. The number of waters is a representation of the environment. However, it does not explain exactly what the role of the cations is.

The preliminary results encourage us to continue working to understand the effect of the cation environment on the catalytic properties of the POM. Nevertheless, further experiments and theoretical studies are needed to confirm the stability, the true role of the cations and the reaction mechanisms of the oxygen evolution reaction. In particular, when we are working in acidic conditions.

UNIVERSITAT
ROVIRA i VIRGILI